# Air-light exposure of $Cu(In,Ga)Se_2$ thin film absorber layers and the effects on complete solar cells

## Dissertation

zur Erlangung des Doktorgrades der Naturwissenschaften

*(Dr. rer. nat.)*

der

Naturwissenschaftlichen Fakultät II

Chemie, Physik und Mathematik

der Martin-Luther-Universität

Halle-Wittenberg

vorgelegt von

Herrn Torsten Hölscher

geb. am 27.05.1985 in Wolfen

Date of submission: 25.08.2021

Date of defence: 28.09.2022

1. Reviewer and Supervisor: Prof. Dr. Roland Scheer (Martin-Luther-University)

2. Reviewer: Prof. Dr. Wolf Widdra (Martin-Luther-University)

Exterrnal Reviewer: Prof. Dr. Clemens Heske (Karlsruhe Institute of Technology)

Member of the doctoral Committee: Prof. Dr. Miguel Marques (Chair), Prof. Dr. Thorid Raabe, Dr. habil. Hartmut Leipner, Prof. Dr. Kathrin Dörr

## List of Publications

## Authored publications

[Höl1] T. Hölscher, S. Förster, T. Schneider, M. Maiberg, W. Widdra, and R. Scheer, Light induced degradation of Cu(In,Ga)$Se_2$ thin film surfaces, *Applied Physics Letters*, **111**, (2017). → (Paper 1)

[Höl2] T. Hölscher, T. Schneider, M. Maiberg, and R. Scheer, Critical role of air-light exposure on co-evaporated Cu(In,Ga)$Se_2$ solar cells, *Japanese Journal of Applied Physics*, **57**, (2018). → (Paper 2)

[Höl3] T. Hölscher, T. Schneider, M. Maiberg, and R. Scheer, Impact of air-light exposure on the electrical properties of Cu(In,Ga)$Se_2$ solar cells, *Progress in Photovoltaics*, **26**, 934-941 (2018). → (Paper 3)

[Höl4] T. Hölscher, T. Walter, T. Schneider, M. Maiberg, and R. Scheer, Device simulation of Cu(In,Ga)$Se_2$ solar cells by means of voltage dependent admittance spectroscopy, *Thin Solid Films*, **669**, 345-350 (2019). → (Paper 4)

[Höl5] T. Hölscher, S. Förster, T. Schneider, M. Maiberg, W. Widdra, and R. Scheer, Light induced modification of copper indium gallium diselenide thin film and solar cells, in *33rd European Photovoltaic Solar Energy Conference*, Amsterdam, 1088-1092 (2017).

## Co-authored publications

[Höl6] E. Jarzembowski, F. Syrowatka, K. Kaufmann, W. Fränzel, T. Hölscher, and R. Scheer, The influence of sodium on the molybdenum/Cu(In,Ga)$Se_2$ interface recombination velocity, determined by time resolved photoluminescence, *Applied Physics Letters*, **107**, (2015).

[Höl7] M. Maiberg, T. Hölscher, S. Zahedi-Azad, and R. Scheer, Theoretical study of time-resolved luminescence in semiconductors. III. Trap states in the band gap, *Journal of Applied Physics*, **118**, (2015).

[Höl8] M. Maiberg, T. Hölscher, S. Zahedi-Azad, W. Franzel, and R. Scheer, Investigation of long lifetimes in Cu(In, Ga)$Se_2$ by time-resolved photoluminescence, *Applied Physics Letters*, **107**, (2015).

[Höl9] M. Maiberg, T. Hölscher, E. Jarzembowski, S. Hartnauer, S. Zahedi-Azad, W. Franzel, and R. Scheer, Verification of minority carrier traps in $Cu(In,Ga)Se_2$ and $Cu_2ZnSnSe_4$ by means of time-resolved photoluminescence, *Thin Solid Films*, **633**, 208-212 (2017).

[Höl10] T. Schneider, T. Hölscher, H. Kempa, and R. Scheer, Determination of the back contact recombination velocity of a $Cu(In,Ga)Se_2$/ITO interface using bifacial solar cells, in *37th European Photovoltaic Solar Energy Conference*, Online, 621-626 (2020).

[Höl11] B. Mahmoudi, F. Caddeo, T. Lindenberg, T. Schneider, T. Hölscher, R. Scheer, and A. W. Maijenburg, Photoelectrochemical properties of Cu-Ga-Se photocathodes with compositions ranging from CuGaSe2 to CuGa3Se5, *Electrochimica Acta*, **367**, 137183 (2021).

[Höl12] S. M. Lyam, T. Hölscher, M. Maiberg, A. Cabas-Vidani, A. Hernandez-Martinez, H. Tampo, and R. Scheer, Dominant recombination path in low-bandgap Kesterite CZTSe(S) solar cells from red light induced metastability, *Journal of Applied Physics*, **129**, 205703 (2021).

[Höl13] T. Schneider, C. Dethloff, T. Hölscher, H. Kempa, and R. Scheer, Comparison of Mo and ITO back contacts in CIGSe solar cells: Vanishing of the main capacitance step, *Progress in Photovoltaics*, submitted (2021).

# Abstract

The present thesis deals with the light induced detrimental modification of $Cu(In,Ga)Se_2$ (CIGSe) layers in ambient (humid) air. Exposure of bare CIGSe layers to light in ambient air, called air-light exposure (ALE), is often unavoidable during the manufacturing process of solar cells in the laboratory scale as well as in the industrial scale. In this work it can be shown that after short ALE periods of few minutes, a significant reduction of minority charge carrier lifetime measured with time-resolved photoluminescence (TRPL) give reasons for the detrimental effect of ALE on CIGSe for solar cell applications. The vital importance of light during ALE is demonstrated by no reduction of TRPL lifetime even after storage in ambient air and darkness of several hours. From X-ray photoelectron spectroscopy (XPS) a modification of the CIGSe surface chemistry due to ALE is observed. In XPS-measurements the enhancement in photoelectron emission and the lowering in binding energies of the Na 1s and O 1s core levels are characteristic for ALE surfaces. The O 1s emission peak centred at 531.6 eV relates to a detrimental Na-O-CIGSe bonding complex, considered responsible for the ALE induced lifetime reduction in TRPL measurements. This lifetime reduction manifests in inferior J-V-parameters of solar cells based on ALE absorbers. Compared to non-ALE solar cells the relative drop in power conversion efficiency can amount up to 30% depending on ALE time and light intensity. With measurements of open circuit voltage as a function of temperature $V_{OC}(T)$ and time $V_{OC}(t)$, dominating recombination at the absorber/buffer interface (IF) is diagnosed for solar cells with ALE absorbers. Voltage dependent admittance spectroscopy reveals a voltage dependent defect signature, responsible for recombination centres at the interface. Performing 1 dimensional device simulations the considered IF-defects are found to be of acceptor type centred on an energy level of 0.3 eV above the valence band with a defect density of $3.5 \cdot 10^{11}$ $cm^{-2}$. On the contrary, solar cells with non-ALE absorbers are not dominated by IF-recombination and hence no interface defects are detected. By application of heat-light soaking (HLS) on ALE impaired solar cells the drop in efficiency can be reversed. HLS for several hours recovers solar cell parameters to a level comparable with non-ALE solar cells. After HLS the dominant role of interface recombination vanishes in $V_{OC}(T)$- and $V_{OC}(t)$-measurements accompanied by no detectable IF-defects in voltage dependent admittance spectroscopy. With glow-discharge optical emission spectroscopy (GDOES) it is found that the elimination of dominating IF-recombination due to HLS comes along with an increased concentration of Na at the absorber/buffer interface. Thus, in contrast to ALE, Na exhibits passivating properties during HLS.

# Kurzfassung (german abstract)

Die vorliegende Arbeit handelt von der verschlechternden Veränderung von $Cu(In,Ga)Se_2$ (CIGSe) Schichten, hervorgerufen durch Beleuchtung in Umgebungsluft. Das Aussetzen der freien CIGSe-Oberfläche gegenüber Licht und Umgebungsluft (engl.: air-light exposure = ALE) ist im Herstellungsprozess von CIGSe-Solarzellen oft unvermeidbar, unabhängig ob im Labormaßstab oder im industriellen Maßstab. Dementsprechend kann in dieser Arbeit gezeigt werden, dass schon nach wenigen Minuten ALE eine starke Verringerung der Lebensdauer der Minoritätsladungsträger, gemessen mit zeitaufgelöster Photolumineszenz (TRPL), auftritt. Diese Verringerung in der Lebensdauer lässt wiederum die Vermutung auf eine Verschlechterung der resultierenden Solarzelle zu, welche mit einem ALE Absorber ausgestattet ist. Die gewichtige Rolle des Lichtes während ALE kann durch die Aussetzung der freien CIGSe Oberfläche gegenüber Umgebungsluft in vollkommener Dunkelheit demonstriert werden. Folglich, zeigt sich nach mehreren Stunden Lagerung der CIGSe Schichten in Umgebungsluft und Dunkelheit keine Reduktion der mit TRPL gemessenen Lebensdauern. Durch Röntgenphotoelektronenspektroskopie (XPS) kann gezeigt werden, dass ALE eine Veränderung der Oberflächenchemie der CIGSe Schichten hervorruft. Diese Veränderung ist charakterisiert durch eine erhöhte Photoelektronenemission und eine Verringerung der Bindungsenergien für die Na 1s und O 1s Bindungsniveaus. Das Maximum des O 1s Emissionspeaks liegt für ALE Oberflächen typischerweise bei einer Bindungsenergie von 531.6 eV, welche einer abträglichen Na-O-CIGSe Verbindung zugeordnet wird. Diese Verbindung wird als Ursache der ALE bedingten Lebensdauerverringerungen in TRPL Messungen erachtet. Die ALE bedingte Verringerung der TRPL Lebensdauer des CIGSe Absorbers zeichnet sich ebenfalls in einer Reduktion der charakteristischen Parameter der auf diesen Absorbern basierenden Solarzellen ab. Im Vergleich zu Solarzellen mit unverminderten Absorbern kann die durch ALE hervorgerufene relative Verringerung der Leistungskonversionseffizienz bis zu 30% betragen. Dabei, steht die Größe der Effizienzverringerung in Abhängigkeit der ALE Dauer und der eingestrahlten Lichtintensität während ALE. Durch Messungen der Leerlaufspannung als Funktion der Temperatur $V_{OC}(T)$ und als Funktion der Zeit $V_{OC}(t)$ konnte für Solarzellen mit ALE Absorbern eine erhöhte Rekombination an der Absorber/Puffer Grenzfläche festgestellt werden. Bei der Anwendung von spannungsabhängiger Admittanzspektroskopie zeigte sich zudem für ALE Solarzellen eine spannungsabhängige Defektsignatur, welche charakteristisch für Grenzflächendefekte ist. Mittels 1 dimensionaler Simulation der Solarzelle als elektrisches

Bauelement ließen sich die Parameter der Grenzflächendefekte bestimmen. Die Simulationsergebnisse zeigten, dass die Grenzflächenzustände durch Akzeptoren beschrieben werden können. Das Energieniveau dieser Akzeptoren zentriert sich 0.3 eV oberhalb des Valenzbandes innerhalb der Bandlücke des Absorbers. Die Dichte der Defektzustände beträgt $3.5 \cdot 10^{11}$ $cm^{-2}$. Im Gegensatz, weisen Solarzellen, basierend auf CIGSe Absorberschichten die keinem ALE ausgesetzt waren, weder dominierende Grenzflächenrekombination in $V_{OC}(T)$- und $V_{OC}(t)$-Messungen auf, noch die Detektion eines Grenzflächendefektes in spannungsabhängiger Admittanzspektroskopie.

Durch Beleuchtung mittels weißem Licht (0.1 $W \cdot cm^{-2}$) und unter erhöhten Temperaturen (80 - 90°C) der kompletten Solarzellen bei geöffneten klemmen, genannt heat-light soaking = HLS, können die Solarzellenparameter von Zellen mit ALE Absorbern auf das Niveau von Zellen mit Absorbern ohne ALE angehoben werden. Die Verbesserung der Solarzellenparameter nach HLS gehen einher mit der nicht mehr vorhandenen Dominanz von Grenzflächenrekombination in $V_{OC}(T)$- und $V_{OC}(t)$-Messungen, sowie dem Ausbleiben des mit der Gleichspannung variierenden Signals eines Grenzflächendefektes in spannungsabhängiger Admittanzspektroskopie. Mittels Glimmentladungsspektroskopie (engl.: glow-discharge optical emission spectroscopy = GDOES) angewendet vor und nach HLS zeigt sich eine durch HLS hervorgerufene Anreicherung von Natrium an der Absorber/Puffer Grenzfläche. Daher kann für Natrium, im Gegensatz zu ALE, eine passivierende Rolle während HLS geschlussfolgert werden.

# Table of content

**1. Introduction ..... 1**

1.1. Air exposure of CIGSe layers ..... 4

1.2. Air-light exposure of CIGSe layers ..... 5

**2. Fundamentals ..... 7**

2.1. Cu(In,Ga)$Se_2$-based solar cells ..... 7

2.1.1. Architecture and preparation techniques ..... 7

2.1.2. Basic properties of Cu(In,Ga)$Se_2$ absorber layers ..... 12

2.1.3. Impact of Sodium ..... 18

2.1.4. Incorporation of Sodium ..... 19

2.1.5. Metastable properties ..... 21

2.1.6. Sample preparation for the present study ..... 22

2.2. The p-$n^-$-n-$n^+$-hetero-junction ..... 23

2.2.1. Ideal diode current ..... 31

2.3. Regions of recombination ..... 41

2.3.1. (A) QNR recombination ..... 42

2.3.2. (B) SCR recombination ..... 45

2.3.3. (C) Interface recombination ..... 50

**3. Measurement techniques ..... 63**

3.1. Open circuit voltage ($V_{OC}$) measurements ..... 63

3.1.1. $V_{OC}$ as a function of temperature ..... 63

3.1.2. $V_{OC}$ as a function of time ..... 67

3.2. Admittance spectroscopy ..... 69

3.2.1. Equivalent circuit and Schottky barrier at the back contact ..... 71

3.2.2. Volume and interface defects ..... 76

**4. Experimental results and device simulation ..... 79**

4.1. ALE induced surface modification ..... 79

4.1.1. Supporting information and considerations of Paper 1 ..... 85

4.2. Disclosure of ALE kinetics and self-healing by HLS ..... 90

4.2.1. Supporting information and considerations of Paper 2 ..... 95

4.3. Existence and elimination of dominant interface-recombination ..... 99

4.3.1. Supporting information and considerations of Paper 3 ..... 108
4.4. Quantification of interface defects and device modelling ..... 110

**5. Conclusion ..... 117**

**6. Outlook ..... 119**

**References ..... 121**

**A. Appendixes ..... 1**

A.1. Potential curve of a n-$n^+$-hetero-junction ..... A-1
A.2. General properties of simulation models ..... A-3
A.3. Physical quantities: Default simulation model ..... A-4
A.4. Physical quantities: Simulation model of Paper 4 ..... A-5
A.5. Overview samples used for ALE experiments ..... A-6

**Danksagung (Acknowledgement)**

**Eidesstattliche Erklärung (Declaration on oath)**

# List of symbols and abbreviations

| | |
|---|---|
| AE | Air exposure |
| $A_i$ | Diode quality factor of the particular recombination current density |
| ALE | Air-light exposure |
| $\alpha$ | Absorption coefficient of light |
| $A^*$ | Richardson constant of thermionic emission theory |
| BC | Region in the proximity of the back contact |
| CBD | Chemical bath deposition |
| $C_{i,j}$ | Capacitance normalized to the cross-sectional area with i = QNR, SCR, BC and j = a, b, hrw, lrw |
| $\chi_{e,i}$ | Electron affinity of particular layer (i = a, b, hrw, lrw) |
| CIGSe | Copper indium gallium diselenide, $Cu(In,Ga)Se_2$ |
| DA | Dark annealing (tempering of devices at high temperatures ≈ 90°C in darkness) |
| $\Delta E_C$ | Conduction band offset in between 2 semiconductors with different electron affinities |
| $D_{n,a}$ | Diffusion length of electrons within the absorber |
| $E_A$ | Activation energy of the saturation current density $J_0$ |
| $E_F$ | Equilibrium Fermi-level |
| $E_{Fn}$, $E_{Fp}$ | Quasi-Fermi level of electrons or holes |
| $E_{g,i}$ | Band gap energy of the particular semiconductor (i = a, b, hrw, lrw) |
| $\varepsilon_0$ | Vacuum permittivity |
| $\varepsilon_{r,i}$ | Relative permittivity of particular semiconductor (i = a, b, hrw, lrw) |
| EQE | External quantum efficiency |
| $E_{z,i}$ | Electric field component in z-direction |
| $\eta_C$ | Collection efficiency of generated charge carriers |
| $\eta_{Cell}$ | Solar cell efficiency (analogous: PCE) |
| FF | Fill factor |
| $\gamma_{A,if}$ , $\gamma_{D,if}$ | Degree of ionized acceptor or donor states at the interface |
| $G_n$, $G_p$ | Generation rate of electrons or holes |
| HLS | Heat light soaking (long time illumination of devices under increased temperatures ≈ 90°C) |
| hrw | high resistive window layer (i-ZnO) |
| IF | Interface |
| i-ZnO | intrinsic (undoped) Zincoxide (IZO) |
| $J_{ph}$ | Collected photo current density |

| | |
|---|---|
| $J_{SC}$ | Short circuit current density |
| $J_0$, $J_{01}$, $J_{02}$, $J_{0,i}$ | Saturation current densities (i = QNR, SCR, IF) |
| $J_{00}$ | Reference current density |
| $k_B$ | Boltzmann constant |
| $\lambda_{D,i}$ | Debye length of majority charge carriers |
| $L_n$, $L_p$ | Diffusion length of electrons or holes |
| lrw | low resistive window layer (ZnO:Al) |
| $N_{A,a}$ | Shallow acceptor density of the p-absorber |
| $N_{D,i}$ | Shallow donor density of the buffer (i = b) or window layers (i = hrw, lrw) |
| $N_{d,i}$ | Density of volume defects in the particular semiconductor (i = a, b, hrw, lrw) |
| $N_{d,if}$ | Surface density of defect states at interfaces |
| $n_{i,j}$ | Intrinsic charge carrier density of particular semiconductor (j = a, b, hrw, lrw) |
| N1 | Recurrent signature in admittance spectroscopy of CIGSe solar cells |
| $N_V$, $N_C$ | Effective density of states of the valence band or conduction band |
| $\omega_0$ | Characteristic angular frequency of capacitance steps |
| PCE | Power conversion efficiency |
| $\Phi_B$ | Energetical barrier for charge carriers |
| $\varphi_i$ | Electro static potential within a specific region |
| $\Phi^p_{if,a}$ | Hole barrier at the front interface of the absorber |
| $\Phi_m$ | Work function of metal contacts |
| PL | Photoluminescence |
| QNR | Quasi-neutral region |
| $R_n$, $R_p$ | Recombination rate of electrons or holes |
| SCR | Space charge region |
| $\sigma_n$ , $\sigma_p$ | Capture cross section of electrons or holes |
| SIMS | Secondary ion mass spectroscopy |
| SLG | Soda lime glass |
| $S_n$, $S_p$ | Recombination velocity of electrons or holes |
| SRH | Shockley-Read-Hall |
| $\tau_{n,a}$ | Lifetime of electrons within the p-type absorber layer |
| TRPL | Time-resolved photoluminescence |
| $V_{BC}$ | Built-in voltage of a Schottky barrier at the back contact |
| $V_{bi}$ | Built-in voltage (complete potential drop in between absorber and low resistive window layer) |
| $V_{OC}$ | Open circuit voltage |
| $w_a$ | Depletion width of the absorber |
| $w_{i,j}$ | Width of a specific region (i = SCR, QNR, BC) within a semiconductor (j = a, b, hrw, lrw) |
| XPS | X-ray photoelectron emission spectroscopy |
| ZnO:Al | Aluminium doped Zincoxide (AZO) |

# 1. Introduction

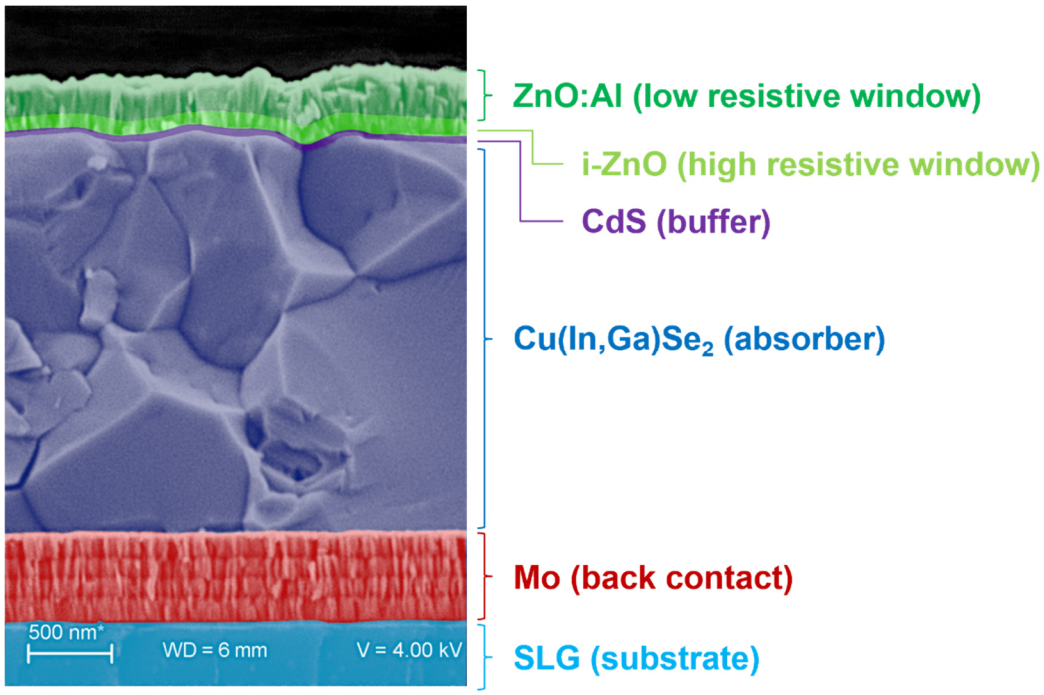


**Figure 1** Scanning electron microscopy cross-section of a $Cu(In,Ga)Se_2$ solar cell fabricated at the Martin-Luther-University. The incorporation of Sodium into the absorber layer took place by diffusion from the soda lime glass substrate (SLG) through the Mo back contact at high temperatures (> 600°C).

Power conversion efficiencies (PCE) of 19.2% [1] at module scale have been demonstrated for photovoltaic thin film devices based on the p-type absorber material $Cu(In,Ga)Se_2$ (CIGSe). Despite the question of abundance of elements like Indium or Gallium and existing PCE's decisively below crystalline Silicon based modules with 24.4% [1], there are nevertheless several reasons making CIGSe photovoltaic technology interesting for consumers, investors and manufactures.

1. The *energy payback time* of CIGSe solar cells is lower than of Silicon devices (2.2 years, solar irradiance: 1000 $kWh \cdot m^{-2}y^{-1}$ [2]) and shows further potential to be reduced by reducing deposition temperatures and thicknesses of functional layers [3-6].
2. *Flexible solar cells* on metallic or synthetic foils with > 20% PCE at the laboratory scale have been reported [7]. Prospectively by establishing the roll-to-roll deposition technique lower production costs could be achieved.

3. CIGSe shows a high *"resistivity" against impurities* [8, 9], wherefore minor requirements have to be imposed on the cleanliness of the production environment and the purity of source materials [10, 11].
4. The *radiation hardness* makes CIGSe solar cells attractive for space applications [12]. In combination with flexible substrates solar sails in space becomes imaginable, but also for earthbound applications like sails for deep-see vessels or sunshades.
5. *Aesthetics aspects* are the anthracite-hued visitation of CIGSe modules or the possibility of semi-transparent (flexible) solar cells, making CIGSe suitable for architectural configurations.

Thus, CIGSe implicates a high potential to filling gaps of the photovoltaic market, which cannot be satisfied by the current Si technology. This may even allow a higher cost-structure.
From the scientific point of view there are still fundamental open questions in despite of a more than 40 years ongoing CIGSe research history. Figure 1 shows a scanning electron microscopy (SEM) cross-section of a CIGSe solar cell with the typical layer sequence from top to bottom: Aluminium doped ZnO (AZO) / intrinsic ZnO (i-ZnO) / CdS / CIGSe / Mo / soda lime glass (SLG). Obviously the imperfect microstructure with small and large grains, vertical and horizontal grain-boundaries of the CIGSe absorber layer can be seen in Figure 1. It is still under debate, why the electronic properties of polycrystalline CIGSe solar cells with >22% PCE [13, 14] are at the same level or even beyond to their epitaxial counterparts with 19 – 20% PCE [15], [16, 17]. Would this imply an unexpected beneficial effect of grain-boundaries to the electrical quality of the absorber material? Some researchers mention that defects and impurities segregate at grain boundaries, resulting in a small defect density within the grain interior [18-20]. However, preponderantly the benign electronic properties of grain-boundaries like charge carrier transport enhancement channels or separation of electrons and holes preventing from recombination due to charge accumulation are considered as the main reasons for achieving high efficiency polycrystalline CIGSe solar cells [17, 21-23].
On the other hand owing to the complexity of the device structure with its numerous layers and interfaces (compare Figure 1) a sufficient modelling of the electronic cell properties is impeded [24]. In the case of the CIGSe layer this is aggravated by inadequately specified transport parameters like minority charge carrier lifetime and mobility. Hence, depending on the measurement conditions/techniques lifetimes in the range from 0.1 ns to several hundred nanoseconds [25, 26], as well as mobilities from 0.01 to 1000 $cm^2 \cdot V^{-1} \cdot s^{-1}$ are reported [27, 28]. In the case of time-resolved photoluminescence (TRPL) measurements Maiberg et al. [29],[Höl7],[Höl9] showed that the decay time observed on bare CIGSe layers does not

correspond directly to the "real" minority charge carrier lifetime. Thus experimental TRPL decay times of CIGSe absorbers are no direct indication for the quality of the resulting solar cells (under the assumption of a constant quality of the buffer/window layer stack). Reasons for this grievance are manifold and mostly intrinsically like i.e. electron trap states within the band gap, charge carrier separation due to internal electric fields, or spatially and energetically distributed recombination centres, influencing the shape and the duration of TRPL-transients. Thus, a firstly simple appearing measurement like the minority charge carrier lifetime with TRPL delivers entirely consistent results only by means of numerical simulation. This reflects the complexity of the polycrystalline CIGSe material system by itself.

That's why it is not surprising that the efficiency enhancement of CIGSe solar cells has been reached with more or less empiric methods [30]. For instance in the early 1990s the observation of the beneficial effect of alkaline metals – for the first time Sodium – to the CIGSe absorber material took place under lucky circumstances. An apriori parasitic incorporation of Sodium during the CIGSe growth process was effected by the usage of impure soda lime glass (SLG) substrates instead of costly highly pure substrates without Sodium [31]. Thus the promotional impact of Sodium on CIGSe solar cells is based on the cost-saving aspects of SLG rather than on a scientific motivation. The unintentional Sodium-doping of CIGSe layers conduced to an immense raise of the power conversion efficiencies. In 1993 Chen et al. [32] reported a record efficiency of 13.7% for devices without Sodium. While at the same time Hedström et al. [33] demonstrated 16.9% due to the incorporation of Sodium from the SLG substrate.

Later on, after 2010, the additional or substitutional incorporation of heavier alkaline metals (K, Rb, Cs) with specifically pre- and post-deposition techniques revealed a further enhancement of power conversion efficiencies [13, 34, 35]. In 2017 Solar Frontier achieved the prolonged highest efficiency of 22.9%[1] for solar cells fabricated under laboratory conditions [1]. However, the mechanisms behind the impact of alkaline metals on the electronic properties of CIGSe are not yet fully understood and highly discussed in the CIGSe community (section 2.1.3).

[1] For comparison the latest laboratory record efficiency of multi-crystalline silicon solar cells amounts 22.3% as well as 26.7% in the case of single crystal silicon [1].

## 1.1. Air exposure of CIGSe layers

One key factor of manufacturing high efficiency CIGSe solar cells is reported by Jackson et al. [36]. They improved their baseline efficiency by reducing the retention time of the uncovered CIGSe absorber in ambient air. It is usual during the laboratory and industrial manufacturing of CIGSe solar cells that the uncoated CIGSe layer comes into contact with the environmental atmosphere i.e. before and during processing the CdS buffer layer [37, 38].

TRPL-experiments of several groups revealed a strong reduction of the minority charge carrier decay times after air exposure of CIGSe layers [39-43]. Shirakata et al. [44] observed a decreasing steady state photoluminescence (PL) intensity in combination with diminishing TRPL decay times by progressive air exposure. Further, as compared to as-fabricated CIGSe layers they monitored with secondary ion mass spectroscopy (SIMS) for air exposed CIGSe layers an increased amount of Sodium, Hydrogen and Oxygen at the very CIGSe surface [44]. In this connection Heske et al. [45, 46] demonstrated with X-ray photoelectron spectroscopy (XPS) the formation of a Na–O–CIGSe complex after annealing at room temperature of CIGSe layers with co-adsorbed $H_2O$ and Na. Both groups suggested, based on their results, that the oxygenation of Sodium at the CIGSe surface induces recombination active defect states, reducing the PCE of the completed solar cell due to interface recombination. However, an experimental evidence for this suggestion has not been presented.

Metzger et al. [25, 40] bridged the gap between TRPL decay time degradation and solar cell impairment of air exposed CIGSe layers. They were able to refer a minority charge carrier lifetime reduction from 40 ns directly after fabrication to 0.3 ns after 21 h air exposure to a decreased PCE from 16% down to 5%, but without figuring out the mechanism behind solar cell deterioration [40].

Braunger et al. [47, 48] noticed that air humidity plays an important role during air exposure. They found a high impairment of PCE for completed solar cells with CIGSe absorbers exposed to humid air ($R_H$ = 100%, t = 20 d) at room temperature. Instead, cells with absorbers exposed to dry air at 200°C (t = 4 h) revealed an improvement of device performance. With XPS measurements they showed that surfaces of Sodium containing CIGSe absorbers exhibit oxides of Na, In, and Ga after dry air annealing. In comparison CIGSe surfaces without Sodium are not oxidized in dry air. In the case of humid air exposure, the oxygenation of all elements, except Cu, is independent from the Sodium content. Further the formation of elemental Se at the CIGSe surface is found and referred to the solar cell impairment [47].

## 1.2. Air-light exposure of CIGSe layers

Consequent upon the preceding results of air exposure experiments this thesis goes one step beyond and uncovers the decisive role of light during air exposure, named as air-light exposure (ALE). In the previous section the experimentalists investigated the influence of air exposure to CIGSe layers without consideration of the illumination state of the samples. A first indication of a light enhanced degradation of CIGSe layers due to illumination was reported by Metzger et al. in Ref. [25]. They observed during TRPL measurements an expedited reduction of minority charge carrier lifetime under high intense laser light excitation in ambient air. Further with steady state PL measurements Regesch et al. [49] pointed out that the decreasing quasi-Fermi level splitting due to air exposure is accelerated if the CIGSe layers are additively illuminated. In this study epitaxial grown CIGSe absorbers served as Sodium free references and exhibited identical reduction of the quasi-Fermi level splitting. For this reason, Regesch et al. excluded a critical role of Sodium on the degradation process [49].
In contrast the underlying hypothesis of this work is based on the participation of Sodium in ALE and is introduced by the following list.

1. Air-light exposure of bare CIGSe layers causes a physico-chemical modification of the CIGSe surface inducing recombination active states within the band gap at the surface. A crucial role during ALE plays Sodium.
2. The modification of the CIGSe surface after ALE survives the subsequent steps of solar cell fabrication and drives the completed device into interface recombination.
3. The illumination dependent metastability of CIGSe based hetero structures is accompanied with the migration of Sodium within the device, mainly the absorber. Thus the ALE impaired solar cell can be repaired due to sodium segregation at the CIGSe-CdS interface initiated by heat light soaking (HLS) under open circuit conditions.

The above mentioned hypothetical aspects were proven in chapter 4 of this cumulative thesis. The key challenge was to differentiate between enhanced surface or enhanced bulk recombination due to ALE in sections 4.1, 4.2, and 4.3. This could not be answered by XPS and TRPL measurements alone and required the deduction from interface recombination dominated solar cells towards surface recombination dominated absorber layers. The applied characterisation methods to absorbers and solar cells from different CIGSe batches with identical physico-chemical properties are introduced and discussed in chapter 3. Voltage

dependent admittance spectroscopy is a suitable method to characterize spatial narrow defect states like interface states and is thus examined more in detail in the subsection 3.2. Based on the measurement results of voltage dependent admittance spectroscopy a simulation model of the electronic device properties was introduced by *SCAPS 3.3.06* in 4.4. The intention of this model is to uncover the electronic properties of interface states in devices with air-light exposed absorbers. In the following section 2 the physical fundamentals of chapter 3 and 4 are given. A conclusion of the thesis is drawn in chapter 5, suggestions for prospective investigation methods with preliminarily results are compiled in chapter 6.

# 2. Fundamentals

This section deals with the physical background of the functionality of solar cells and the basics for the investigative study of the ALE effect on CIGSe layers and solar cells in this work. First, section 2.1 outlines the fundamental properties of $Cu(In,Ga)Se_2$ solar cells. Subsequently, in section 2.2 the principles of a p-$n^-$-n-$n^+$-hetero-junction are examined by means of a hypothetic hetero-structure given in Table A - 4. Finally section 2.3 gives an overview about the loss mechanisms in CIGSe solar cells.

## 2.1. $Cu(In,Ga)Se_2$-based solar cells

In the following section the material properties of the investigated thin film solar cells are presented. The structure and the fabrication methods are demonstrated in section 2.1.1 on the basis of a standard laboratory cell manufactured at the Martin-Luther-University (MLU). Subsequently, in sections 2.1.2 - 2.1.5 the specifics of the object of interest in this work, namely the CIGSe absorber are examined more in detail. The chapter will be closed with an overview of the possible recombination domains for this type of solar cell in section 2.3.

### 2.1.1. Architecture and preparation techniques

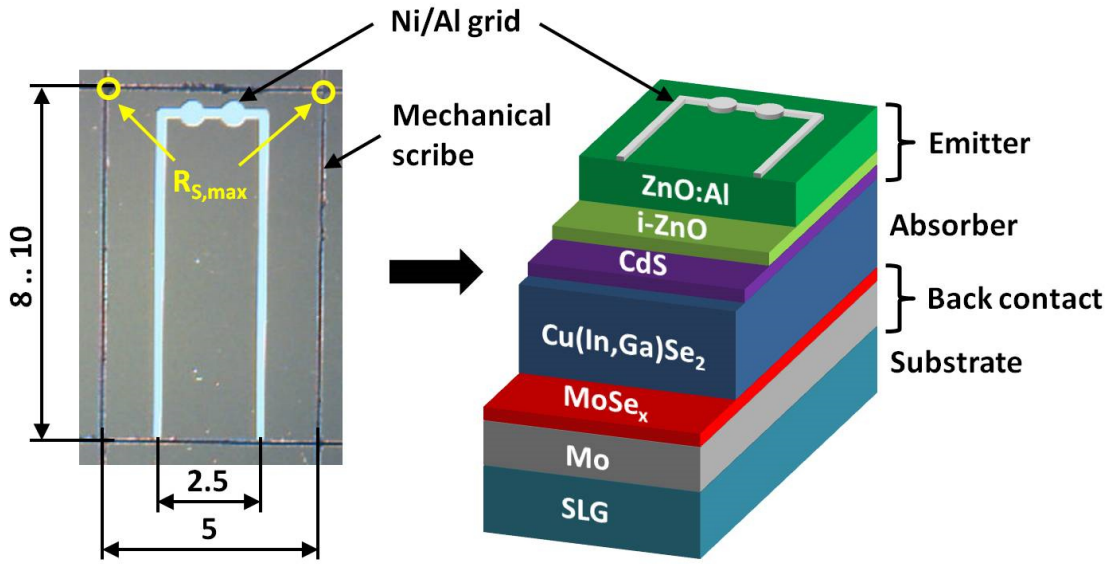


**Figure 2** Left hand side: Topview of a thin film solar cell manufactured at the MLU and defined by mechanical scribing. Stated dimensions are in units of mm. Right hand side: A not true to scale schematic depiction of the layer stack. Thickness specifications of the films are written within the text.

The left hand side of Figure 2 presents the top view of a typical $Cu(In,Ga)Se_2$ thin film solar cell fabricated at the MLU. Next to it on the right hand side of Figure 2 is a schematic sketch of the underlying layer stack. The functionalities and characteristics of each layer are briefly declared in the following subsections, more detailed descriptions can be derived from the literature [50-53].

*Molybdenum coated SLG substrate*

Next to the budget-friendly availability a further advantage of soda lime glass (SLG) is the very well matching thermal expansion coefficient with respect to Mo and CIGSe. With a fraction of ≈ 15% $Na_2O$ the incorporation of Na into the CIGSe layer via diffusion from the SLG substrate is a long-standing standard method (see section 2.1.3). Coating of 1 to 3 mm SLG slices with 0.5 to 1 µm Mo is usually performed by sputtering, less common by thermal evaporation. Reasons, why Molybdenum serves as the back-contact, are due its stability in a Selenium atmosphere, no incorporation into the CIGSe layer and cost effectiveness [50]. However, during the In,Ga rich growth (i.e. the first stage in Figure 3) of the CIGSe absorber the formation of $MoSe_x$ ($x \approx 2$) at the Molybdenum surface takes place [54]. This reaction is further catalyzed by the presence of Na [55, 56]. Typical $MoSe_x$ thicknesses from 10 to 100 nm are observed forming an interfacial layer between CIGSe and Mo [55, 57, 58].

*$Cu(In,Ga)Se_2$ absorber layer*

There exist manifold variants of manufacturing CIGSe thin films with the aim to improve the cost effectiveness or process stability. Thus, several deposition techniques have been demonstrated from selenization of sputtered In, Ga and Cu layer stacks, over inkjet printing through to electro deposition [52]. However, the co-evaporation of the elemental constituents is the common method applied in various laboratories [4]. As well, co-evaporation can be categorized into subgroups like 1-stage, 2-stage or 3-stage processes [50, 52].
In the following the 3-stage process, shown in Figure 3, is described more in detail, because this is the standard technique of growing CIGSe absorbers at the MLU [59]. The 3-stage process was invented by the *National Renewable Energy Laboratory* (NREL) in the mid of the 1990's [60]. During the first stage a $(In,Ga)_xSe_y$ ($x \approx 2$, $y \approx 3$) precursor is formed by evaporating elemental In and Ga under Selenium excess. In the second stage the deposition of In and Ga is intermitted and Cu + Se is supplied until the CIGSe layer becomes copper rich $[Cu]/([In] + [Ga]) = CGI > 1$. For an enhanced copper diffusion the substrate temperature is increased close to the softening point of the SLG substrate (at the MLU: $T \approx 625$ °C).

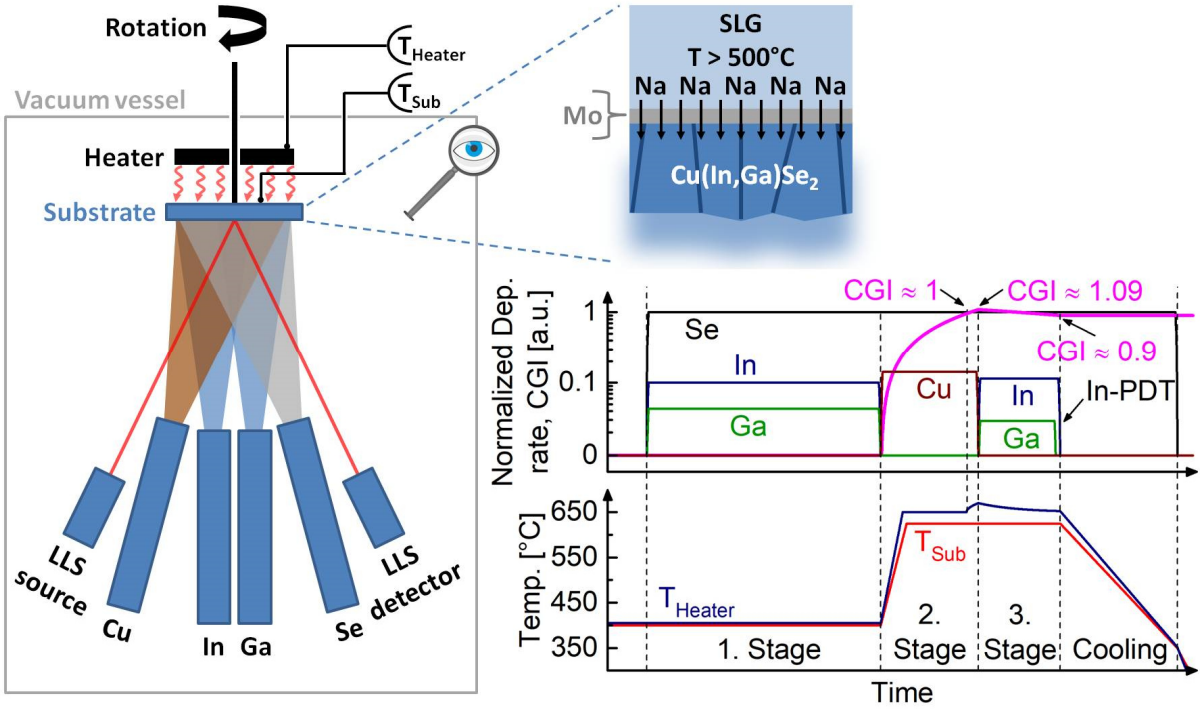


**Figure 3** Left hand side: Principle of the co-evaporation process technique for manufacturing $Cu(In,Ga)Se_2$ absorber layers. Copper fraction within the CIGSe layer becomes controllable with a laser light scattering (LLS) system and by monitoring the temperature of the substrate heater ($T_{Heater}$). Right hand side: Magnification of the substrate, illustrating the incorporation of Sodium from the SLG substrate into the growing CIGSe layer at high process temperatures and the time regime of the 3-stage process. The deposition rates are normalized to the Se-rate.

Ordinarily, the CGI should not exceed 1.09 at the end of the second phase to achieve high quality solar-grade CIGSe layers at the end [61]. In the third stage the final copper poor composition of CGI ≈ 0.9 is defined by evaporating again In + Ga + Se in the absence of a Cu-flux. Additionally, at the end of the 3rd phase a finishing is performed by depositing a few atomic layers of In + Se (In-PDT) [62]. Afterwards, the sample cools down to 350 °C under Se supply and thereafter in vacuo to room temperature [59]. For composition control during growth visible red laser light scattering (LLS) is utilized, indicating the stoichiometric points (CGI = 1) by knees in the monitored curves of the scattered light intensity. The reason for an altered scattering amplitude is the formation and vanishing of a quasi-liquid $Cu_xSe$ ($x \approx 2$) phase changing the optical properties and morphology of the CIGSe surface [63]. It is presumed that $Cu_xSe$ enhances diffusion processes for recrystallisation. Monitoring the temperature (heating power) of the substrate heater as depicted in Figure 3 supports the signal processing of the LLS system. With infra-red LLS ($E_{ph} < E_{g,CIGSe}$) the thickness of the grown CIGSe layer becomes determinable.

*CdS buffer layer*

The emitter stack of the completed solar cell in Figure 2 begins with a CdS layer of usually 50 nm thickness. Providing CIGSe with a CdS coating is performed in general by the chemical bath deposition (CBD) technique, due to its reliability of achieving highly efficient solar cells [52]. Reasons are founded on (1) closed dense layers even for layer thicknesses in the range of 10 nm [64] as well as (2) the removal of natural oxides from the CIGSe surface [50, 65]. The parent substances for the CdS-CBD process are $Cd(CH_3COO)_2$ (cadmium acetate), $CH_4N_2S$ (thiourea) and $NH_4OH$ (ammonia solution) dissolved in water. At the beginning of the deposition process the CIGSe samples are embed into the solution at room temperature (cold start [50]). Subsequently, the beaker with solution + samples is immediately inserted into a water bath of 60 °C. After 8 min a ca. 50 nm thick CdS layer has been formed and the deposition process is interrupted by taking out the samples from the beaker. Abundant residuum on the CdS surface is rinsed off with deionised water and the samples are dried with a nitrogen stream. The heterogeneous CdS growth is constituted by the following chemical equation [66]:

$$Cd(NH_3)_4^{+2} + SC(NH_2)_2 + 2OH^- \rightleftarrows CdS + CN_2H_2 + 4NH_3 + 2H_2O. \quad \textbf{2.1}$$

The functionality of the CdS buffer layer are after [50] (section 5.2.8) and [53] (section 7.3.4):

1. Protecting the CIGSe surface (hetero junction) against chemical reactions or damages initiated by the ZnO deposition process.
2. Type inversion of the CIGSe near-surface region either due to diffusion of Cd into the CIGSe, creating $Cd_{Cu}$ donor states or due to the removal of natural oxides, leaving positive charged states behind at the very CIGSe surface.
3. Making the provisional product CIGSe + CdS storable and transportable even under ambient conditions.
4. Passivation of recombination active surface states by impurities like oxygen or hydrogen.

Attaching to bullet item 3, it has been revealed that ALE of CdS covered CIGSe layers does not diminish the quality of completed solar cells.

Unfortunately CdS has a direct band gap of $E_{g,CdS} \approx 2.4$ eV, limiting the quantum efficiency of solar cells within the short wavelength range of the solar spectrum. Further, the bad

reputation of Cadmium motivates the research of alternative buffer layers like Zn(O,S), (Zn,Mg)O and $In_2S_3$ to mention the established ones [4, 67, 68].

*ZnO window and Ni/Al metal grid*

A bi-layer consisting of 50 – 100 nm high-resistance undoped i-ZnO (i denotes intrinsic) and 350 – 400 nm low-resistance Al-doped ZnO:Al finalises the emitter of the solar cell in Figure 2. In general film deposition is realised via sputtering methods of pure ZnO and ZnO:$Al_2O_3$ targets. Both layers exhibit a high transparency in a wide range of the solar spectrum due to the ZnO's wide band gap of $E_{g,ZnO} \approx 3.3$ eV. It is proposed by Rau and Schmidt [69] that the low lateral conductivity of i-ZnO separate inferior operating locations or micro-shunts from higher performing regions of the solar cell, resulting in increased fill factor and open circuit voltage. The role of the highly conductive ZnO:Al is to ensure a loss-free transport of the collected photo current to the grid fingers. Prerequisite in that case is a high doping level. However, if the Al doping concentration of ZnO:Al reaches the percentage range, light absorption by free carriers comes into play. Increasing the ZnO's absorptivity of longer wavelengths ($\lambda \geq 1$ µm) and reducing the solar cell's quantum efficiency in this spectral range [50]. Thus, electrical and optical properties have to be balanced for solar grade ZnO:Al layers. Considering a homogenous ZnO:Al layer with a free carrier concentration of $n = 5 \cdot 10^{20}$ $cm^{-3}$ and a mobility of $\mu_n = 20$ $cm^2 \cdot V^{-1} \cdot s^{-1}$ then with the conductivity $\sigma = q \cdot \mu_n \cdot n$ the specific resistance results to $\rho_s \approx 6 \cdot 10^{-4}$ Ω·cm, which is 4 orders of magnitude higher than the resistivity of aluminium or copper. The region of maximum series resistance $R_{s,max}$ is indicated by the yellow open circles in Figure 2 located at the top corners of the solar cell, approximately 1.5 mm away from the metal grid. Additionally, further the series resistance is increasing towards the left and right edges as well as towards the middle of the two longer grid fingers. Due to variable current paths the calculation of the local dependent series resistance is not trivial and treated further in section 3.2.

The metal grid is deposited by thermal evaporation in vacuum and consists of a 50 nm Ni layer followed by a ca. 1.5 µm Al layer and finally again a 50 nm Ni cap-layer. Improved adhesion and prevention to the formation of $Al_2O_3$ at the ZnO/Al interface is ensured by the first Ni coating. Capping the Al layer with a second Ni layer increases the resilience of the metal grid to injuries by contacting the solar cell with measurement probes for electrical characterisation.

### 2.1.2. Basic properties of Cu(In,Ga)$Se_2$ absorber layers

Cu(In,Ga)$Se_2$ is a I-III-$VI_2$ compound semiconductor and crystallises in the tetragonal chalcopyrite structure, depicted in Figure 4 a). This structure type can be deduced by stacking 2 unit cells of the zinc blende (ZnS) structure on top of each other. Thus, the ratio of the lattice constants in Figure 4 a) results to c/a ≈ 2. Due to the different binding strength of Cu-Se and (In,Ga)-Se the tetragonal arrangement is distorted and the c/a-ratio amounts ≈ 2.01 for CISe and ≈ 1.96 for CGSe [70, 71]. Further, it can be derived from Figure 4 a) that the coordination number of each element is 4. Hence, the metal atoms (Cu, In, Ga) hold 4 bonds with Selenium, whereas every Se atom holds 2 bonds with 2 different Cu atoms and further 2 bonds with 2 different group-III atoms. The valence band is formed by hybridisation of the Cu 3*d*- and Se 4*p*-orbitals. Group-III *s*-orbitals and Selenium *sp*-hybrid states provide the conduction band. At the Γ-point in the centre of the Brillouin zone the valence band maximum and conduction band minimum can be found, allowing a direct transition for the smallest energy gap [16, 50, 72].

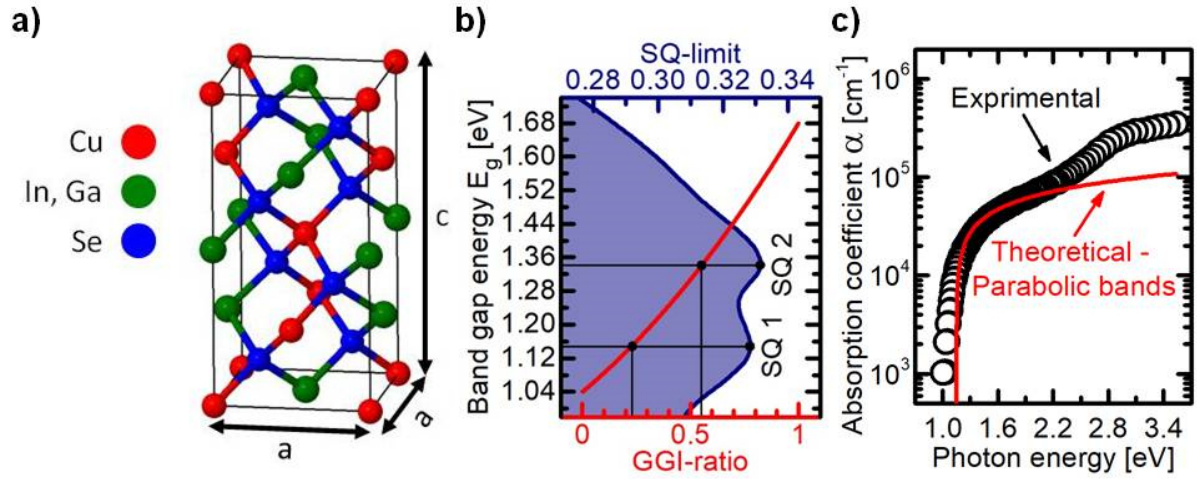


**Figure 4** (a) Unit cell of the tetragonal chalcopyrite structure compiled with the software *PDF4* using ICDD-No./Ref.: 04-016-4109. (b) Band gap energy as a function of the GGI-ratio calculated after equation 2.2, with SQ 1 at $E_g$ = 1.15 eV, GGI = 0.23 and SQ 2 at $E_g$ = 1.34 eV, GGI = 0.55 matching the local maxima of the Shockley-Queisser limit, drawn up with computed values tabulated in Ref. [73]. (c) Theoretical approximated optical absorption coefficient with equation 2.3 for an optical band gap of $E_g$ = 1.15 eV (GGI = 0.23). For comparison experimental data from spectroscopic reflectance and transmittance measurements examined on a CIGSe layer with 250 nm thickness and a GGI-ratio of 0.23 in Ref. [74].

*Material composition*

As previously mentioned, solar grade CIGSe layers are fabricated with a final Cu-poor composition (CGI ≈ 0.9). This causes an intrinsic p-type doping of the CIGSe material due to the formation of shallow acceptor states in the form of copper vacancies $V_{Cu}$. Typical doping densities are in the range of $10^{15}$ to $10^{17}$ $cm^{-3}$ [75-79], by contrast for a CGI-ratio of 0.9 the stoichiometry would account for a density of $V_{Cu} \approx 10^{21}$ $cm^{-3}$. Hence, the formation of compensating donor states like $In_{Cu}$ or $Ga_{Cu}$ antisites in Table 1 are imaginable. However, $V_{Cu}$ exhibits the lowest formation energy of the latter impurities under Se excess growth [80-82], and thus the CIGSe layer becomes intrinsic p-type with doping densities conformable to solar cell applications.

For CIGSe there is no miscibility gap with regard to Indium and Gallium, wherefore elemental ratios of [Ga]/([Ga] + [In]) = GGI = 0 .. 1 can be arbitrary adjusted. Correspondingly the band gap can be varied in the range from 1.04 eV for CISe (GGI = 0) to 1.68 eV for CGSe (GGI = 1). The band offsets $\Delta E_{V,C}$ between CISe and CGSe are obtained by first-principle calculations with $\Delta E_V \approx 0.04$ eV and $\Delta E_C \approx 0.6$ eV [82]. Hence, the Ga content in CIGSe effects mainly the position of the conduction band. The band gap energy as a function of the Ga content can be given by the following equation [83]:

$$E_g(x) = (1 - x) \cdot 1.04eV + x \cdot 1.68eV - b \cdot x \cdot (1 - x) \qquad \textbf{2.2}$$

where x denotes the GGI-ratio and b ≈ 0.21 eV the bowing parameter. As depicted in Figure 4 b) this gives the ability to tune the CIGSe band gap in terms of matching the local maxima of the Shockley-Queisser (SQ) limit. The SQ limit is derived from the principle of detailed balance of single junction solar cells and qualifies the highest achievable power conversion efficiency as a function of the band gap energy [84]. Recent calculation of the SQ limit considering an air mass spectrum of AM 1.5 G[2] reveals 2 local maxima in Figure 4 b) with 32.85% for $E_g$ = 1.15 eV (SQ 1) and 33.16% for $E_g$ = 1.34 eV (SQ 2) [73].

[2] The AM 1.5 G spectrum defines the spectrum of solar light after passing through 1.5 thicknesses of the atmosphere directly and an additional fraction of scattered light. Thus, compared to direct irradiation (AM 1.5 D) the AM 1.5 G spectrum reveals an increased intensity in the short wave length range. The calculation of the detailed balance limit was conducted by Shockley and Queisser with the simplification of a 6000 K black body spectrum, modelling the solar light. This assumption delivers 1 maximum at 30.66% power conversion efficiency for $E_g$ = 1.32 eV and an overestimation of the efficiency limit for $E_g$ > 2 eV. Instead, using the AM 1.5 G spectrum 2 maxima with increased efficiencies appear, caused by characteristic absorption lines and high extinction of the ultra violet spectral range [73].

Apart from the SQ-limit, commonly CIGSe solar cells with an integral GGI-ratio in the range of ≈ 0.3 reveal the highest conversion efficiencies. Increasing the Ga content further usually degrades the solar cell efficiency, which can be referred either to higher recombination losses within the bulk caused by $Ga_{Cu}$ antisites or an unfavourable band alignment and Fermi-level position at the CIGSe/CdS interface [85-89].

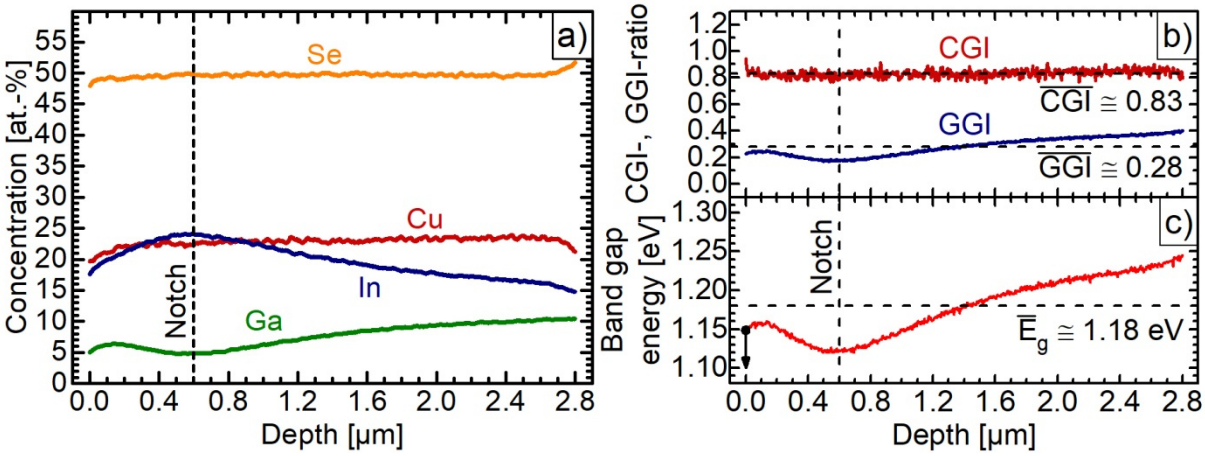


**Figure 5** (a) GDOES-measurement of the depth dependent elemental concentrations obtained on a MLU standard CIGSe sample. (b) CGI- and GGI-ratio deduced from the elemental concentrations of (a). (c) Band gap energy $E_g$ as a function of depth calculated with the GGI-ratio in (b) and equation 2.2.

A noteworthiness of CIGSe layers fabricated with a 3-stage process is the self-adjusted V-shaped depth dependent Ga and In concentrations. Figure 5 b) shows the GGI-ratio as a function of depth obtained on a MLU standard CIGSe sample by glow discharge optical emission spectroscopy (GDOES). With equation 2.2 the band gap energy and in particular the energetic position of the conduction band varies likewise with the GGI-ratio in Figure 5 c). Reason for the graded band alignment is the sequence arrangement of the 3-stage process. During the 2nd stage reaction of Cu + Se with the $(In,Ga)_2Se_3$ precursor causes a directed diffusion of Cu-atoms towards the back contact and in the 3 rd phase an opposite diffusion of Cu towards the surface. Migration of Cu depends on film stoichiometry and temperature. The movement of Cu is ensued either over vacancies $V_{Cu}$ (Cu-poor) or via interstitial lattice sites $Cu_i$ (Cu-rich) [90]. In the same way a diffusion of In and Ga to make space for the incorporation of copper takes place. By ab-initio calculations Witte et al. [91] came to the conclusion that the diffusion barrier of Ga in CISe is distinctly above the diffusion barrier of In in CGSe, which is assigned to the different ionic radii of Ga and In [91]. This may explain the observation of Schroeder et al. [92] that Ga diffusion is effected by metal vacancies with $V_{Cu}$ in the Cu-poor phase and $V_{In}$ in the Cu-rich phase. Further the In-diffusibility is found to

be higher than the Ga-diffusibility in the CISe host lattice [93]. Hence, the In atoms are more probably driven to the surface due to the incorporation of Cu and a maximum of In-concentration at the notch-position in Figure 5 a) exists. The opposite case can be observed for the Ga-concentration in Figure 5 a). However, in spite of a V-shaped GGI-profile the band gap energy at the surface can be estimated to $E_g \approx 1.15$ eV as indicated by the arrow at zero depth in Figure 5 c).

*Effective density of states*

The theoretical absorption coefficient $\alpha(\hbar\omega)$ of CIGSe (GGI = 0.23) in Figure 4 c) was computed with equation 2.3. This equation is derived in Ref. [94] from the excitation probability of electrons within the valence band into the conduction band by photons.

$$\alpha(\hbar\omega) = \frac{(2m^*_{comb})^{\frac{3}{2}}}{2\pi\varepsilon_0 c_0 n} \cdot \frac{q^2 p^2}{\hbar^2 m_0^2} \cdot \frac{1}{\hbar\omega} \left(\hbar\omega - E_g\right)^{\frac{1}{2}} \qquad \textbf{2.3}$$

After Ref. [95] the matrix element $p^2$ can be obtained from the following relation $p^2 = m_0/2 \cdot \hbar\omega\left(m_0/m^*_{comb} - 1\right)$, where $m^*_{comb} = \left(1/m^*_n + 1/m^*_p\right)^{-1}$ is the combined effective mass within the conduction band $\left(m^*_n\right)$ and the valence band $\left(m^*_p\right)$. For the theoretical absorption coefficient in Figure 4 c) the effective masses were fixed to $m^*_n = 0.1 \cdot m_0$ and $m^*_p = m_0$ with $m_0$ the mass of free electrons. Further material parameters in equation 2.3 are $E_g = 1.15$ eV the band gap energy and n = 3 the refractive index. Physical constants in equation 2.3 are $\varepsilon_0$ the dielectric constant, $c_0$ the vacuum velocity of light, q the elemental charge and $\hbar$ the reduced Planck constant. The photon energy is given with the angular frequency by $\hbar\omega$.

Measurements of Weinert et al. [96] and calculations by Persson [97] confirm the fairly good estimation of $m_n \approx 0.1 \cdot m_0$ and a nearly isotropic character of $m_n$ at the Γ-point. On the other hand the hole mass shows a high anisotropy at the Γ-point due to the non-degeneracy of the valence bands in this point [16, 97]. However, the theoretical curve in Figure 4 c) fits well to the experimental data [74] in the range of 1.2 to 2 eV, accordingly the approximation of $m_p \approx m_0$ should be appropriate for electrical simulations of CIGSe solar cells. Hence, the effective densities of states of the CIGSe material system can be evaluated to $N_C \lesssim 10^{18}$ cm$^{-3}$ and $N_V \gtrsim 10^{19}$ cm$^{-3}$. In the case of higher photon energies > 2 eV a deviation of theoretical and experimental data in Figure 4 c) is attributed to the modified band curvature for high $\vec{k}$ values; especially the valence band drifts abruptly away from the parabolic approximation [16].

On the other hand, absorption of photons with energies below the band gap energy can be ascribed to Urbach tails due to lattice distortion by thermal vibrations of atoms. Both scenarios can be regarded by extension of equation 2.3 with semi-empirical quantities (see Ref. [50] section 4.2.4).

*Defect properties and non-radiative recombination*

As listed in Table 1, there is a plethora of possible intrinsic point defects within the CIGSe lattice. Hence, it can be assumed that defect related recombination plays a crucial role on the efficiency of CIGSe solar cells. For the Cu-poor material the preferential defect formation of group-III metals on copper sites denoted with $III_{Cu}(0/+1)$ and $III_{Cu}(+1/+2)$ as well as the defect complex $(In_{Cu} + V_{Cu})(0/+)$ can be taken into account. In the case of stoichiometric or Cu-rich material the formation possibility of Cu-interstitials $Cu_i$ as well as $Cu_{III}$ antisites should increase. Calculated transition energies of defects caused by extrinsic dopants or impurities are given in the theoretical studies of Refs. [98-103].

**Table 1** Overview of intrinsic point defects within the CIGSe lattice.

| Defect | Type | Transition | Defect level $E_d$ | | Reference |
|---|---|---|---|---|---|
| | | | CISe (III = In) | CGSe (III = Ga) | |
| $V_{Cu}$ | Acceptor | 0/–1 | $E_V$ + 0.03 eV | $E_V$ + 0.01 eV | [80, 82, 104] |
| $V_{III}$ | Acceptor | 0/–1 | $E_V$ + 0.17 eV | $E_V$ + 0.19 eV | [80, 82] |
| | | –1/–2 | $E_V$ + 0.41 eV | $E_V$ + 0.38 eV | |
| $Cu_{III}$ | Acceptor | 0/–1 | $E_V$ + 0.29 eV | $E_V$ + 0.29 eV | [80, 82, 105, 106] |
| | | –1/–2 | $E_V$ + 0.58 eV | $E_V$ + 0.61 eV | |
| $III_{Cu}$ | Donor | 0/+1 | $E_C$ – 0.25 eV | $E_C$ – 0.49 eV | [80, 82, 107-110] |
| | | +1/+2 | $E_C$ – 0.34 eV | $E_C$ – 0.69 eV | |
| $Cu_i$ | Donor | 0/+1 | $E_C$ – 0.20 eV | $E_C$ – 0.21 eV | [80, 82, 108, 111] |
| $In_{Cu} + V_{Cu}$ | Donor | 0/+1 | $E_C$ – 0.20 eV | – | [80, 108, 111] |

Recombination over trap states within the band gap is treated by the Shockley-Read-Hall (SRH) formalism. Both, radiative and non-radiative trapping processes of charge carriers within the bands are included in the SRH-theory [112]. For solar cells non-radiative recombination is more critical than radiative recombination due to the generation of heat during this recombination process. In theory non-radiative transitions are dominating in the case of a strong electron-lattice coupling [113]. Hence, the energy surfaces of the excited and ground state for a recombination centre are displaced in the configurational coordinate diagram and contact or even intersect each other [114]. Accordingly, reaching the pitch point of the energy surfaces the excited centre can change over to the ground state as shown for the $V_{Se}^{2+} \rightarrow V_{Se}^{0}$ transition in CISe by Wei and Zhang [115]. Subsequently, due to multi-phonon interactions the centre relaxes into the equilibrium configuration of the ground state [116]. A quantitative dimension of non-radiative recombination in CIGSe can be obtained by the external quantum efficiency $\eta_{ext}$ of i.e. electroluminescence (EL) or photoluminescence (PL) measurements at room temperature. The internal luminescence efficiency $\eta_i$ is given by Ref. [117] to:

$$\eta_i = \frac{\tau_{nrad}}{\tau_{nrad} + \tau_{rad}} \approx \frac{\tau_{nrad}}{\tau_{rad}}, \qquad \tau_{rad} \gg \tau_{nrad} \tag{2.4}$$

where $\tau_{nrad}$, $\tau_{rad}$ denote the lifetimes due to non-radiative and radiative recombination, respectively. Typical external luminescence efficiencies of CIGSe solar cells with PCE's from 19% to 20% lie in the range of $\eta_{ext} \approx 3 \cdot 10^{-4}$ .. $2 \cdot 10^{-3}$ [118, 119]. Approximating a radiative recombination coefficient of $B \approx 5 \cdot 10^{-11}$ $cm^3 s^{-1}$ (confirmed by the measured absorption data in Figure 4 c)) and a net doping concentration of $p_0 \approx 10^{16}$ $cm^{-3}$ then the radiative lifetime can be approximated with $\tau_{rad} = (B \cdot p_0)^{-1} = 2$ µs. Thus, with the above mentioned external quantum efficiencies and equation 2.4 a lower limit of the non-radiative lifetime can be expected in the range of $\tau_{nrad} \approx 0.5$ .. 5 ns. An upper limit of $\tau_{nrad}$ results to 50 ns under the assumption of an insufficient light emission with $\eta_{ext} \approx 0.1 \cdot \eta_i$ as observed on silicon solar cells [117].

*Charge carrier mobilities*

An important role on device simulations plays the mobility of charge carriers, especially in the case of re-modelling admittance measurements. The measured hole and electron mobilities – as pointed out in chapter 1 – range over several orders of magnitude from 0.01 to 1000 $cm^2 \cdot V^{-1} \cdot s^{-1}$ [27, 28, 120-123]. In consideration of numerous microstructural

imperfections of CIGSe layers scattering at ionized or neutral impurities should dominate the hole and electron mobilities. A compilation of temperature dependent hole mobilities measured by several groups in Ref. [120] reveals (1) a distinct higher hole mobility for single crystal samples with $\mu_p = 100 .. 1000\ cm^2 \cdot V^{-1} \cdot s^{-1}$ than for polycrystalline layers with $\mu_p = 0.1 .. 10\ cm^2 \cdot V^{-1} \cdot s^{-1}$, which is also confirmed by the results of Ref. [122]. And (2) the temperature dependence of the hole mobility for single crystal CIGSe follows an $T^{-3/2}$ trend as in the utilized simulation model of Paper 4 in section 4.4. The maximum of the hole mobility is found to be at temperatures of $T \lesssim 150$ K. However, in the case of polycrystalline films no general tendency of the hole mobility varying with temperature can be observed [120].
The reduced mobilities of polycrystalline samples are ascribed to grain boundaries, acting as barriers especially in the case of lateral current transport like in Hall measurements [122]. But also time of flight (TOF) or voltage dependent TRPL measurements with dominating vertical transport reveal electron and hole mobilities not exceeding the upper limit of $5\ cm^2 \cdot V^{-1} \cdot s^{-1}$ [120, 121].

### 2.1.3. Impact of Sodium

As implied in chapter 1, doping of CIGSe layers with alkaline metals (here Sodium) is a crucial process element to achieve high efficiency thin film solar cells. The mechanisms behind the beneficial effects of Sodium are not fully understood. It is ensured that Na increases the majority charge carrier density of CIGSe films by more than 1 order of magnitude [9, 124-126]. Even epitaxial grown CIGSe layers reveal a higher p-conductivity due to Na incorporation [15, 127]. There exist several models to describe the principles of the Na doping effect:

1. Neutralizing of compensating donor defects at interfaces, grain boundaries or lower-dimensional lattice defects within the bulk. Either by hindering the formation of donor defects like $In_{Cu}$ due to occupation of $V_{Cu}$ during growth [19, 128] or by reducing the amount of $V_{Se}$ due to a higher incorporation of Se via $NaSe_2$ as well as a Na-catalyzed oxygenation of $V_{Se}$ creating $O_{Se}$ acceptor states in contact with ambient air [48, 129-131].
2. Formation of acceptor-like impurity levels by occupation of lattice sites like $Na_{In}$ or $Na_{Se}$. However, $Na_{Se}$ is energetically levelled nearly below the conduction band edge

giving an inefficient acceptor level [99, 100]. Thus, it can be considered that neutralizing $V_{Se}$ outweigh the enhancement of p-type doping due to $Na_{Se}$.

3. As has been shown by Yuan et al. [132] the solubility of Sodium within the CIGSe crystal system is increased at high process temperatures (T ≳ 400 °C). The soluble Sodium concentration

$$c(Na) = N_s exp\left\{\frac{\Delta H}{k_B T}\right\} \quad \textbf{2.5}$$

is determined by the available sites $N_s$ of the host system, the formation energy ΔH and the temperature T. Occupation of copper vacancies $Na + V_{Cu} \rightarrow Na_{Cu}$ shows the lowest formation energy. According to equation 2.5 during cooling down to room temperature the solubility of Sodium declines, and precipitation of Na at interfaces or grain boundaries takes place. Hence, an increased amount of $V_{Cu}$ is existent within the bulk, scaling up the majority charge carrier density [132].

As previously mentioned the formation of $MoSe_x$ at the back contact is promoted by Na, further effects due to Na-doping are listed below.

1. CIGSe films grown in the presence of Na tend to prefer the desired 112-orientation [133], resulting in a higher saturation current density compared to films with a preferred 220/204-orientation [134].
2. Sodium expands the α-phase region of the binary CIGSe phase diagram towards lower copper concentrations [53].
3. Due to the formation of $Na_2Se_x$ during the deposition process the development of the CIGSe phase is decelerated [135], but on the other hand the incorporation of Se is increased [136], reducing likewise the emergence of compensating $V_{Se}$ defects.
4. Sodium impedes the Ga-In interdiffusion during the growth process, resulting in a more pronounced Ga gradient for films grown in the presence of Na [137].

### 2.1.4. Incorporation of Sodium

Commonly doping CIGSe with Sodium is performed through to 3 different methods with: (1) diffusion from the SLG substrate, (2) pre-deposition of a NaF precursor and (3) post-deposition of NaF directly afterwards the CIGSe growth process.

*1. Diffusion from the SLG substrate*

This technique requires high substrate temperatures close to the softening point of the SLG [48]. By analogy with Figure 3 during the MLU standard process this condition is reached at the beginning of the second stage, where the substrate temperature is heated up from 400°C to 625°C. The first barrier for the out-diffusing Na ions is the Mo back contact. It is presumed that the transport of Na ions takes place over Mo grain boundaries [50]. Therefore, the sputter conditions of the Mo layers effectuate the incorporation of Sodium into CIGSe layers. Optimal electronic properties of CIGSe solar cells are obtained with a Sodium content of 0.1 at.-% [138, 139]. To achieve this optimum of Na-concentration it is either necessary to adapt the Mo layer to the CIGSe growth process or vice versa [140, 141].

*2. NaF precursor*

The usage of alternative substrates without Sodium or lower process temperatures necessitates other strategies for incorporation of Sodium. One possibility is given by evaporating a thin NaF precursor in the range of few to multiple ten nano-meters on top of the Mo back-contact before starting the CIGSe deposition process. Similar to the SLG technique, the presence of Sodium during formation of the CIGSe film influences the film structure (preferred 112-orientation) and enhances grain growth [142, 143].

*3. NaF post-deposition treatment (PDT)*

Actually to allow Ga diffusion at low substrate temperatures Rudmann et. al. [137] invented the PDT-technique. In that case after processing the CIGSe film an additional deposition sequence follows by evaporating NaF + Se on top of the CIGSe surface, where the in-diffusion of Sodium takes place. The additional Selenium flux forestalls the loss of Selenium and its compounds of the CIGSe layer during PDT. Figure 6 shows the beneficial impact of Na-PDT on the TRPL-lifetime of a bare CIGSe layer even after an exposition period of 1 day to ambient air before Na-PDT. On the other hand shows Figure 6 the detrimental impact of ALE on the TRPL-lifetime after Na-PDT. Instead, no reduction of the TRPL-lifetime is observable in the case of CIGSe layers without Na (not shown).

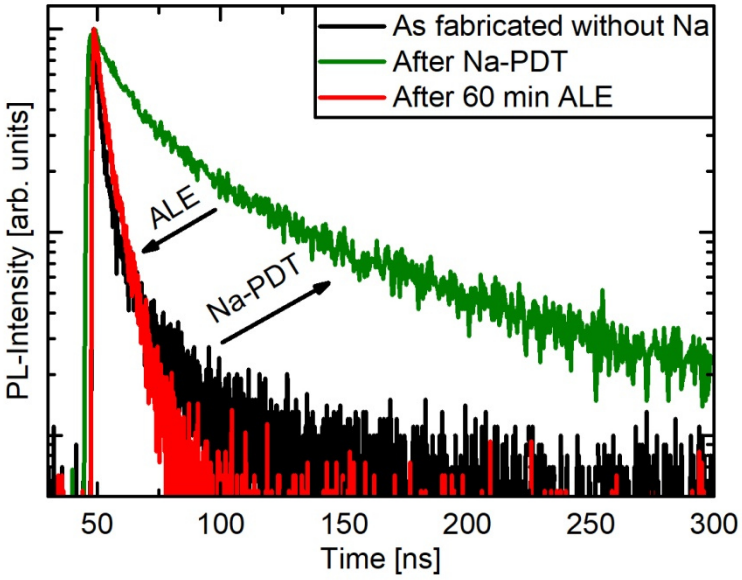


**Figure 6** Impact of Na-PDT and ALE on the photoluminescence transient behaviour of a very same CIGSe sample. Na-PDT was performed after 1 day storage time of the bare CIGSe layer in ambient air and darkness.

### 2.1.5. Metastable properties

A unique characteristic of CIGSe solar cells is the occupation of different states depending on the history of illumination. Usually the J-V-parameters of completed solar cells are improving after light-soaking (LS), which is explained by an increased doping density of the CIGSe film [144]. The metastable relaxation of the solar cell takes place during dark annealing (DA) at room temperature or above. LS with red light[3] below the absorption edge of the CdS film gives the ability to separate the light induced modification of the absorber layer from the light induced modification of the buffer/window layers. In the following the widely accepted metastability model of Lany and Zunger [145] is introduced. This model is based on the configurational change of the di-vacancy complex ($V_{Se}$–$V_{Cu}$) due to the following reactions with holes ($h^+$) or injected electrons ($e^-$).

[3] Next to the red light effect there exists also a blue and white light effect, implying metastable properties as well for the emitter layers. However, not only light causes metastable changes of CIGSe devices, correspondingly similar modifications of CIGSe solar cells are observed under voltage biasing in forward direction (≈ light soaking) and in reverse direction (≈ dark annealing) For further information see Ref. [50] sections 6.2.4.3 – 6.2.4.7.

$$(V_{Se} - V_{Cu})^{+} + e^{-} \xrightarrow{\Delta E \approx 0.1eV} (V_{Se} - V_{Cu})^{-} + h^{+} \quad \textbf{2.6}$$

$$(V_{Se} - V_{Cu})^{-} + 2h^{+} \xrightarrow{\Delta E \approx 0.35eV} (V_{Se} - V_{Cu})^{+} \quad \textbf{2.7}$$

Equation 2.6 describes the conversion from a donor to an acceptor state due to electron injection by LS and equation 2.7 the reverse reaction due to DA (relaxing). Both donor and acceptor configurations are shallow levels and can severely modify the majority charge carrier density. The theoretical predicted activation energy in equation 2.7 is experimentally well confirmed [146, 147]. A problem of the Lany-Zunger model is the high formation energy of $V_{Se}$ for copper poor materials [148], wherefore the required concentration of $V_{Se}$ is debatable. An extension of the Lany-Zunger model is proposed by Erslev et al. [149] involving the $In_{Cu}$ antisite interchanging electrons with the $V_{Se}$ vacancies. Their model is founded on the results generated by capacitance spectroscopic methods, where less formation of deep defects after LS for samples containing Na is observed [149]. In that context the role of sodium is assumed to reduce the lattice disorder caused by $In_{Cu}$ antisites and changing equally the configuration of $In_{Cu}$ to an energy level above the conduction band minimum, reducing the deep defect concentration [107, 149].

### 2.1.6. Sample preparation for the present study

After providing the background of CIGSe solar cells in the following the manufacturing and handling of samples for ALE studies is described. In this work solely CIGSe samples were investigated with Sodium incorporated from the glass substrate. The investigated solar cells and CIGSe absorber layers of this thesis were grown on a commercially available Mo laminated SLG substrate from *Guardian Thalheim GmbH*. For manufacturing CIGSe films the 3-stage co-evaporation process was applied. After preparation the final ratios of GGI ≈ 0.3 and CGI ≈ 0.85 were determined by energy dispersive X-ray spectroscopy (EDX) on a reference sample of the batch. In the case of solar cells the CBD-CdS process was conducted under a strong dimmed illumination of the laboratory to avoid further unwanted ALE of the uncoated CIGSe layers. This was additionally promoted by preserving the samples in light tight cases. In contrast to section 2.1.1 the i-ZnO and ZnO:Al window layers were fabricated by reactive sputtering at the *Fraunhofer IMWS*. Finally, the deposition of the metal grid for electrical contacting was conducted by electron beam evaporation of Ni and Al in vacuum.

## 2.2. The p-n$^-$-n-n$^+$-hetero-junction

To investigate the principles of the functionality of a CIGSe solar cell in the subsequent chapters, this section deals with the p-n$^-$-n-n$^+$-hetero-junction formed in a CIGSe solar cell with the layer arrangement depicted on the right hand side in Figure 2. The particular domains can be attributed to (1) the p-type CIGSe absorber with an effective acceptor density denoted by $N_{A,a}$. Followed by (2) the weakly doped (n$^-$) CdS buffer layer with an effective donor density of $N_{D,b}$. Thereupon forms (3) the moderate n-doped i-ZnO, the high resistive window (hrw) layer with $N_{D,hrw}$. Finally (4) the highly doped (n$^+$) AZO with $N_{D,lrw}$ donors completes the solar cell, where lrw denotes low resistive window. The index by upper case characters indicates the type of dopants (A: Acceptor, D: Donor) and lower case characters indicate the functional layer (a: absorber, b: buffer etc.) of the solar cell. The relevance of each layer is discussed in section 2.1.

In contrast to a homo-junction the semiconducting materials are differing in their electro-physical properties with main focus on the band gap energies $E_{g,i}$, the dielectric constants $\varepsilon_0\varepsilon_{r,i} = \varepsilon_i$ and the electron affinities $\chi_{e,i}$ (i = a, b, hrw, lrw). These quantities for the respective layer are given in Table A - 4 in the form of a default solar cell model for simulation and calculation of electrical device characteristics.

A requirement to generate the band diagram in the vicinity of the junction like in Figure 7 d) is the alignment of the electrostatic potential $\varphi_i$ within the space charge region (SCR) of the respective layer (i = a, b, hrw, lrw). In Figure 7 a) it is assumed that the SCR indicated by the red shading in between absorber/buffer/hr-window is formed by stationary charges due to the depletion of mobile majority charge carriers, which are diffusing into opposite (p-n) or lower (n-n$^+$) doped layers at the junctions.

Because of the small thickness $d_b$ and the low net doping concentration $N_{D,b}$ (compensating defects) of the CdS buffer layer it is highly probable that this layer is completely depleted. The latter case can be taken into account if the following inequality is fulfilled.

$$d_b < \frac{\varepsilon_b}{\varepsilon_a}\sqrt{\frac{2\varepsilon_a N_{D,b}}{q^2 N_{A,a}\left(N_{A,a}+N_{D,b}\right)}\left(\Delta E_C + E_{g,a} - k_B T ln\left[\frac{N_{C,b}N_{V,a}}{N_{D,b}N_{A,a}}\right]\right)} \qquad \textbf{2.8}$$

Inequality 2.8 can be derived by solving the static potential for the absorber/buffer junction with an infinite extended buffer layer. The right hand side of the inequality in equation 2.8 represents the depletion width ($w_b$) of the infinite extended buffer layer, forming at the junction to the absorber. $\Delta E_C = \chi_{e,a} - \chi_{e,b}$ denotes the conduction band offset between buffer

and absorber. A further boundary condition for a complete depleted buffer layer follows from the doping density of the hrw-layer and the different electron affinities of hrw-layer and buffer layer. In the case of a moderate doping of the hrw-layer and with $\chi_{e,hrw} > \chi_{e,b}$ it is highly probable that the buffer layer is depleted as well at the buffer/hr-window junction. With the physical quantities in Table A - 4 the right hand side of equation 2.8 results to $2.2d_b$, satisfying the inequality. Further is $\chi_{e,hrw} - \chi_{e,b} = 0.1$ eV, that's why the buffer layer of the default model can be considered as completely depleted. This is a useful boundary condition for solving the potential curve of the p-n$^-$-n-hero-junction, formed by the absorber, buffer, and hrw-layer. With the Schottky approximation of abrupt junctions the depletion regions can be simplified to spatial box shaped charge distributions as depicted in Figure 7 a). In equations 2.9 and 2.10 the fixed charges $\rho_i(z)$ are linked via the 1 dimensional Poisson equation to the potential $\varphi_i(z)$ and the electric field $\vec{E}_i$.

$$-\frac{d^2\varphi_a}{dz^2} = \frac{dE_{z,a}}{dz} = \frac{\rho_a(z)}{\varepsilon_a} = \frac{-qN_{A,a}}{\varepsilon_a} \quad , -w_a \le z < 0 \qquad \textbf{2.9}$$

$$-\frac{d^2\varphi_i}{dz^2} = \frac{dE_{z,i}}{dz} = \frac{\rho_i(z)}{\varepsilon_i} = \frac{qN_{D,i}}{\varepsilon_i} \quad , \begin{cases} i = b & 0 \le z < d_b \\ i = hrw & d_b \le z \le (d_b + w_{hrw}) \end{cases} \qquad \textbf{2.10}$$

The right hand side of equations 2.9 and 2.10 are valid for the depletion regions of the particular layers. Spatially, the borders of the space charge region are localized at $w_a$ within the p-doped absorber and $w_{hrw}$ within the n-doped high resistive window. Under the made assumptions the potential curve of the particular depletion regions can be derived to

$$\varphi_a(z) = \frac{qN_{A,a}}{2\varepsilon_a}(z + w_a)^2 \qquad \textbf{2.11}$$

$$\varphi_b(z) = -\frac{qN_{D,b}}{2\varepsilon_b}z^2 + \frac{qN_{A,a}}{\varepsilon_b}w_a z + \varphi_a(0) \qquad \textbf{2.12}$$

$$\varphi_{hrw}(z) = -\frac{qN_{D,hrw}}{2\varepsilon_{hrw}}(z - d_b)^2 + \frac{q\left(N_{A,a}w_a - N_{D,b}d_b\right)}{\varepsilon_{hrw}}(z - d_b) + \varphi_b(d_b)\,. \qquad \textbf{2.13}$$

Accordingly, it follows with $\varphi \propto z^2$ a quadratic dependence of the potential from the depth. The boundary conditions of equations 2.11 - 2.13 are defined by the electric field with $E_z(z = -w_a) = E_z(z = d_b + w_{hrw}) = 0$ as well as $\varepsilon_a E_z(z \to 0^-) = \varepsilon_b E_z(z \to 0^+)$ and $\varepsilon_b E_z(z \to d_b^-) = \varepsilon_{hrw} E_z(z \to d_b^+)$. Further boundary conditions are the continuity of the potentials $\varphi_a(z = 0) = \varphi_b(z = 0)$, $\varphi_b(z = d_b) = \varphi_{hrw}(z = d_b)$, which is evident from Figure 7 b) and c). A partial depletion of the high resistive window can be tested by finding the zero $z_0$ of

the negative derivation of equation 2.13 with $-d\varphi_{hrw}(z)/dz = E_{z,hrw} = 0$. If $z_0 < d_b + d_{hrw}$ the latter condition becomes true and the high resistive window can be considered as partially depleted, which holds for the model in Table A - 4. In Figure 7 c) the resulting alignment of the potential curve at thermal equilibrium (T = 300 K) is depicted for this hetero-structure, where

$$qV_{bi} = q\Delta\varphi_{SCR} = q\varphi_a(z \leq -w_a) - q\varphi_{lrw}(z \geq d_b + w_{hrw})$$
$$= E_{g,a} - k_B T ln\left[\frac{N_{C,lrw}N_{V,a}}{N_{D,lrw}N_{A,a}}\right] \quad \textbf{2.14}$$

denotes the built-in voltage. If an external voltage $V_{ext}$ is applied to the potential curve in Figure 7 c) the built in voltage $V_{bi}$ is either weakened (forward bias) or enhanced (reverse bias). Hence, the voltage dependent potential drop over the complete junction follows with $\Delta\varphi_{SCR} = V_{bi} - V_{ext}$. In consequence the depletion width $w_a$ of the absorber becomes a function of the external voltage too. By inserting equations 2.11 and 2.13 into equation 2.14 and utilizing the charge neutrality condition:

$$0 = N_{D,b}d_b + N_{D,hrw}w_{hrw} - N_{A,a}w_a \quad \textbf{2.15}$$

the depletion width $w_a$ within the absorber can be derived to:

$$w_a(V) = \delta d_b\left(\sqrt{1 + \beta + 2\vartheta\frac{\Delta\varphi_{SCR}(V)}{\varphi^*}} - 1\right). \quad \textbf{2.16}$$

For a clearer arrangement the Greek symbols in equation 2.16 are substitutions and given by

$$\delta = \frac{\varepsilon_{hrw}/\varepsilon_b - N_{D,b}/N_{D,hrw}}{\varepsilon_{hrw}/\varepsilon_a + N_{A,a}/N_{D,hrw}}$$
$$\beta = \frac{N_{D,b}}{\delta N_{A,a}}$$
$$\vartheta = \left(\frac{\varepsilon_a N_{A,a}}{\varepsilon_{hrw}N_{D,hrw}} + 1\right)^{-1} \quad \textbf{2.17}$$
$$\varphi^* = \frac{qN_{A,a}}{\varepsilon_a}\delta^2 d_b^2$$
$$\Delta\varphi_{SCR}(V) = V_{bi} - V - V_{corr} - \Delta\varphi_w$$

where $V_{corr} = k_B T/q$ is a correction term. This correction is based on the screening effect of majority carriers on the electric field at the edges of the depletion region [150].

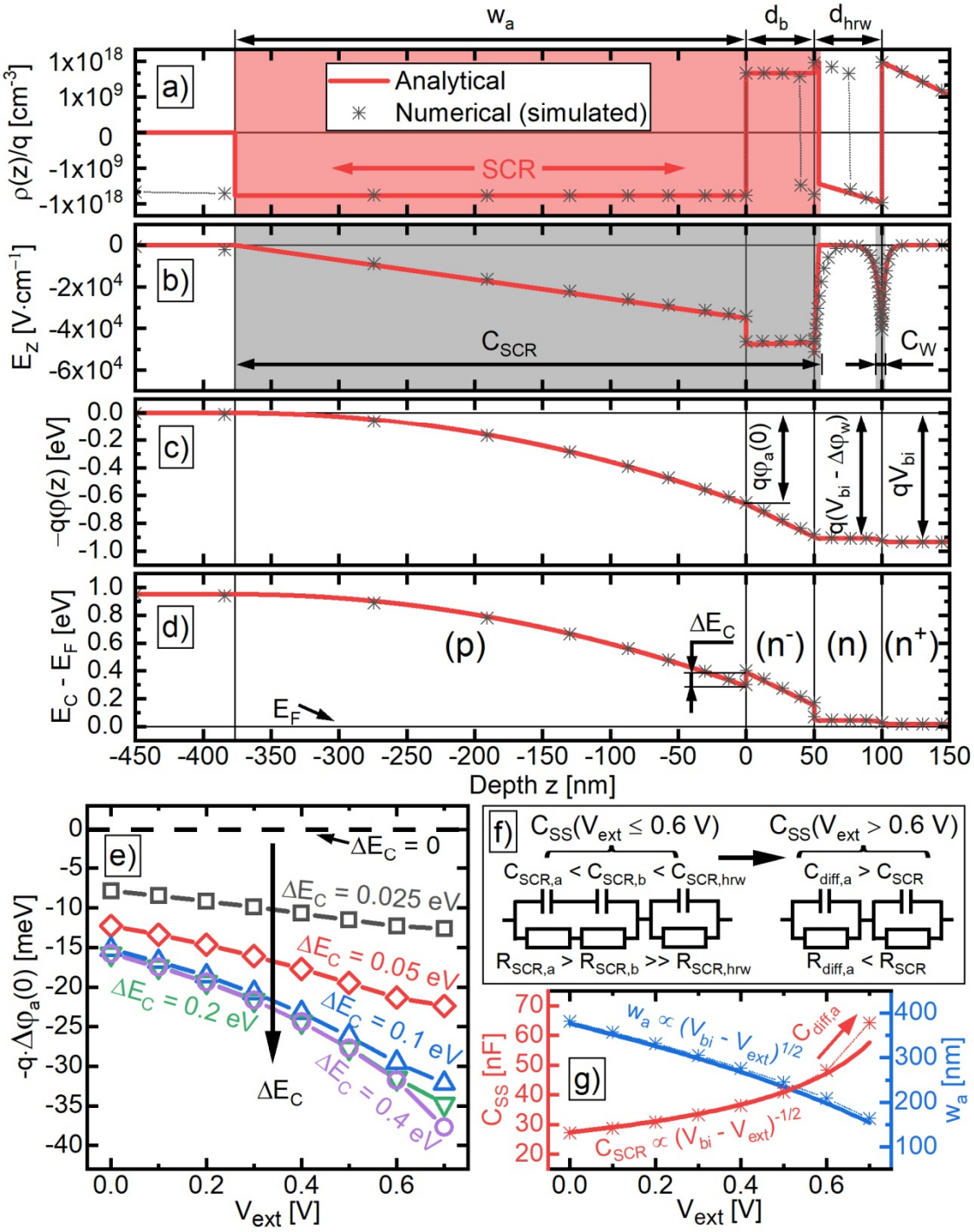


**Figure 7** Characteristics of a p-n$^-$-n-n$^+$-hetero-junction with (a) the charge distribution, where the red shading indicates the SCR with the Schottky approximation of abrupt junctions, (b) the electric field in z-direction, where the grey shadings indicate the regions for capacitance calculations. (c) depicts the induced band-bending, resulting in (d) the alignment of the conduction band. (e) shows the voltage dependent gain in band-bending $-q{\cdot}\Delta\varphi_a(0)$ at the absorber surface induced by the conduction band offset $\Delta E_C$ between absorber and buffer layer. (f) displays on the left hand side the equivalent circuit for the p-n$^-$-n-hetero-junction ($C_{SS} = C_{SCR}$) indicated by the light red and grey shading in (a), respectively (b). The equivalent circuit on the right hand side in (f) represents the case of an additional diffusion-capacitance $C_{diff,a}$ in series to the junction-capacitance $C_{SCR}$. (g) compares simulated (symbol + line) and calculated (solid line) voltage dependent curves of the complete device capacitance $C_{SS}$ in steady state ($\omega \rightarrow 0$) and the depletion width $w_a$ of the absorber. All data are obtained on the default model in Table A - 4 without interface states.

Due to the much higher doping density of the high resistive window with respect to the absorber the correction term was utilized analogous to the case of a one sided junction. When calculating potentials with $w_a$ the correction term has to be set to zero ($V_{corr} = 0$). Otherwise the potential drop $\Delta\varphi_{SCR}$ over the complete junction would be reduced by $V_{corr}$, which is physical inconceivable. Thus, $V_{corr}$ has to be regarded if the depletion width $w_a$ is the subject of interest. In the last equation of equations 2.17 $\Delta\varphi_w$ represents the potential drop between the 2 window layers as indicated in Figure 7 c). Owing to the high doping densities of the window layers $\Delta\varphi_w$ can be considered as voltage independent. The height of this potential step is

$$\Delta\varphi_w = \frac{k_B T}{q} ln\left[\frac{N_{D,lrw} N_{C,hrw}}{N_{D,hrw} N_{C,lrw}}\right]. \qquad \textbf{2.18}$$

In Figure 7 a) the electron accumulation within the hr-window and the electron depletion within the lr-window, responsible for $\Delta\varphi_w$, are decaying exponentially from $z = d_b + d_{hrw}$ in bulk-direction of the particular layer. A derivation for the analytical solutions of the hr-lr-window junction in Figure 7 a) - d) is given in Appendixes A.1.

Further, simulated data points in Figure 7 a) reveal on the buffer side an accumulation of negative charges (electrons) at the buffer/hr-window junction ($z \lesssim d_b$). This is in contradiction to the assumption of a complete depleted buffer layer. The reason for this effect is the more than 2 orders of magnitude lower effective doping density of the buffer layer with $N_{D,b} = 1 \cdot 10^{15}$ cm$^{-3}$ compared to the hr-window layer with $N_{D,hrw} = 7.1 \cdot 10^{17}$ cm$^{-3}$. Nonetheless, with respect to Figure 7 b) - d) the assumption of a complete depleted buffer layer produces only a minor difference between simulated and calculated data curves, especially at the absorber-buffer interface, which is of major interest in this work (see section 2.3.3). Figure 7 d) shows the resulting band diagram of the hetero-structure given in Table A - 4. The band alignment differs from the potential curve by a positive band offset with $\Delta E_C = 0.1$ eV between absorber and buffer layer. $\Delta E_C$ results from the reduced electron affinity with $\chi_{e,a}$-$\chi_{e,b} = 0.1$ eV assumed for the buffer layer. On the other hand, a compensating band offset with $\Delta E_C = -0.1$ eV is formed between buffer and high resistive window. Thus, the band offset does not enter into equation 2.14 for calculating $V_{bi}$. However, differences in the electron affinity effect additional bending of the bands due to accumulation of charge carriers (here electrons) at the particular side of junction with higher electron affinity. An analytical solution for a voltage dependent depletion region in combination with a band-offset is hard to achieve. Thus, in the following the phenomenology of a band offset at the absorber/buffer interface is

treaten qualitatively by means of simulated potentials at the absorber surface z = 0 in Figure 7 e). It can be confirmed in Figure 7 e) that the positive band-offset induces an additional voltage dependent downward band-bending $-q\Delta\varphi_a(0)$ at the absorber surface. The change in band-bending is referenced to no band offset with $\Delta E_C = 0$ and estimated with $-q\cdot\Delta\varphi_a(0) = -q\left[\varphi_a^{\Delta E_C}(0) - \varphi_a^{\Delta E_C = 0}(0)\right]$. In Figure 7 e) at equilibrium $-q\cdot\Delta\varphi_a(0)$ levels off for $\Delta E_C \geq 0.1$ eV. However, with increasing bias-voltage $V_{ext}$ in forward direction the impact of $\Delta E_C$ rises on $-q\cdot\Delta\varphi_a(0)$ due to an enhanced accumulation of electrons at the absorber surface. This is relevant for voltage dependent recombination rates over interface states, depending strongly on the respective charge carrier densities at the interface. Hence, this subject is picked up again in section 2.3.3.

*Capacitances of the space charge regions*

The grey shadings in Figure 7 b) indicate the analogon of the space charge regions to 2 parallel plate capacitors, where holds $E_z \neq 0$ for the electric field in between the two plates and $E_z = 0$ outside of the plates. In line with this, one plate is placed at $z = -w_a$ and the other plate at $z = d_b + w_{hrw}$ indicated by $C_{SCR}$ in Figure 7 b). Due to 3 different dielectric materials defining the junction-capacitance $C_{SCR}$ it is reasonable to divide $C_{SCR}$ further into a series connection of capacitances with homogeneous dielectric properties. The corresponding equivalent circuit for low forward bias-voltages follows on the left hand side of Figure 7 f) and is subsequently explained in this section. With the general approach for the capacitance

$$C = \varepsilon_0 \varepsilon_r \frac{\oiint \vec{E}\, d\vec{A}}{\int \vec{E}\, d\vec{s}} \qquad \textbf{2.19}$$

the respective area normalized capacitance $C_{SCR,i}$ (i = a, b, hrw) of each depletion region can be derived to

$$C_{SCR,a} = \frac{\varepsilon_a}{w_a} \;,\; C_{SCR,b} = \frac{\varepsilon_b}{d_b} \;,\; C_{SCR,hrw} = \frac{\varepsilon_{hrw}}{w_{hrw}}. \qquad \textbf{2.20}$$

The total capacitance $C_{SCR}$ follows from the steady state ($\omega = 0$, with $\omega$ the angular frequency of the applied voltage signal) solution of the equivalent circuit depicted on the left hand side in Figure 7 f). By using the complex admittance Y the total capacitance of the equivalent circuit correspond to $C_{SCR} = \mathrm{Im}(Y)/\omega$. For 2 separate parallel circuits connected in series (see section 3.2) the limit of $\mathrm{Im}(Y)/\omega$ for $\omega \rightarrow 0$ yields the capacitance in steady state. Consequently, the following equation can be derived for $C_{SCR}$

$$C_{SCR} = \frac{\left(C_{SCR,a}^{-1} + C_{SCR,b}^{-1}\right)^{-1}\left(R_{SCR,a} + R_{SCR,b}\right)^2 + C_{SCR,hrw}R_{SCR,hrw}^2}{\left(R_{SCR,a} + R_{SCR,b} + R_{SCR,hrw}\right)^2}$$

$$C_{SCR} \cong \left(\frac{1}{C_{SCR,a}} + \frac{1}{C_{SCR,b}}\right)^{-1}. \qquad \textbf{2.21}$$

In equation 2.21, the resistances $R_{SCR,i}$ (i = a, b, hrw) become available by integrating the inverse of the conductivity $\sigma(z) = \left|q\mu_n n(z)\right|$ over the particular depletion region (see equation 2.25). The reason that the conductivity within the SCR is entirely based on electrons follows from the band-diagram in Figure 8 on page 32. Due to the high valence band offset of $\gtrsim 1$ eV in between the absorber and buffer layer a charge balancing via holes between the depletion edge of the absorber ($z = -w_a$) and the depletion edge of the buffer ($z = d_b$) can be excluded. This explains, why $C_{SCR,a}$ and $C_{SCR,b}$ as well as $R_{SCR,a}$ and $R_{SCR,b}$ are connected in series in 2 separate lines connected in parallel, yielding the equivalent circuit ($V_{ext} \lesssim 0.6$ V) depicted on the left hand side of Figure 7 f). For the conduction band alignment in Figure 7 d) the resistances in equilibrium follow from numerical integration to $R_{SCR,a} \approx 6 \cdot 10^{10}$ Ω·cm$^2$, $R_{SCR,b} \approx 0.15$ Ω·cm$^2$, and $R_{SCR,hrw} \approx 2 \cdot 10^{-7}$ Ω·cm$^2$. In accordance with equation 2.21 this 17 orders of magnitude lower resistance of the hr-window effects a negligible contribution of $C_{SCR,hrw}$ to $C_{SCR}$. Inserting equations 2.16 and 2.20 into equation 2.21 the junction-capacitance can be expressed as a function of voltage by

$$C_{SCR}(V) = \frac{\varepsilon_a \varepsilon_b}{\varepsilon_b w_a(V) + \varepsilon_a d_b} = \left[\frac{d_b}{\varepsilon_b} + \frac{\delta d_b}{\varepsilon_a}\left(\sqrt{1 + \beta + 2\vartheta\frac{\Delta\varphi_{SCR}(V)}{\varphi^*}} - 1\right)\right]^{-1}. \qquad \textbf{2.22}$$

From equation 2.22 it can be concluded that $C_{SCR}$ depends solely on the inverse depletion width $w_a$ of the absorber and hence on the inverse square root of $V_{bi}$ - V as labelled in Figure 7 g). Due to the highest resistance with $R_{SCR} \approx 10^{11}$ Ω·cm$^2$ of the absorber/buffer junction within the complete device it can be concluded that the device capacitance in steady state $C_{SS}$ equals to $C_{SCR}$ as shown in Figure 7 g) for $V_{ext} \lesssim 0.6$ V.

Further, with the previous consideration it will be attempted to demonstrate that the contribution of the window-junction capacitance $C_W$ to the complete device capacitance $C_{SS}$ becomes negligible. In Figure 7 b) $C_W$, indicated by the grey shading, is located in between the z-coordinates of the 1/e$^2$-decay of the electric field $E_z$. These borders are derived with equation 2.19. Both, the depletion width within the lr-window as well as the accumulation width within the hr-window are corresponding to 2 times the Debye-length $\lambda_D$ given in equation 2.23.

$$\lambda_{D,i} = \sqrt{\frac{\varepsilon_i k_B T}{q^2 N_{D,i}}} \quad , \quad i = hrw, lrw \qquad \textbf{2.23}$$

In accordance with equation 2.20, the capacitances of the 2 regions can be estimated with $C_{W,i} = \varepsilon_i/2\lambda_i$ (i = hrw, lrw). Because of the high availability of electrons within the window junction the equivalent circuit of this junction can be expected as 2 separate parallel circuits $R_{W,hrw} \parallel C_{W,hrw}$ and $R_{W,lrw} \parallel C_{W,lrw}$ connected in series. The capacitance $C_W$ of this series connection can be derived with equation 2.24 and $C_W$ can be expected as independent from the external voltage.

$$C_W = \frac{C_{W,hrw}R_{W,hrw}^2 + C_{W,lrw}R_{W,lrw}^2}{\left(R_{W,hrw} + R_{W,lrw}\right)^2} \qquad \textbf{2.24}$$

However, due to $R_{W,hrw} \approx R_{W,lrw}$ the capacitance $C_W$ will not reduce to $C_{W,hrw}$ or $C_{W,lrw}$ as in the case of $C_{SCR} \cong \left(C_{SCR,a}^{-1}+C_{SCR,b}^{-1}\right)^{-1}$ in equation 2.21. Thus, the resistances $R_{W,hrw}$ , $R_{W,lrw}$ have to be determined by integrating the inverse conductance $1/\sigma(z)$ over the particular region of the junction. As shown in equation 2.25 this equals to an integration of the inverse electron density 1/n(z) under the assumption that the contribution of holes to the conductance is negligible for the window layers.

$$R_{W,i} = \pm \int_{\mp 2\lambda_{D,i}}^{0} \frac{1}{\sigma_i(z^*)} dz^* = \pm \int_{\mp 2\lambda_{D,i}}^{0} \frac{1}{\left|q\mu_{n,i}n_i(z^*)\right|} dz^* \quad , \quad i = hrw, lrw \qquad \textbf{2.25}$$

To simplify the integration procedure in equation 2.25 the z-coordinate is substituted by $z^* = z - d_b - d_{hrw}$. In spite of this, the analytical integration of 1/n(z) is hard to achieve because of $n(z) \propto \exp\{q\varphi(z)/k_BT\}$ and $\varphi(z) \propto \exp\{z/\lambda_D\}$. That's why, from numerical integrations the resistances have been estimated to $R_{W,hrw} \approx 3 \cdot 10^{-7}$ Ω·cm² and $R_{W,lrw} \approx 1 \cdot 10^{-7}$ Ω·cm². With the particular capacitances $C_{W,hrw} \approx 1.9$ µF·cm$^{-2}$ and $C_{W,lrw} \approx 3.1$ µF·cm$^{-2}$ the complete capacitance of the window-junction can be determined to $C_W \approx 1.3$ µF·cm$^{-2}$. By utilizing again the complex admittance (see section 3.2) the resistance for $\omega \rightarrow 0$ of the complete window-junction follows with $R_W = R_{W,hrw} + R_{W,lrw} = 4 \cdot 10^{-7}$ Ω·cm². Repetitively, due to the series connection of $R_{SCR} \parallel C_{SCR}$ and $R_W \parallel C_W$ the complete device capacitance $C_{SS}$ becomes available with equation 2.24 by replacing the respective resistances and capacitances. Independent from the external voltage it follows that $R_{SCR} >> R_W$ and hence $C_{SS} \cong C_{SCR}$.

On the other hand, if the external voltage exceeds 0.6 V the simulated device capacitance $C_{SS}$ (symbol + scattered line) in Figure 7 g) begins to deviate from the analytical solution $C_{SCR}$

(solid line) calculated with equation 2.22. Responsible for this increased capacitance is the diffusion capacitance $C_{diff,a}$ caused by injection of minority charge carriers into the absorber bulk. A closer examination of $C_{diff,a}$ is given in the next section 2.2.1.

### 2.2.1. Ideal diode current

A solar cell situated at its working point is subjected to physical processes comparable to a diode biased with a respective external voltage. Usually, the voltage of the working point is in proximity to the open circuit voltage $V_{OC}$. Under $V_{OC}$-condition the diode-current balances the generated photo-current. For this purpose, the present section derives with the ideal diode current in forward direction an expression for $V_{OC}$ of an ideal solar cell.

The band diagram and charge carrier densities of a solar cell in steady state biased with $V_{ext}$ = 0.7 V in forward direction are depicted in Figure 8 (a) and (b). Approximately, the difference $E_{Fn} - E_{Fp} = q \cdot V_{ext}$ of the quasi-Fermi levels is constant within the SCR ($E_z < 0$ V/cm). Inside of the quasi-neutral regions ($E_z \approx 0$ V/cm) $QNR_a$ and $QNR_{hrw}$ the recombination of injected minority charge carriers is characterized by decreasing minority charge carrier densities with increasing distance to the SCR edge. This causes a gradient of the respective quasi-Fermi level $E_{Fn,a}$ and $E_{Fp,hrw}$ within $QNR_a$ and $QNR_{hrw}$. The strength of the gradient represents the rate of recombination and is accordingly a characteristic factor of the diode current. In Figure 8 a) it is apparent that $\nabla E_{Fn,a} << \nabla E_{Fp,hrw}$. As a result, the minority charge carriers within the absorber have to be regarded for the derivation of the diode current.

In Figure 8 b) a more than 2 orders of magnitude lower minority charge carrier density with respect to the majority charge carrier density at the SCR edge ($z = -w_a$) indicates the case of low injection (l.i.). Thus, the quasi-Fermi level $E_{Fp,a}$ for holes remains constant inside of $QNR_a$. By using the Schottky approximation the existing injection of electrons at $z = -w_a$ becomes comparable to the absorption case of light with high photon energies i.e. $E_{ph} \approx 3 \cdot E_{g,a}$. In that case the depth dependent generation rate $G_{n,a}$ becomes spatially narrow and negligible within the QNR. This reduces the continuity equation for injected excess-electrons $\Delta n_a(z)$ inside of $QNR_a$ to

$$\frac{\Delta n_a(z)}{\tau_{n,a}} = D_{n,a} \frac{d^2 \Delta n_a(z)}{dz^2} \qquad \textbf{2.26}$$

with $D_{n,a}$ the diffusion coefficient and $\tau_{n,a}$ the lifetime of electrons within the absorber.

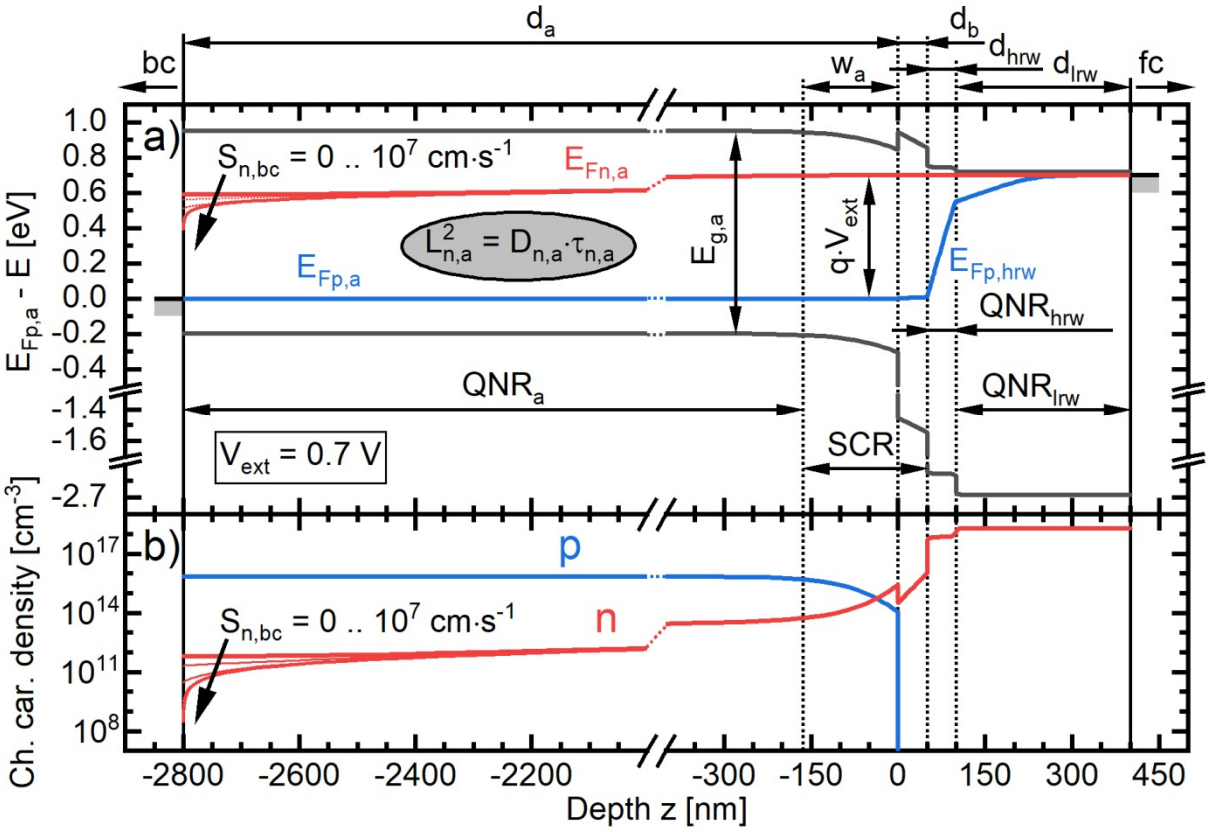


**Figure 8** (a) Band diagram of a theoretical solar cell under an applied bias-voltage of $V_{ext}$ = 0.7 eV in darkness. The physical parameters of the used solar cell model are given in Table A - 4. Recombination centres at the absorber/buffer interface are not included in the simulation of this band diagram. For a simplified illustration of the particular regions in the solar cell the spatial extension of space charge and charge accumulation layers within the window layers are neglected. (b) Spatial distributions of the electron and hole densities within the particular regions of the solar cell.

The electron density at the depletion edge z = –$w_a$ can be determined with the quasi-Fermi levels, giving following equation.

$$\Delta n_a(-w_a(V)) = \frac{n_{i,a}^2}{N_{A,a}}\left(exp\left\{\frac{E_{Fn,a}-E_{Fp,a}}{k_BT}\right\}-1\right) \overset{l.i.}{\approx} n_{a,0}\left(exp\left\{\frac{qV}{k_BT}\right\}-1\right) \qquad \textbf{2.27}$$

Using the result of equation 2.27 and $d\Delta n_a/dz|_{-d_a} = 0$ as boundary conditions the solution of equation 2.26 is given with

$$\Delta n_a(z,V) = n_{a,0}\left(exp\left\{\frac{qV}{k_BT}\right\}-1\right)\frac{\cosh\left(\frac{z+d_a}{L_{n,a}}\right)}{\cosh\left(\frac{d_a-w_a(V)}{L_{n,a}}\right)}, \qquad z \le -w_a(V) \qquad \textbf{2.28}$$

where $L_{n,a} = (D_{n,a}\cdot\tau_{n,a})^{1/2}$ denotes the diffusion length of electrons. Equation 2.28 gives the ability to obtain the depth and voltage dependent recombination rate $R_{n,a}(z,V) = \Delta n_a(z,V)/\tau_{n,a}$ of electrons within $QNR_{,a}$. For a finite absorber thickness the electron current

$J_{n,a}$ becomes available in equation 2.29 by integrating $q \cdot R_{n,a}(z,V)$ over the complete QNR of the absorber.

$$J_{n,a}(V) = q \int_{-d_a}^{-w_a(V)} R_{n,a}(z,V)\, dz = \frac{qL_{n,a}n_{a,0}}{\tau_{n,a}} \left( exp\left\{\frac{qV}{k_B T}\right\} - 1 \right) \tanh\left( \frac{d_a - w_a(V)}{L_{n,a}} \right) \qquad \textbf{2.29}$$

The Shockley-equation for ideal diodes can be derived by combining the pre-factors on the right hand side of equations 2.29 to the saturation current density $J_0$.

$$J_{diode}(V) = J_{n,a}(V) = J_0 \left( exp\left\{\frac{qV}{k_B T}\right\} - 1 \right) \qquad \textbf{2.30}$$

$$J_0(V) = \frac{qL_{n,a}n_{a,0}}{\tau_{n,a}} \tanh\left( \frac{d_a - w_a(V)}{L_{n,a}} \right) \approx \frac{qL_{n,a}n_{a,0}}{\tau_{n,a}} \quad for \quad d_a \gg w_a(V)\,, L_{n,a} \qquad \textbf{2.31}$$

The used model in Figure 8 has an absorber thickness of $d_a$ = 2.8 µm, the diffusion length is $L_{n,a} \approx$ 500 nm and the depletion width within the absorber is $w_a$(0 V) ≈ 380 nm. With these values the argument of the hyperbolic tangent in equation 2.31 becomes > 3, where the tanh-function converges to 1. That means, in the case case of $d_a - w_a(V) \gtrsim 3L_{n,a}$ the narrowing on the right hand side of equation 2.31 is valid. This holds always for the default model, if the external voltage is applied in forward direction (≥ 0 V), then $J_0(V) \rightarrow J_0$ becomes independent of the external voltage. By replacing $n_{a,0}$ with $n_{i,a}^2/N_{A,a}$ and $L_{n,a}$ with $(D_{n,a} \cdot \tau_{n,a})^{1/2}$ the saturation current density can be rewritten to:

$$J_0 \approx \frac{qn_{i,a}^2}{N_{A,a}} \sqrt{\frac{D_{n,a}}{\tau_{n,a}}} = \frac{qN_{C,a}N_{V,a}}{N_{A,a}} \sqrt{\frac{D_{n,a}}{\tau_{n,a}}}\, exp\left\{-\frac{E_{g,a}}{k_B T}\right\}. \qquad \textbf{2.32}$$

It is evident from equation 2.32 that an Arrhenius plot of $J_0$ over $T^{-1}$ delivers an activation energy of $E_A = E_{g,a}$ for the saturation current density. Thus, introducing the reference current density $J_{00}$ [50] equation 2.32 can be recomposed to

$$J_0 = J_{00} exp\left\{-\frac{E_A}{k_B T}\right\}. \qquad \textbf{2.33}$$

*Back contact recombination current*

In the former part of this section it could be shown that the finite absorber fulfilling $d_a - w_a(V) \gtrsim 3L_{n,a}$ gives a negligible modification of the diode current compared with an infinite

extended absorber. Hereafter, the impact of the electron back-contact recombination on the diode current is demonstrated. The recombination current density

$$J_{n,bc}(V) = qS_{n,bc}\Delta n_a(-d_a,V) = qD_{n,a}\frac{d\Delta n_a(-d_a,V)}{dz} \qquad \textbf{2.34}$$

of electrons at the back contact depends on the recombination velocity $S_{n,bc}$ and the present excess charge carrier density $\Delta n_a(-d_a,V)$. The right hand side of equation 2.34 represents the diffusion current out of the back side of the absorber. Transforming equation 2.34 to $d\Delta n_a/dz|_{-d_a,V} = \left(S_{n,bc}/D_{n,a}\right)\cdot\Delta n_a(-d_a,V)$ gives the back contact boundary condition for solving the continuity equation in 2.26. With the second boundary condition for the injected electron density $\Delta n_a(-w_a(V))$ in equation 2.27 the depth and voltage dependent electron density within $QNR_a$ $\left(z \leq -w_a(V)\right)$ results to

$$\Delta n_a(z,V) = \frac{n_{a,0}\left(exp\left\{\frac{qV}{k_BT}\right\}-1\right)\left[\cosh\left(\frac{z+d_a}{L_{n,a}}\right)+\frac{L_{n,a}S_{n,bc}}{D_{n,a}}\sinh\left(\frac{z+d_a}{L_{n,a}}\right)\right]}{\cosh\left(\frac{d_a-w_a(V)}{L_{n,a}}\right)+\frac{L_{n,a}S_{n,bc}}{D_{n,a}}\sinh\left(\frac{d_a-w_a(V)}{L_{n,a}}\right)}. \qquad \textbf{2.35}$$

Obviously, in the case of $S_{n,bc} = 0$ the solution of $\Delta n_a(z,V)$ in equation 2.35 reduces to the solution without back-contact recombination in equation 2.28. The contribution of the additional hyperbolic sine terms with pre-factors on $\Delta n_a(z,V)$ is observable in Figure 8 b). Accordingly, up to a depth of ¾ of the absorber thickness ($z \approx -d_a + L_{n,a}$) $\Delta n_a(z,V)$ reveals no dependency to the back-contact recombination velocity. In a closer distance to the back-contact the hyperbolic sine function of the numerator in equation 2.35 converges to 0 and does not balance the additional contribution of the sinh-function in the denominator anymore. Thus, in conformity with Figure 8 b) an increasing recombination velocity $S_{n,bc}$ causes a decreasing electron density $\Delta n_a(-d_a,V)$ in the vicinity of the back-contact.

As mentioned above at $z = -d_a$ the sinh-function in the numerator of equation 2.35 converges to 0. On the other hand the cosh-function converges to 1 at $z = -d_a$. Consequently, the back-contact recombination current density can be deduced from equations 2.34 and 2.35 to

$$J_{n,bc}\left(V,S_{n,bc}\right) = \frac{qS_{n,bc}n_{a,0}\left(exp\left\{\frac{qV}{k_BT}\right\}-1\right)}{\cosh\left(\frac{d_a-w_a(V)}{L_{n,a}}\right)+\frac{L_{n,a}S_{n,bc}}{D_{n,a}}\sinh\left(\frac{d_a-w_a(V)}{L_{n,a}}\right)}. \qquad \textbf{2.36}$$

The diode current density $J_{diode}(V)$ can be obtained by the superposition principle of the back-

contact recombination and bulk recombination current density with $\left(J_{n,bc}+J_{n,a}\right)\big|_{V,S_{n,bc}}$ in equation 2.37.

$$J_{diode}(V,S_{n,bc}) = J_{n,a}(V,S_{n,bc}) + J_{n,bc}(V,S_{n,bc}) = J_0\left(exp\left\{\frac{qV}{k_BT}\right\}-1\right)\cdot\Xi(V,S_{n,bc}) \qquad \textbf{2.37}$$

$$\Xi(V,S_{n,bc}) = \frac{\sinh\left(\frac{d_a-w_a(V)}{L_{n,a}}\right)+\frac{L_{n,a}S_{n,bc}}{D_{n,a}}\cosh\left(\frac{d_a-w_a(V)}{L_{n,a}}\right)}{\cosh\left(\frac{d_a-w_a(V)}{L_{n,a}}\right)+\frac{L_{n,a}S_{n,bc}}{D_{n,a}}\sinh\left(\frac{d_a-w_a(V)}{L_{n,a}}\right)} \qquad \textbf{2.38}$$

Integration of equation 2.35 over $QNR_a$ delivers $J_{n,a}$ in equation 2.37. After few transformations the right hand side of equation 2.37 becomes available, where $J_0$ corresponds to the approximated solution in equation 2.32 of an infinite absorber. The function $\Xi\left(V,S_{n,bc}\right)$ given in equation 2.38 includes the modifications caused by a finite absorber and the electron recombination at the back-contact. For $d_a$ = 2.8 µm, $L_{n,a}$ = 500 nm and $\tau_{n,a}$ = 10 ns this function results to ≈ 1, independent from the external voltage $V_{ext} \geq 0$ V and the back-contact recombination velocity $S_{n,bc} \leq 10^7$ cm/s. In consequence the diode current density of solar cells with identical physical quantities as given in Table A - 4 can be considered as immune to recombination at the back-contact.

*Open circuit voltage*

After investigating the diode current density in darkness, the diode current densities within the hetero-structure under illumination becomes the subject of interest. In this case the continuity equation in 2.26 for electrons $\Delta n_a(z)$ within the QNR of the absorber has to be supplemented by the generation rate $G_{n,a}(z)$ of excess charge carriers. For monochromatic illumination with a generation rate $G_{n,a}(z) = G_{n,a}(0)\exp\{\alpha\cdot z\}$ the continuity equation for electrons $\Delta n_a$ and its solution can be given with the following 2 equations.

$$0 = G_{n,a}(z) - \frac{\Delta n_a(z)}{\tau_{n,a}} + D_{n,a}\frac{d^2\Delta n_a(z)}{dz^2}, \quad z \leq -w_a \qquad \textbf{2.39}$$

$$\Delta n_a(z) = \frac{\tau_{n,a}\left(G_{n,a}(z) - G_{n,a}(-w_a-L_{n,a})\cdot \mathrm{H}(z,S_{n,bc}) - G_{n,a}(-d_a)\cdot\Lambda(z,S_{n,bc})\right)}{\left(1-\alpha^2L_{n,a}^2\right)} \qquad \textbf{2.40}$$

In equations 2.39 and 2.40 it was assumed that $\tau_{n,a}$ is no function of the incident light intensity or applied voltage (weak excitation or injection). The solution in equation 2.40 has been derived by using the boundary conditions $d\Delta n_a/dz|_{-d_a} = \left(S_{n,bc}/D_{n,a}\right)\cdot\Delta n_a(-d_a)$ for the back

contact and $d\Delta n_a/dz|_{-w_a\text{-}L_{n,a}} = 0$ in the case of $L_{n,a} < d_a$ [151]. To achieve an improved clarity in equation 2.40 the dimensionless functions $H(z,S_{n,bc})$ and $\Lambda(z,S_{n,bc})$ have been introduced representatively for

$$H(z,S_{n,bc}) = \alpha \frac{L_{n,a}D_{n,a}\cosh\left(\frac{d_a+z}{L_{n,a}}\right) + L_{n,a}^2 S_{n,bc}\sinh\left(\frac{d_a+z}{L_{n,a}}\right)}{L_{n,a}S_{n,bc}\cosh\left(\frac{w_a+L_{n,a}-d_a}{L_{n,a}}\right) - D_{n,a}\sinh\left(\frac{w_a+L_{n,a}-d_a}{L_{n,a}}\right)}$$

$$\Lambda(z,S_{n,bc}) = \frac{L_{n,a}(S_{n,bc}-\alpha D_{n,a})\cosh\left(\frac{L_{n,a}+w_a+z}{L_{n,a}}\right)}{L_{n,a}S_{n,bc}\cosh\left(\frac{w_a+L_{n,a}-d_a}{L_{n,a}}\right) - D_{n,a}\sinh\left(\frac{w_a+L_{n,a}-d_a}{L_{n,a}}\right)}. \quad \textbf{2.41}$$

The contribution $J_{n,QNRa}$ to the photo-current density $J_{ph}(V)$ due to generated electrons within $QNR_a$ becomes available with $\Delta n_a$ in equation 2.40.

$$J_{n,QNRa}(V) = -q\int_{-d_a}^{-w_a(V)} G_{n,a}(z) - \frac{\Delta n_a(z)}{\tau_{n,a}}dz$$

$$= -q\frac{\alpha^2 L_{n,a}^2\left(G_{n,a}(-d_a) - G_{n,a}(z)\right) + G_{n,a}(z-L_{n,a})\cdot H_0(z,S_{n,bc}) - G_{n,a}(-d_a)\cdot\Lambda_0(z,S_{n,bc})}{\alpha(1-\alpha^2 L_{n,a}^2)}\Bigg|_{z=-w_a(V)} \quad \textbf{2.42}$$

$H_0(\text{-}w_a(V),S_{n,bc}) \rightarrow H_0(V,S_{n,bc})$ and $\Lambda_0(V,S_{n,bc})$ are the integrated functions of equations 2.41 extended with α to keep these functions dimensionless.

$$H_0(V,S_{n,bc}) = \frac{\alpha^2 L_{n,a}^2 D_{n,a}\sinh\left(\frac{d_a-w_a(V)}{L_{n,a}}\right) + \alpha^2 L_{n,a}^3 S_{n,bc}\left(\cosh\left(\frac{d_a-w_a(V)}{L_{n,a}}\right)-1\right)}{L_{n,a}S_{n,bc}\cosh\left(\frac{w_a(V)+L_{n,a}-d_a}{L_{n,a}}\right) - D_{n,a}\sinh\left(\frac{w_a(V)+L_{n,a}-d_a}{L_{n,a}}\right)}$$

$$\Lambda_0(V,S_{n,bc}) = \frac{\alpha L_{n,a}^2(S_{n,bc}-\alpha D_{n,a})\left(\sinh(1)-\sinh\left(\frac{L_{n,a}+w_a(V)-d_a}{L_{n,a}}\right)\right)}{L_{n,a}S_{n,bc}\cosh\left(\frac{L_{n,a}+w_a(V)-d_a}{L_{n,a}}\right) - D_{n,a}\sinh\left(\frac{L_{n,a}+w_a(V)-d_a}{L_{n,a}}\right)} \quad \textbf{2.43}$$

By neglecting diffusion and recombination within the SCR the current density $J_{n,SCRa}$ due to light generation within $SCR_a$ can be considered as constant. Integrating the generation rate from $z = -w_a(V)$ to $z = 0$ the contribution of the depletion region $SCR_a$ within the absorber to the photo-current density results to

$$J_{n,SCRa}(V) = -q\frac{G_{n,a}(0) - G_{n,a}\left(w_a(V)\right)}{\alpha}. \qquad \textbf{2.44}$$

Totalling equations 2.42 and 2.44 gives the collected photo-current density within the absorber. If the photon energy of the incident light is smaller than the band gap energy of the CdS buffer layer the light induced photo-current density of the absorber corresponds to $J_{ph}(V)$ of the complete solar cell. The diode current density $J_{diode}$ of the ideal solar cell under illumination is accordingly determined by the sum of equations 2.30, 2.42, and 2.44.

$$J_{diode}(V) \approx J_0\left(exp\left\{\frac{qV}{k_BT}\right\} - 1\right) - J_{ph}(V) \qquad \textbf{2.45}$$

The open circuit voltage $V_{OC}$ for the illuminated p-$n^-$-n-$n^+$-device can be obtained by setting the diode current density in equation 2.45 equal to zero. Assuming $J_{ph} >> J_0$ conduces to an implicit equation for the temperature dependence of the open circuit voltage.

$$V_{OC}(T) \approx \frac{k_BT}{q} ln\left(\frac{J_{ph}(V_{OC})}{J_0}\right) = \frac{E_A}{q} - \frac{k_BT}{q} ln\left(\frac{J_{00}}{J_{ph}(V_{OC})}\right) \qquad \textbf{2.46}$$

Thus, the activation energy of the saturation current density for an ideal solar cell can be obtained by measuring $V_{OC}$ as a function of temperature and extrapolating to T = 0 K (compare section 3.1.1).

*Diffusion-capacitance*

As shown in Figure 7 g), for bias-voltages exceeding 0.6 V an additional capacitance contribution $C_{diff,a}$ to the junction capacitance $C_{SCR}$ emerges. The reason for this additional capacitance is the injection of electrons from the SCR into the $QNR_a$ of the absorber giving additional negative charges within $QNR_a$. Figure 8 b) depicts the depth dependent electron and hole concentration under an applied forward bias of $V_{ext}$ = 0.7 V. Within $QNR_a$ the hole concentration can be considered as constant, whereas the electron concentration decreases towards the back contact. Following equation 2.19 this produces a capacitance indicated by $C_{diff,a}$. This diffusion capacitance can be derived from the oscillating excess electron density $\Delta n_a(z,V(t))$ within $QNR_a$. The external voltage V(t) can be expressed with

$$V(t) = V_{DC} + \hat{V}_{AC}exp\{i\omega t\} \qquad \textbf{2.47}$$

where $V_{DC}$ represents the direct voltage and $\hat{V}_{AC}$ the amplitude of the small test signal. Under the assumption that $\hat{V}_{AC} << V_{DC}$ the time dependent thickness variation of $QNR_a$ becomes

negligible and it can be approximated $d_a - w_a(V(t)) \approx d_a - w_a(V_{DC})$. By courtesy of the previous assumption and by inserting equation 2.47 into 2.35 the time dependent excess electron density can be revealed to

$$\Delta n_a(z, V(t)) \approx n_{a,0}\Theta(z, V_{DC}, S_{n,bc}) exp\left\{\frac{q(V_{DC} + \hat{V}_{AC} exp\{i\omega t\})}{k_B T}\right\}. \quad \textbf{2.48}$$

In equation 2.48 the function $\Theta(z,V_{DC},S_{n,bc})$ includes the hyperbolic functions of equation 2.35. Further, the -1 in equation 2.35 is neglected in equation 2.48 due to high forward voltages (compare Figure 7) giving $qV_{DC} >> k_BT$ and $exp\{q(V_{DC}+\hat{V}_{AC}exp\{i\omega t\})/k_BT\} >> 1$. For a small test signal equation 2.48 can be approximated with

$$\Delta n_a(z, V(t)) \approx n_{a,0}\Theta(z, V_{DC}, S_{n,bc}) exp\left\{\frac{qV_{DC}}{k_B T}\right\}\left(1 + \frac{q\hat{V}_{AC} exp\{i\omega t\}}{k_B T}\right). \quad \textbf{2.49}$$

From equation 2.49 it is visible that the complete time dependent excess electron density is the summation of the steady state solution in equation 2.35 and a time dependent excess electron density $\Delta\tilde{n}_a(t)$ due to the small test signal. In that case after Ref. [150] the time dependent excess electron density in equation 2.49 can be rewritten to

$$\Delta n_a(z, V(t)) = \Delta n_a(z, V_{DC}) + \Delta\tilde{n}_a(z, V_{DC}, t). \quad \textbf{2.50}$$

Before, obtaining the ac current density $\tilde{J}$ caused by the small test signal the time dependent continuity equation for $\Delta\tilde{n}_a(z,V_{DC},t)$ in equation 2.51 has to be solved.

$$\frac{\partial}{\partial t}\Delta\tilde{n}_a = D_{n,a}\frac{\partial^2 \Delta\tilde{n}_a}{\partial z^2} - \frac{\Delta\tilde{n}_a}{\tau_{n,a}} \quad \textbf{2.51}$$

With the boundary conditions

$$\Delta\tilde{n}_a(-w_a, V_{DC}, t) = n_{a,0} exp\left\{\frac{qV_{DC}}{k_B T}\right\}\frac{q\hat{V}_{AC}}{k_B T} exp\{i\omega t\}$$
$$\frac{\partial}{\partial z}\Delta\tilde{n}_a\Big|_{-d_a, V_{DC}} = \frac{S_{n,bc}}{D_{n,a}}\Delta\tilde{n}_a(-d_a, V_{DC}, t) \quad \textbf{2.52}$$

as well as $\partial\Delta\tilde{n}_a/\partial t = i\omega\cdot\Delta\tilde{n}_a$ and $\tau^*_{n,a} = \tau_{n,a}/(1+i\omega\tau_{n,a})$ [150] the solution for $\Delta\tilde{n}_a(z,V_{DC},t)$ results to

$$\Delta\tilde{n}_a(z,V_{DC},t) = n_{a,0}exp\left\{\frac{qV_{DC}}{k_BT}\right\}\frac{q\hat{V}_{AC}}{k_BT}exp\{i\omega t\}\cdot\Theta^*\left(z,V_{DC},S_{n,bc}\right)$$

$$\Theta^*\left(z,V_{DC},S_{n,bc}\right) = \frac{\cosh\left(\frac{z+d_a}{L^*_{n,a}}\right)+\frac{L^*_{n,a}S_{n,bc}}{D_{n,a}}\sinh\left(\frac{z+d_a}{L^*_{n,a}}\right)}{\cosh\left(\frac{d_a-w_a(V_{DC})}{L^*_{n,a}}\right)+\frac{L^*_{n,a}S_{n,bc}}{D_{n,a}}\sinh\left(\frac{d_a-w_a(V_{DC})}{L^*_{n,a}}\right)} \quad \textbf{2.53}$$

where $L^*_{n,a} = \sqrt{D_{n,a}\tau^*_{n,a}} = L_{n,a}\left(1+i\omega\tau_{n,a}\right)^{-1/2}$ is the complex diffusion length. Equation 2.54 gives the solution of the ac component $\tilde{J}$ of the complete current density, derived by integrating $q\cdot\Delta\tilde{n}_a/\tau_{n,a}$ over $QNR_a$ plus the time dependent recombination current density at the back contact (compare equation 2.37).

$$\tilde{J}\left(V_{DC},S_{n,bc}\right) = J_0exp\left\{\frac{qV_{DC}}{k_BT}\right\}\frac{q\hat{V}_{AC}}{k_BT}exp\{i\omega t\}\cdot\Xi^*\left(V_{DC},S_{n,bc}\right)$$

$$\Xi^*\left(V_{DC},S_{n,bc}\right) = \frac{1+\frac{\cosh(\xi^*)-1}{1+i\omega\tau_{n,a}}+\frac{D_{n,a}\sinh(\xi^*)}{L_{n,a}S_{n,bc}\sqrt{1+i\omega\tau_{n,a}}}}{\frac{D_{n,a}\cosh(\xi^*)}{L_{n,a}S_{n,bc}}+\frac{\sinh(\xi^*)}{\sqrt{1+i\omega\tau_{n,a}}}} \quad \textbf{2.54}$$

In equation 2.54 $\xi^*$ is the substitution of the complex ratio $\left(d_a\text{-}w_a(V_{DC})\right)/L^*_{n,a}$ and $J_0$ is the saturation current density from equation 2.32. Now, with the approximation $\left(1+i\omega\tau_{n,a}\right)^{1/2} \approx 1 + 1/2\cdot i\omega\tau_{n,a}$ [150] the diffusion capacitance $C_{diff,a} = Im(Y^*)/\omega$ can be obtained from the imaginary part of the complex admittance $Y^* = \tilde{J}/\hat{V}_{AC}exp\{i\omega t\}$ tested by the small ac signal, giving a complicate expression for the frequency dependent diffusion capacitance. Therefore, equation 2.55 deals with the frequency independent solution of $C_{diff,a}$ obtained for low frequencies $\omega << 1/\tau_{n,a}$. On the over hand in the case of $\tau_{n,a} \approx 10$ ns equation 2.55 holds up to a frequency of $\approx 10^7$ $s^{-1}$, which is beyond or in the vicinity of the maximum frequency achieved by the most commercial LCR meter.

$$C_{diff,a}\left(V_{DC},S_{n,bc}\right) = J_0\frac{q\cdot\tau_{n,a}}{2k_BT}exp\left\{\frac{qV_{DC}}{k_BT}\right\}\cdot\Gamma\left(V_{DC},S_{n,bc}\right)$$

$$\Gamma\left(V_{DC},S_{n,bc}\right) \quad \textbf{2.55}$$

$$= \frac{\xi\left(\frac{L^2_{n,a}S^2_{n,bc}}{D^2_{n,a}}-1\right)+2\frac{L_{n,a}S_{n,bc}}{D_{n,a}}\cosh\xi\,(\cosh\xi-1)+\left[\left(1+\frac{L^2_{n,a}S^2_{n,bc}}{D^2_{n,a}}\right)\cosh\xi-2\frac{L^2_{n,a}S^2_{n,bc}}{D^2_{n,a}}\right]\sinh\xi}{\left(\cosh\xi+\frac{L_{n,a}S_{n,bc}}{D_{n,a}}\sinh\xi\right)^2}$$

With $J_0$ from equation 2.32 it can be found in equation 2.55 that the diffusion capacitance is a

function of the minority charge carrier lifetime with $C_{diff,a} \propto \sqrt{\tau_{n,a}}$. The impacts of the geometrical dimensions and the back contact recombination on $C_{diff,a}$ are included in the dimensionless function $\Gamma(V_{DC},S_{n,bc})$ of equation 2.55. For thick absorber layers with $\xi = (d_a - w_a(V_{DC}))/L_{n,a} >> 1$ this function becomes $\Gamma(V_{DC},S_{n,bc}) \approx 1$ and the impact of $S_{n,bc}$ on $C_{diff,a}$ is negligible. However for thin absorbers $\xi \approx 1$ an increasing $S_{n,bc}$ would reduce $C_{diff,a}$. In the case of Figure 7 g) it can be shown with equation 2.55 that for $V_{DC}$ = 0.6 V the diffusion capacitance amounts to $C_{diff,a} \approx 0.13$ nF·cm$^{-2}$. Increasing $V_{DC}$ to 0.7 V produces after equation 2.55 a capacitance contribution of $C_{diff,a} \approx 6.42$ nF·cm$^{-2}$, fitting perfectly the difference of ≈ 6.72 nF·cm$^{-2}$ between simulated and calculated data.

To avoid unknown capacitance contributions like $C_{diff,a}$ in the interpretation of voltage dependent admittance spectroscopy data, in section 4.4 of this work only bias-voltages below 0.5 V were considered for device modelling.

## 2.3. Regions of recombination

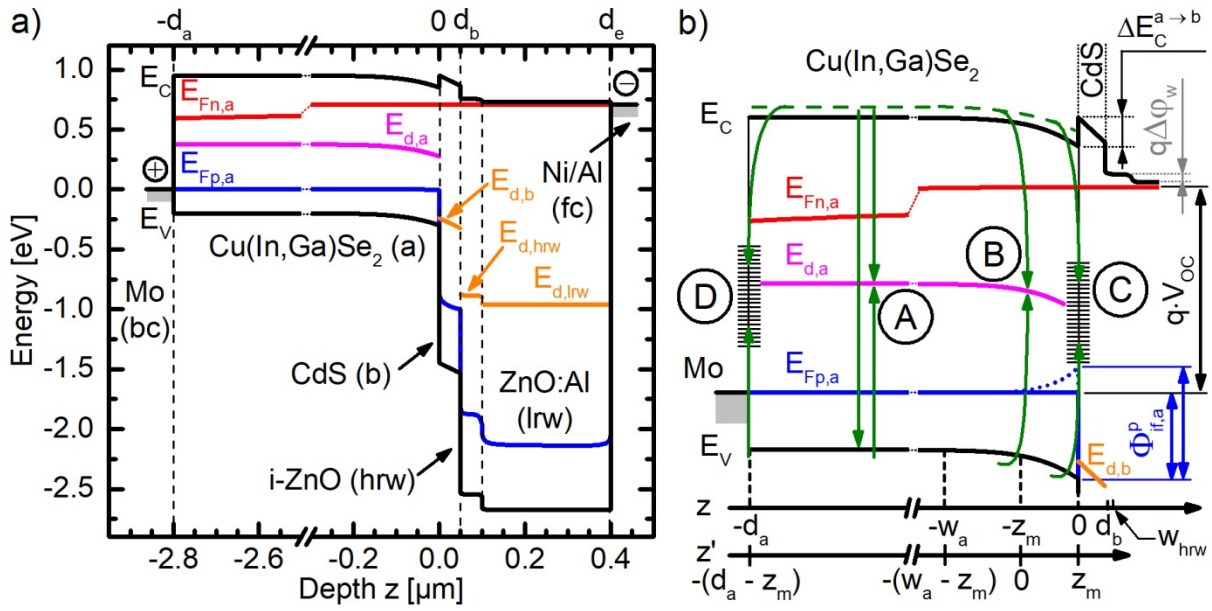


**Figure 9** (a) Band structure of the default device for a CIGSe solar cell given in Table A - 4, the bracketed abbreviations are indicating the functional layers with bc = back contact, a = absorber, b = buffer, hrw = high-resistance window, lrw = low-resistance window, and fc = front contact. $E_{d,x}$ (x = a, b, hrw, lrw) are defect levels located on midgap of the corresponding layer. $E_{Fp,a}$ and $E_{Fn,a}$ are the quasi Fermi levels within the absorber. The state of the solar cell correspond to the open circuit condition with illumination from the right hand side and T = 300 K. (b) Magnification of the absorber region including the hetero junction for illustrating the critical recombination paths. Here (A) represents recombination within the quasi neutral region, (B) recombination within the absorber's depletion region, (C) recombination at the absorber/buffer interface, and (D) interface recombination at the Mo back contact. $\Delta E_C^{a\rightarrow b}$ is the electron affinity related conduction band offset between absorber and buffer layer, $\Delta\varphi_w$ indicates the potential drop between the hr- and lr-window layer due to unequal doping densities. The hole barrier at the absorber/buffer interface is labelled by $\Phi_{if,a}^p$. The doted $E_{Fp,a}$ in the vicinity of z = 0 indicates the upward bending of the hole quasi-Fermi level for high defect densities $N_{d,if} \gtrsim 10^{12}$ cm$^{-2}$ at the interface.

Thus far the idealized solar cell was considered by neglecting recombination losses at the front interface and within the depletion region of the absorber. Figure 9 b) depicts the common recombination sites by means of the simplified band diagram of a CIGSe solar cell with an absorber band gap of $E_{g,a}$ = 1.15 eV (GGI ≈ 0.3). The operation mode of the solar cell in Figure 9 is under open circuit condition. In that case the generated charge carriers cannot leave the cell and have to recombine within the device over the four recombination paths (A) – (D) located within and at the interfaces of the absorber. Obviously, the recombination processes (A) – (D) are connected in parallel, with (A) recombination in the quasi neutral region (QNR), (B) recombination in the space charge region (SCR), (C) recombination at the

absorber/buffer interface (IF) and (D) recombination at the back contact (BC). A key factor of solar cell development and improvement is the knowledge about the dominating recombination path limiting the solar cell's open circuit voltage and consequently the efficiency. In the following the impact of the particular recombination regions on the solar cell's operation principle are treated more in detail by considering the default device given in Table A - 4.

### 2.3.1. (A) QNR recombination

In principle, the probability of dominating QNR recombination under $V_{OC}$ conditions enhances with increasing minority charge carrier lifetime. Provided that Auger recombination is negligible, then the highest possible lifetime is limited by radiative band to band recombination. Thus, a device limited by radiative recombination is sufficient to investigate the nature of QNR recombination within the absorber. For a device under $V_{OC}$ condition an important boundary condition is the approximation $[d_a - w_a(V_{OC})]/d_a \approx 1$, indicating the strongly reduced depletion width $w_a(V)$ for $V = V_{OC}$ and the existence of a QNR per se. This means that this approximation holds also for very low absorber doping densities, despite the absorber is completely depleted under 0 V as indicated by the $w_a(0V) = d_a$ line in Figure 10.
Without recombination of minority charge carriers at the back contact the derivatives at the beginning of section 2.2.1 are valid in Figure 10. Due to $L_{n,a} > d_a$ for low absorber doping densities the saturation current density $J_0 \rightarrow J_0(V)$ is a function of the voltage and can be determined by equation 2.31. From equation 2.33 the activation energy of $J_0$ of the p-$n^-$-n-$n^+$-structure in section 2.2 was found to be the band gap energy of the absorber ($E_A = E_{g,a}$). The reason for this finding has been related to the much higher band gaps of the buffer and window layers, which can be observed in Figure 9 a). Additionally, from equation 2.46 it becomes apparent that the smaller the reference current density $J_{00}$ the higher is $V_{OC}$, which is fulfilled for $N_{A,a}$, $\tau_{n,a}$, and $E_{g,a}$[4] as high as possible. In the case of radiative recombination the minority charge carrier lifetime results to $\tau_{n,a}^{max} = \tau_{n,a}^{rad} \approx (B \cdot N_{A,a})^{-1}$. B is the radiative recombination constant and can be derived from the van Roosbroeck-Shockley relation [152].

[4] The optimum band gap energy of solar cells – limited solely by radiative recombination – is defined by the Shockley-Queisser limit SQ2 in Figure 4 b) and is correspondingly given with $E_{g,a}^{opt} = 1.34$ eV.

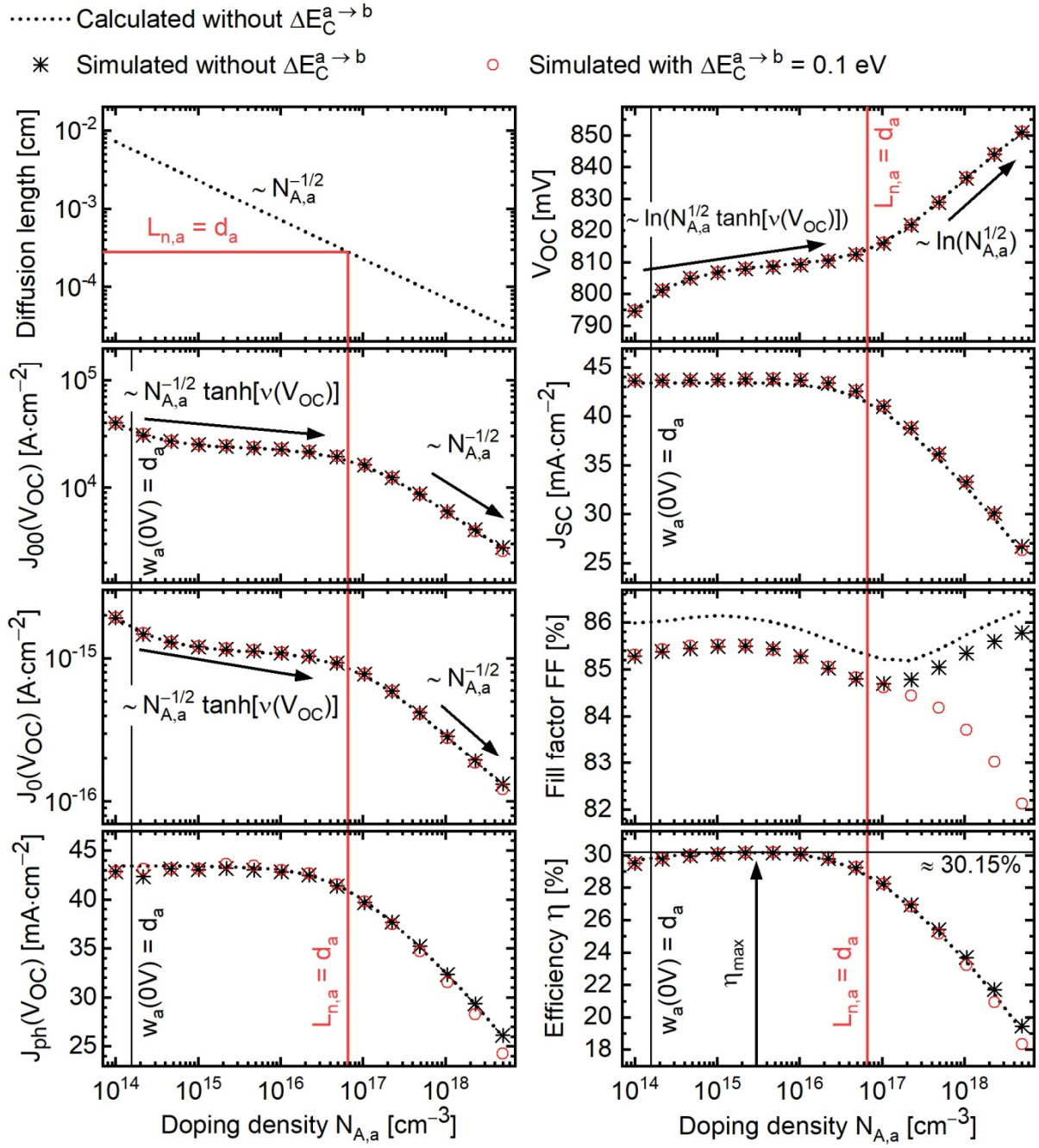


**Figure 10** Simulated (scattered symbols) and calculated (dotted lines) diode parameter for the default device characteristics given in Table A - 4. The band structure is depicted in Figure 9. Simulated data were generated with *Scaps 1d*. The simulations were performed with and without a band offset $\Delta E_C^{a\rightarrow b}$ of the CdS buffer layer. To ensure dominating QNR-recombination due to radiative recombination within the absorber bulk other recombination channels of minority charge carriers related to defects within the absorber, to the metal contacts, and to internal interfaces are omitted in this plot. The function $\nu(V_{OC}) = [d_a - w_a(V_{OC})]/L_{n,a}$ takes into consideration the geometric extension of a finite absorber on the diode current density as derived in equation 2.29.

Consequently, the maximum absorber doping density of the idealized solar cell is balanced with the radiative lifetime for electrons, neglecting band gap narrowing or the occurrence of band-to-band Auger recombination. Correspondingly, the radiative recombination rate $U_{rad,a}$ increases with increasing $N_{A,a}$, which also effects the collected photocurrent density $J_{ph}(V)$. $J_{ph}(V)$ can be obtained by integrating the continuity equation of the whole device under $J_{SC}$ condition [50, 153]

$$J_{ph}(V) = -q\eta_C(V) \int_{-d_a}^{d_e} \big(G(z) - U(z,0)\big)dz = \eta_C(V)\frac{J_{SC}}{\eta_C(0)}, \qquad \textbf{2.56}$$

where $-d_a$ denotes the back side of the absorber and $d_e$ the front side of the emitter (see Figure 9). U(z,0) is the depth dependent net recombination rate at V = 0 V. The voltage dependent collection efficiency $\eta_C$ of the absorber can be estimated to [154]

$$\eta_C(V) = \int_{E_{g,a}}^{\infty} 1 - \frac{exp\{-\alpha(E)w_a(V)\}}{1+\alpha(E)L_{n,a}}\,dE\,. \qquad \textbf{2.57}$$

With $w_a, L_{n,a} \propto N_{A,a}^{-1/2}$ it can be concluded from equations 2.56 and 2.57 that $N_{A,a}$ limits $J_{ph}(V_{OC})$ and $J_{SC} = J_{ph}(0)$. Especially when $L_{n,a}$ becomes smaller than the absorber thickness $d_a$ (compare red solid lines in Figure 10) the impact of $N_{A,a}$ on $J_{SC}$ and $J_{ph}$ becomes visible. Taking equation 2.46 into consideration the increase of $V_{OC}$ with higher $N_{A,a}$ is slightly reduced due to the decreasing $J_{ph}(V_{OC})$, compensating weakly the reduction of $J_{00}$ with increasing $N_{A,a}$.

On the bottom of the right hand side in Figure 10 it becomes apparent that increasing $N_{A,a}$ above $10^{17}$ $cm^{-3}$ reduces eminently the device efficiency η. Reason is the strongly decreasing short circuit current density due to the reduction in collection efficiency $\eta_C(0)$ with decreasing $w_a$ and $L_{n,a}$. This means that the increasing $V_{OC}$ for $N_{A,a} \gtrsim 10^{17}$ $cm^{-3}$ in Figure 10 is not able to compensate the reduction in efficiency η due to the decreasing $J_{SC}$. The connection of η, $V_{OC}$, and $J_{SC}$ is given in equation 2.58.

$$\eta = FF \cdot \frac{J_{SC}V_{OC}}{E_s} \qquad \textbf{2.58}$$

FF in equation 2.58 represents the fill factor and $E_s$ stands for the energy flux density of irradiated sun light.

An impact on the J-V-characteristics in Figure 10 due to a band offset $\Delta E_C^{a\rightarrow b}$ = 0.1 eV between the CIGSe absorber and CdS buffer layer (compare Figure 9 b)) becomes noticeable not until $N_{A,a} \gtrsim 10^{17}$ $cm^{-3}$, which is expressed by reduced $J_{ph}(V_{OC})$ and FF. In the case that the

band offset would exceed $\Delta E_C^{a\rightarrow b} \gtrsim 0.3$ eV the reflection of electrons at the CIGSe/CdS interface back into forward direction starts to reducing $J_{SC}$, FF, and the device efficiency independent from $N_{A,a}$. On the other hand for voltages close to $V_{OC}$, $\Delta E_C^{a\rightarrow b} \gtrsim 0.3$ eV effects a positive jump of $E_{Fn}$ at the absorber/buffer interface, increasing $V_{OC}$. However, $J_{SC}$ and $V_{OC}$ are not influenced in Figure 10 over the whole $N_{A,a}$ range for such a small-sized band offset of $\Delta E_C^{a\rightarrow b} = 0.1$ eV as depicted in Figure 9 b). Equally, no noticeable impact of $\Delta E_C^{a\rightarrow b} = 0.1$ eV on the saturation current density is observed in Figure 10.

In Figure 9 a) the absorber is spatially extended to $-d_a = 2.8$ µm. The finite absorber causes a characteristic point with $L_{n,a} = d_a$ for the diode parameter $J_0(V_{OC})$, $J_{00}(V_{OC})$, and $V_{OC}$ in Figure 10. This point indicates that if the diffusion length minority charge carriers is significantly smaller than the thickness of the absorber $L_{n,a} << d_a$ the hyperbolic tangent in equation 2.31 becomes ≈ 1. Thus, the approximation on the right hand side of equation 2.31 is still valid and the proportionalities of the characteristic parameter to $N_{A,a}$ follow from equations 2.32 and 2.46 to $J_0 \propto N_{A,a}^{-1/2}$ and $V_{OC} \propto \ln\left(N_{A,a}^{1/2}\right)$. However, in the vicinity and on the left hand side of the demarcation line $L_{n,a} = d_a$ the impact of $\tanh([d_a - w_a(V_{OC})]/L_{n,a}) = \tanh[\nu(V_{OC})]$ on $J_0$ in equation 2.31 is not negligible anymore. With the effect that the increasing $\tanh[\nu(V_{OC})]$ with decreasing $L_{n,a} \propto N_{A,a}^{-1/2}$ nearly compensates the reduction of $J_0$ and the concomitant enhancement of $V_{OC}$ for increasing doping densities.

### 2.3.2. (B) SCR recombination

If only radiative recombination is active, optimum diode parameter for the default device, depicted in Figure 9 with the physical quantities in Table A - 4, were found for $N_{A,a}$ in the range of $10^{15} – 10^{16}$ cm$^{-3}$ (see the arrow $\eta_{max}$ in Figure 10). In the latter case the equations of section 2.2.1 are still applicable. However, if recombination via deep defects becomes active equations 2.45 and 2.46 have to be supplemented by the diode ideality factor A.

$$J_{diode}(V) = J_0\left(exp\left\{\frac{qV}{Ak_BT}\right\} - 1\right) - J_{ph}(V) \qquad \textbf{2.59}$$

$$V_{OC}(T) = \frac{E_A}{q} - \frac{Ak_BT}{q} ln\left(\frac{J_{00}}{J_{ph}(V_{OC})}\right) \qquad \textbf{2.60}$$

For a device without shunt paths or tunnelling enhanced recombination the diode ideality factor lies in the range between 1 and 2 [155], where A = 1 represents solely dominating recombination within the QNR (or in exceptional cases at the CIGSe/CdS interface see

below) and A > 1 partial or dominating recombination within the SCR. However, the diode ideality factor is not a constant quantity either due to the decreasing SCR width with increasing forward bias or due to saturation of recombination levels with rising charge carrier injection aroused by high forward currents. Thus, Figure 11 depicts the A-factor and $J_0$ under $V_{OC}$ condition as a function of the absorber doping $N_{A,a}$ in column a), the ratio of defect density and doping concentration $N_d/N_{A,a}$ with $N_{A,a}$ fixed to $7 \cdot 10^{15}$ $cm^{-3}$ in column b). Further shows Figure 11 in column c) the impact of the defect level $E_d - E_V$ and in column d) the ratio of the capture cross sections $\sigma_n/\sigma_p$, where $\sigma_p$ was varied and $\sigma_n = 10^{-12}$ $cm^2$ was retained constant. To keep the donor type character of the defect level $\sigma_p > \sigma_n$ was dispensed. If not stated otherwise for simulations in Figure 11 defect and device properties were utilized from Table A - 4. The arrows and solid lines in Figure 11 are indicating the specified default values of the CIGSe absorber in Table A - 4. Further, for simplification recombination of minority charge carriers at the metal contacts and internal interfaces was omitted, but not radiative recombination within the absorber.

As shown in Figure 11 the condition of $A(V_{OC}) = 2$ under $V_{OC}$ condition is hard to achieve with a device involving a hetero junction as depicted in Figure 9, even if the recombination centres are located at midgap of the absorber. With $A(V_{OC}) > 1.33$ (resulting from equation 2.62) represented by the horizontal dotted line in the first row of Figure 11, there are 2 conditions in Figure 11 where recombination within the SCR becomes dominant. In the first case for high defect densities $N_d > 10^{14}$ $cm^{-3}$ ($N_d/N_{A,a} > 1.4 \cdot 10^{-2}$) in column b) and in the second case for high capture cross sections $\sigma_p/\sigma_n \approx 1$ in column c). Following the solid lines in Figure 11 the default model (without interface states) can be considered as dominated by QNR recombination with $A(V_{OC}) \approx 1$.

The depicted cardinal parameters ($V_{OC}$, $J_{SC}$, FF, η) in Figure 11 derived from illuminated J-V-curves exhibit a distinct correlation between $V_{OC}$ and $J_0(V_{OC})$. In turn $J_0(V_{OC})$ and $A(V_{OC})$ are weakly correlated to each other, and are following equal trends in every column of Figure 11. However, it appears that $A(V_{OC})$ shows a lower sensitivity to the change of defect parameters than $J_0(V_{OC})$. A-factors and saturation current densities in Figure 11 have been extracted from simulated spatially resolved recombination rates under $V_{OC}$. The diode current density $J_{diode}(V)$ was estimated with the following 2 diode model described by equation 2.61.

$$J_{diode}(V) = J_{01}(V)\left(exp\left\{\frac{qV}{k_B T}\right\} - 1\right) + J_{02}(V)\left(exp\left\{\frac{qV}{2k_B T}\right\} - 1\right) - J_{ph}(V) \qquad \textbf{2.61}$$

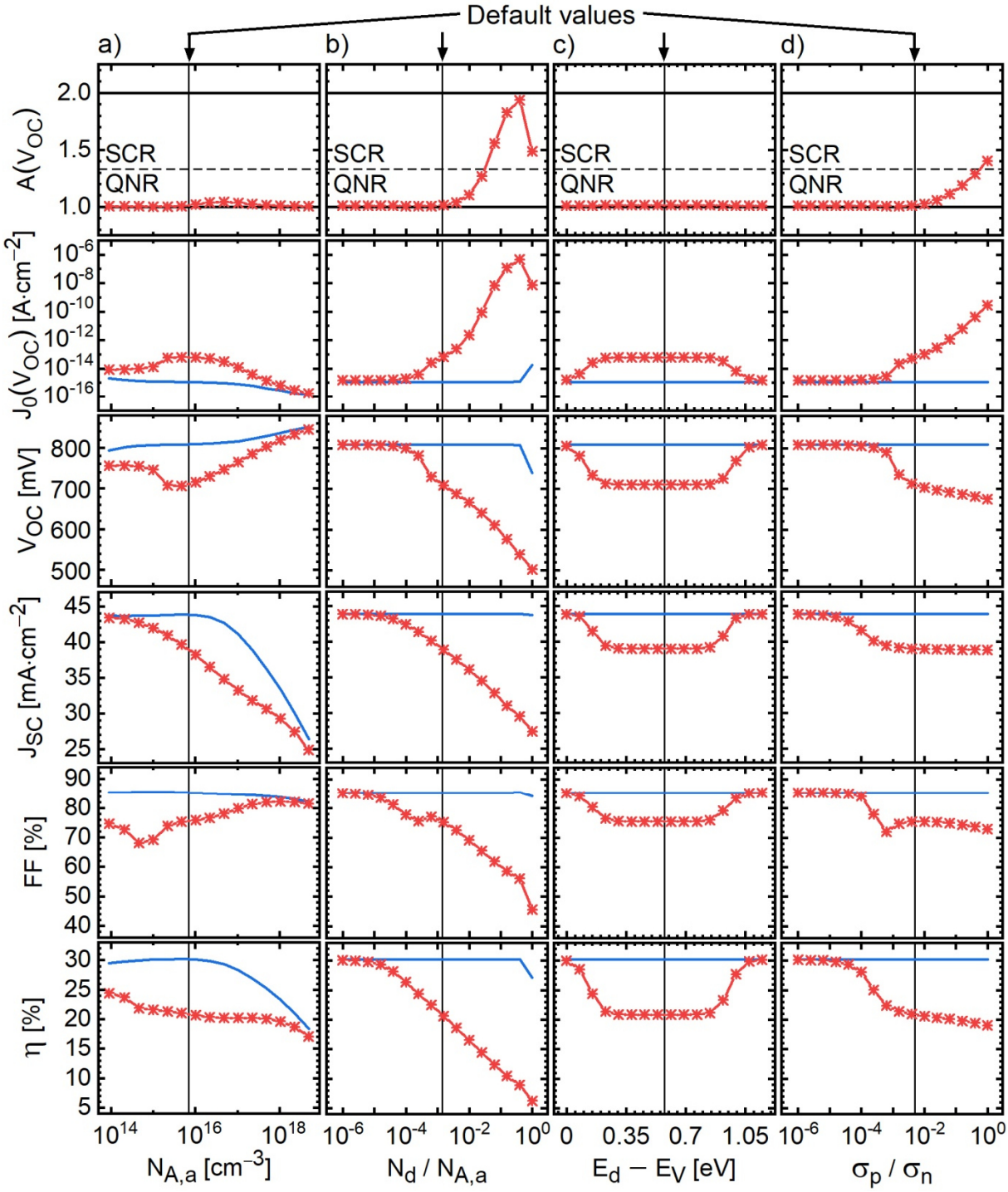


**Figure 11** Simulated J-V-parameter to investigate the impact on the device characteristics of a donor type bulk defect placed within the band gap of the absorber. Simulations were performed on the default device given in Table A - 4 without recombination of charge carriers at internal interfaces or of minority charge carriers at the metal contacts. Column a) depicts the J-V-characteristics as a function of the shallow acceptor density $N_{A,a}$ of the absorber, the trap parameter were fixed to the values in Table A - 4. The impact of the defect properties are shown in column b) with varying density $N_d$ of the trap states normalized to $N_{A,a} = 7 \cdot 10^{15}$ cm$^{-3}$, in column c) with a variable trap level $E_d - E_V$ and in column d) with a versatile hole capture cross section $\sigma_p$ normalized to $\sigma_n = 10^{-12}$ cm$^2$. If not stated otherwise all physical parameter for simulating a) - d) are corresponding to the given values in Table A - 4. The dotted lines are obtained on a device in the radiative limit, to emphasize the impact of the particular defect parameter.

On the right hand side of equation 2.61 the first term correspond to the recombination current density within the QNR and the second term to the recombination current density within the depletion region of the absorber. Both saturation current densities $J_{01}$ and $J_{02}$ become available by integrating the recombination rate over the particular thickness of QNR and SCR under $V_{OC}$. From the saturation current densities $J_{01}$ and $J_{02}$ of the 2 diode-model in equation 2.61 it is hard to discriminate between dominating QNR or SCR recombination. Further, direct relations between J-V-parameters like $V_{OC}$ and $J_{01}$ as well as $J_{02}$ are not unambiguous. Thus in Figure 11 $A(V_{OC})$ and $J_0(V_{OC})$ of the 1 diode model derived from the 2 diode model parameter were utilized to disclose interrelations of the J-V-parameters and the diode equation. By linearization of equations 2.59 and 2.61 with a Taylor expansion in the vicinity of $V_{OC}$ and equating them the diode quality factor $A(V_{OC})$ becomes available after following equation.

$$A(V_{OC}) = \frac{J_{01} exp\left\{\frac{qV_{OC}}{2k_BT}\right\} + J_{02}}{J_{01} exp\left\{\frac{qV_{OC}}{2k_BT}\right\} + \frac{1}{2}J_{02}}. \qquad \textbf{2.62}$$

After obtaining $A(V_{OC})$ with equation 2.62, the saturation current density $J_0(V_{OC})$ of the 1 diode-model becomes determinable with equation 2.59. The knowledge of $A(V_{OC})$ gives the possibility to discriminate between dominating recombination within the QNR ($A < 1.33$) and dominating recombination within SCR ($A > 1.33$) under $V_{OC}$ condition.

The increased $J_0$ and decreased J-V-parameter in column b) of Figure 11 for radiative limited recombination (blue solid line) – acting as the reference – is ascribed to the compensation effect in the case of $N_d \approx N_{A,a}$, resulting from the definition of donor type defect states. Further reveals $A(V_{OC})$ and $J_0(V_{OC})$ in column b) an unexpected reduction for the highest defect concentration $N_d/N_{A,a} = 10^0$. This is in turn a consequence of the compensated absorber doping due to donor type defect states. The lower hole concentration effects that the recombination rate of electrons reduces within the SCR and an higher concentration of electrons is injected into the QNR of the absorber, reducing $A(V_{OC})$. On the other hand the reduction of $J_0$ indicates that the diode current density becomes limited by the lower hole concentration of the absorber. However, this reduction of $J_0$ is not translated into an improvement of $V_{OC}$. The reason is the strongly reduced photocurrent density $J_{ph}(V_{OC})$ as indicated by the accelerated decrease in FF.

In column a) of Figure 11 the decreasing $V_{OC}$ with increasing doping density in the range of $10^{14}$ .. $5 \cdot 10^{15}$ $cm^{-3}$ originates from the asymmetric capture cross sections $\sigma_n = 10^{-12}$ $cm^2$ for electrons and $\sigma_p = 5 \cdot 10^{-15}$ $cm^2$ for holes. As a result, the recombination current density over the defect level is limited by holes for low $N_{A,a}$. Appropriate, with increasing doping density

the saturation current density $J_0(V_{OC})$ increases and $V_{OC}$ decreases. In the case that $N_{A,a}$ exceeds $5 \cdot 10^{15}$ $cm^{-3}$ the recombination process becomes solely limited by electrons and $J_0$ starts to decreasing, effecting an increasing $V_{OC}$. Reaching very high doping densities, all quantities in column a) of Figure 11 are converging to the values of the radiative limited device. The declining and increasing trend of $V_{OC}$ as a function of $N_{A,a}$ in column a) of Figure 11 should be taken into account by the interpretation of $V_{OC}(t)$-measurements (see section 3.1.2).

Analytically, the diode current can be derived from the product of the charge carrier densities $n \cdot p \rightarrow (n \cdot p)^{1/A}$ within the particular bands [50]. This approach follows from the high injection condition within the depletion region. Under the assumption of constant quasi-Fermi levels within the SCR the charge carrier product can be rewritten to

$$(n \cdot p)^{\frac{1}{A}} = n_i^{\frac{2}{A}} exp\left\{\frac{E_{Fn} - E_{Fp}}{Ak_BT}\right\} = \left(N_{C,a}N_{V,a}\right)^{\frac{1}{A}} exp\left\{-\frac{E_{g,a}}{Ak_BT}\right\} exp\left\{\frac{qV}{Ak_BT}\right\}. \qquad \textbf{2.63}$$

Now, the charge carrier densities at the point $-z_m$ of maximum recombination $U_m$ (Figure 9 b)) can be determined with equation 2.63 by using the relation $\tau_{p0} \cdot n(-z_m) = \tau_{n0} \cdot p(-z_m)$. By approximation, in the vicinity of $-z_m$ the recombination rate decays to each side of the pn-junction exponentially with a characteristic length of $(k \cdot T)/(q \cdot E_{z,m})$, where $E_{z,m}$ denotes the electric field at $-z_m$ [156]. Integration of the recombination rate over the depletion region of the absorber delivers the recombination current:

$$J_{SCR} = q \int_{-w_a}^{0} U(z)dz = q \int_{-(w_a - z_m)}^{z_m} U(z')dz'. \qquad \textbf{2.64}$$

An exact solution of the integral in equation 2.64 requires the knowledge of the position dependent energetic distance of the quasi Fermi-levels to the respective band edges as a function of the applied voltage within the SCR [156]. In that case a system of non-linear differential equations has to be solved, wherefore device simulation is usually indispensable. However, with the simplification that $U_m$ decays exponentially in +z- and –z-direction and inserting equation 2.63 into the Shockley-Read-Hall (SRH) [112] equation an analytical expression for $J_{SCR}$ can be derived to

$$J_{SCR}(V) \approx \frac{\pi}{2} \cdot \frac{k_B T}{E_{z,m}} \cdot \left( \frac{N_{C,a} N_{V,a}}{\tau_{n0} \tau_{p0}} \right)^{\frac{1}{A}} exp\left\{ -\frac{E_{g,a}}{A k_B T} \right\} \left( exp\left\{ \frac{qV}{A k_B T} \right\} - 1 \right)$$
$$= J_{00} exp\left\{ -\frac{E_{g,a}}{A k_B T} \right\} \left( exp\left\{ \frac{qV}{A k_B T} \right\} - 1 \right) = J_0 \left( exp\left\{ \frac{qV}{A k_B T} \right\} - 1 \right). \quad \textbf{2.65}$$

In correspondence to dominating recombination within the QNR, from equation 2.65 an activation energy of $E_A = E_{g,a}$ for $J_0$ can be obtained as well. Thus, if recombination dominates in the SCR a $V_{OC}(T)$-measurement should reveal the band gap energy of the absorber (see section 3.1.1).

### 2.3.3. (C) Interface recombination

The recombination rate of charge carriers over interface states is described by the model of Pauwels and Vanhoutte [157]. In contrast to the usual Shockley-Read-Hall recombination, where the occupation density of the investigated defect level depends on two carrier concentrations p and n, the occupation density of interface states can depend on 4 different carrier concentrations in accordance to Figure 9 given with $p_{if,a}$, $p_{if,b}$, $n_{if,a}$ and $n_{if,b}$ [158]. Then, with the SRH-equation [112] the net recombination rate $U_{SRH,if}$ of charge carriers over a discrete defect level ($E_{d,if}$, $N_{d,if}$) at the CIGSe/CdS interface (see Figure 9) under an applied bias voltage and/or illumination can be given as

$$U_{SRH,if}(V) = \frac{n_{if} p_{if,a} - n_{i,a}^2}{\frac{1}{\sigma_p v_p N_{d,if}} (n_{if} - n_1) + \frac{1}{\sigma_n v_n N_{d,if}} (p_{if,a} - p_1)}, \quad \textbf{2.66}$$

where $n_{if}$ denotes the higher non-equilibrium electron concentration either $n_{if,a}$ at $z = z \rightarrow 0^-$ within the absorber or $n_{if,b}$ at $z = z \rightarrow 0^+$ within the buffer layer [159]. Due to the positive band offset $\Delta E_C^{a \rightarrow b} > 0$ (see Figure 9 b)) it is highly probable under forward biasing that the higher electron concentration is located within the absorber with $n_{if,a}$ at $z = z \rightarrow 0^-$. On the other hand the higher intrinsic $n_{i,a}$ and the higher non-equilibrium hole concentration $p_{if,a}$ are located invariably within the absorber. By virtue of interface defects $[N_{d,if}] = cm^{-2}$ the pre-factors of the denominator correspond to recombination velocities $S_{n,if}$, $S_{p,if}$ for electrons and holes, respectively.

$$S_{n,if} = \sigma_n v_n N_{d,if}$$
$$S_{p,if} = \sigma_p v_p N_{d,if} \qquad \textbf{2.67}$$

Usually, the variables $p_1 = N_{V,a}\exp\{-(E_{d,if} - E_{V,a})/k_B T\}$, $n_1 = N_{C,a}\exp\{-(E_{C,a} - E_{d,if})/k_B T\}$, and $n_{i,a}^2$ in equation 2.66 are negligible in comparison to the non-equilibrium charge carrier densities $n_{if,a}$ and $p_{if,a}$. This is true, if the trap level is located at midgap $E_{g,a}/2$ of the absorber and if a high positive Fermi-level splitting is existent as it is the case under $V_{OC}$.

To evaluate the impact of recombination centres at the interface on the J-V-characteristics of a solar cell one has to distinguish between donor and acceptor type defects and additionally has to regard the Fermi-level position at the interface. According to Figure 9, this requires to solving the Poisson equation for a p-$n^-$-n-$n^+$-junction with a complete depleted buffer as well as a partial depleted high resistance window (hrw) layer as conducted in section 2.2, but now with additional charge states at the absorber/buffer interface. In that case the charge neutrality condition in the depletion approximation of the hetero-junction reads

$$qN_{A,a}w_a + qn_{A,if}^- = qN_{D,hrw}w_{hrw} + qN_{D,b}d_b + qn_{D,if}^+. \qquad \textbf{2.68}$$

In eqation 2.68 $n_{A,if}^-$ and $n_{D,if}^+$ denote the ionized acceptor, respectively donor type trap states at the interface. The density $n_{d,if}$ of occupied interface defects is governed by the following rate equation

$$\frac{dn_{d,if}}{dt} = \frac{1}{N_{d,if}}\left[S_{n0,if}n_{if,a}(N_{d,if} - n_{d,if}) - S_{p0,if}p_{if,a}n_{d,if}\right]_{Capture} + \frac{1}{N_{d,if}}\left[S_{p0,if}(N_{d,if} - n_{d,if})p_1 - S_{n0,if}n_{d,if}n_1\right]_{Emission}, \qquad \textbf{2.69}$$

where the first cornered bracket term indicates the capture rates and the second one the emission rates (in line with [106]). In steady state $dn_{d,if}/dt = 0$ and by inserting equation 2.66 into 2.69, further with the relation $n_{i,a}^2 = p_1 n_1$ the ionized acceptor or donor trap density at the interface in equation 2.68 can be determined to

$$n_{A,if}^- = \frac{S_{n,if}n_{if,a} + S_{p,if}p_1}{S_{n,if}(n_{if,a} - n_1) + S_{p,if}(p_{if,a} - p_1)}N_{d,if} = \gamma_{A,if}N_{d,if}$$
$$n_{D,if}^+ = (1 - \gamma_{A,if})N_{d,if} = \gamma_{D,if}N_{d,if}. \qquad \textbf{2.70}$$

The quantities $\gamma_{A,if}$ and $\gamma_{D,if}$ are voltage dependent, since $n_{if}$ and $p_{if,a}$ are functions of the voltage. Regarding the default model in Figure 9 the depletion approximation in equation 2.68 holds merely for bias voltages close to $V_{OC}$ and produces slight deviations (< 3%) between analytical and simulated potentials, respectively barrier heights $\Phi^{p}_{if,a}(V_{OC})$ in Figure 12 b) for bulk limitation. (The deviations between calculations and simulations of the strong IF-limited devices are of other nature and discussed later in this section.) However, at lower voltages, especially $V \leq 0$, the assumption of i. e. a partially depleted hrw-layer is not fulfilled anymore for a high concentration of acceptor states at the interface and the error of the analytical solution increases.

*Donor type interface states:*

In the case of a discrete donor level with $E_{d,if} \approx E_{g,a}/2$ and a type inversion of the absorber with $N_{A,a} << N_{D,hrw}$ at the interface, it can be assumed that $S_{n,if}n_{if,a} >> S_{p,if}p_{if,a}$. Accordingly, equation 2.66 can be simplified to

$$U_{SRH,if}(V) \approx S_{p,if}p_{if,a} = S_{p,if}N_{V,a}exp\left\{-\frac{\Phi^{p}_{if,a}(V)}{k_BT}\right\} \qquad \textbf{2.71}$$

and the voltage dependent recombination current density $J_{if}$ follows with

$$J_{if}(V) = qS_{p,if}N_{V,a}exp\left\{-\frac{\Phi^{p}_{if,a}(V)}{k_BT}\right\} \overset{!}{=} J_0\left(exp\left\{\frac{qV}{Ak_BT}\right\} - 1\right). \qquad \textbf{2.72}$$

Under the condition of a constant hole quasi Fermi-level $E_{Fp,a}$ within the depletion region of the absorber (see Figure 9) the hole barrier $\Phi^{p}_{if,a}$ is described by

$$\Phi^{p}_{if,a}(V) = \left(E_{Fp,a}(V) - E_{V,a}(V)\right)_{z=0} = \left(E_{Fp,a} - E_{V,a}\right)_{QNR} + q\varphi_{if,a}(V). \qquad \textbf{2.73}$$

Hence, for further examinations the voltage dependent potential $\varphi_{if,a}$ (V) at the interface (z = 0) of the absorber has to be determined via solving the Poisson equation for the structure depicted in Figure 9. Following the assumption that the donor trap level at the interface is discrete and located on $E_{g,a}/2$ an additional contribution to the SCR by these chargeable defects becomes negligible, because of $\exp\{-(E_F-E_{d,if})/k_BT\} \approx 0$, if the type inversion of the absorber at the interface is strong enough in equilibrium. This holds even under illumination or voltage biasing, since $\gamma_{D,if} \approx 0$ for $E_{d,if} \approx E_{g,a}/2$ and $S_{n,if}n_{if} >> S_{p,if}p_{if,a}$. On the other hand an additional downward band bending within the absorber is induced by the different electron

affinities of the CIGSe and CdS layers with $\chi_{CIGSe} - \chi_{CdS} = 0.1$ eV. As well, the positive band offset represents an electron barrier at the CIGSe/CdS interface and enhances further the downward band bending of the absorber due to an increased electron concentration at the absorber surface. This situation requires to solve the Poisson-Boltzmann equation, which considers also the mobile charge carriers for the position and voltage dependent potential. However, an analytical solution of this non-linear problem is hard to achieve even with appropriate simplifications [160, 161]. Therefore, hereinafter the analytical problem is treated without a band offset between absorber and buffer layer. This does not changes the previous assumption of the recombination rates at the interface, since $p_{if,a} >> p_{if,b}$.

By inserting equation 2.16 into 2.11 the potential $\varphi_{if,a}(V)$ at the absorber/buffer interface results to

$$\varphi_{if,a}(V) = \vartheta \cdot \Delta\varphi_{SCR}(V) + \varphi^* \left( 1 + \frac{\beta}{2} - \sqrt{1 + \beta + 2\vartheta \frac{\Delta\varphi_{SCR}(V)}{\varphi^*}} \right). \qquad \textbf{2.74}$$

Hence, one will find that the square root voltage term in equation 2.74 impedes the direct comparison of the left hand and right hand side in equation 2.72. This problem can be overcome in accordence to Ref. [159] by linearization of $\varphi_{if,a}$ with a Taylor expansion at $V_{OC}$. Thus, in the vicinity of $V_{OC}$, equation 2.74 can be rewritten to

$$\begin{aligned} \varphi_{if,a}(V) \approx\ & \vartheta(V_{bi} + \Delta\varphi_w) + \varphi^* \left( 1 + \frac{\beta}{2} - \sqrt{1 + \beta + 2\vartheta \frac{\Delta\varphi_{SCR}(V_{OC})}{\varphi^*}} \right) \\ & - \vartheta V_{OC} \Big/ \sqrt{1 + \beta + 2\vartheta \frac{\Delta\varphi_{SCR}(V_{OC})}{\varphi^*}} + \left( \vartheta \Big/ \sqrt{1 + \beta + 2\vartheta \frac{\Delta\varphi_{SCR}(V_{OC})}{\varphi^*}} - \vartheta \right) V. \end{aligned} \qquad \textbf{2.75}$$

As specified in section 2.2 for calculating potentials, the correction term $V_{corr}$ does not enter into $\Delta\varphi_{SCR}(V_{OC})$ in equation 2.17. Inserting the linearized potential into equation 2.73 gives the hole barrier for the recombination current density $J_{if}$ over IF-states on the left hand side in equation 2.72. By a comparison of coefficients the sought quantities $J_0$ and A of $J_{if}$ on the right hand side of equation 2.72 can be directly determined and follow with

$$A = \left( \vartheta - \vartheta \Big/ \sqrt{1 + \beta + 2\vartheta \frac{\Delta\varphi_{SCR}(V_{OC})}{\varphi^*}} \right)^{-1} \qquad \textbf{2.76}$$

$$J_0 = qS_{p,if}N_{A,a}\left(\frac{N_{V,a}N_{C,lrw}}{N_{A,a}N_{D,hrw}}\right)^{\vartheta} exp\left\{-(k_BT)^{-1}\left[\vartheta E_{g,a}\right.\right.$$
$$\left.\left. + q\varphi^*\left(1+\frac{\beta}{2}-\sqrt{1+\beta+2\vartheta\frac{\Delta\varphi_{SCR}(V_{OC})}{\varphi^*}}\right) - qV_{OC}\vartheta\Big/\sqrt{1+\beta+2\vartheta\frac{\Delta\varphi_{SCR}(V_{OC})}{\varphi^*}}\right]\right\}. \quad \textbf{2.77}$$

The activation energy $E_A$ of the saturation current density can be obtained by the ansatz $J_0 = J_{00}\exp[-E_A/(Ak_BT)]$ and comparison of coefficients. However, the square roots and the unknown function $\Delta\varphi_{SCR}(V_{OC})$ in equation 2.77 inhibit the direct extraction of $E_A$ with

$$\frac{E_A}{Ak_BT} = \frac{1}{k_BT}\cdot\left(\vartheta E_{g,a} + q\varphi^*\left(1+\frac{\beta}{2}\right) - \frac{q\varphi^*\left(1+\beta+2\vartheta\frac{\Delta\varphi_{SCR}(V_{OC})}{\varphi^*}\right)+qV_{OC}\vartheta}{\sqrt{1+\beta+2\vartheta\frac{\Delta\varphi_{SCR}(V_{OC})}{\varphi^*}}}\right). \quad \textbf{2.78}$$

The right hand side of equation 2.78 is the transformed argument of the exponential function in equation 2.77. $E_A$ becomes available from equation 2.78 by generating the limits of $qV_{OC}(T)$ and $q\Delta\varphi_{SCR}(V_{OC},T)$ for $T \rightarrow 0$ K.

$$\lim_{T\to 0} qV_{OC}(T) \overset{!}{=} E_A \quad \textbf{2.79}$$

$$\lim_{T\to 0} q\Delta\varphi_{SCR}(V_{OC},T) = E_{g,a} - E_A \quad \textbf{2.80}$$

With the assumption that the net doping densities and material constants in equations 2.14, 2.17, and 2.18 are temperature independent, the activation energy is found to be

$$E_A = E_{g,a} + \frac{\beta}{2\vartheta}q\varphi^* = E_{g,a} + \frac{q^2d_b^2N_{D,b}^2}{2}\left(\frac{1}{\varepsilon_bN_{D,b}} - \frac{1}{\varepsilon_{hrw}N_{D,hrw}}\right). \quad \textbf{2.81}$$

From equation 2.81 it becomes apparent that in the case of dominating interface recombination the activation energy of $J_0$ exceeds $E_{g,a}$ by an expression depending on the thickness of the buffer layer as well as the doping densities of buffer and high resistance window layer. However, the additional contribution to $E_A$ by this expression is marginal i.e. for the default model given in Table A - 4, where $d_b$ = 50 nm, $N_{D,b} = 10^{15}$ cm$^{-3}$ and $N_{D,hrw} = 7.1\cdot10^{17}$ cm$^{-3}$, the activation energy increases by a small amount of 2.3 meV.

To evaluate the analytical model, Figure 12 a) shows calculated and simulated $V_{OC}$ values as a function of the donor defect density at the absorber/buffer interface of the default model in

Table A - 4. Simulations were performed with and without a band offset of 0.1 eV. For simplification the bulk defect of the absorber was removed. Thus, the problem reduces to a bulk recombination limited device (in the radiative limit) for low $N_{d,if}$ values and an IF-recombination limited device for high $N_{d,if}$ values. This leads to a 2 diode equation for the current density at $V_{OC}$

$$J(V_{OC}) = J_{0,if}\left(exp\left\{\frac{qV_{OC}}{A_{if}k_BT}\right\} - 1\right) + J_{0,bulk}\left(exp\left\{\frac{qV_{OC}}{A_{bulk}k_BT}\right\} - 1\right) - J_{ph}(V_{OC}) \overset{!}{=} 0 \qquad \textbf{2.82}$$

with $A_{bulk} = 1$. The quantities $A_{if}$, $J_{0,if}$, and $J_{0,bulk}$ are calculated with equations 2.76, 2.77, and 2.32, respectively.

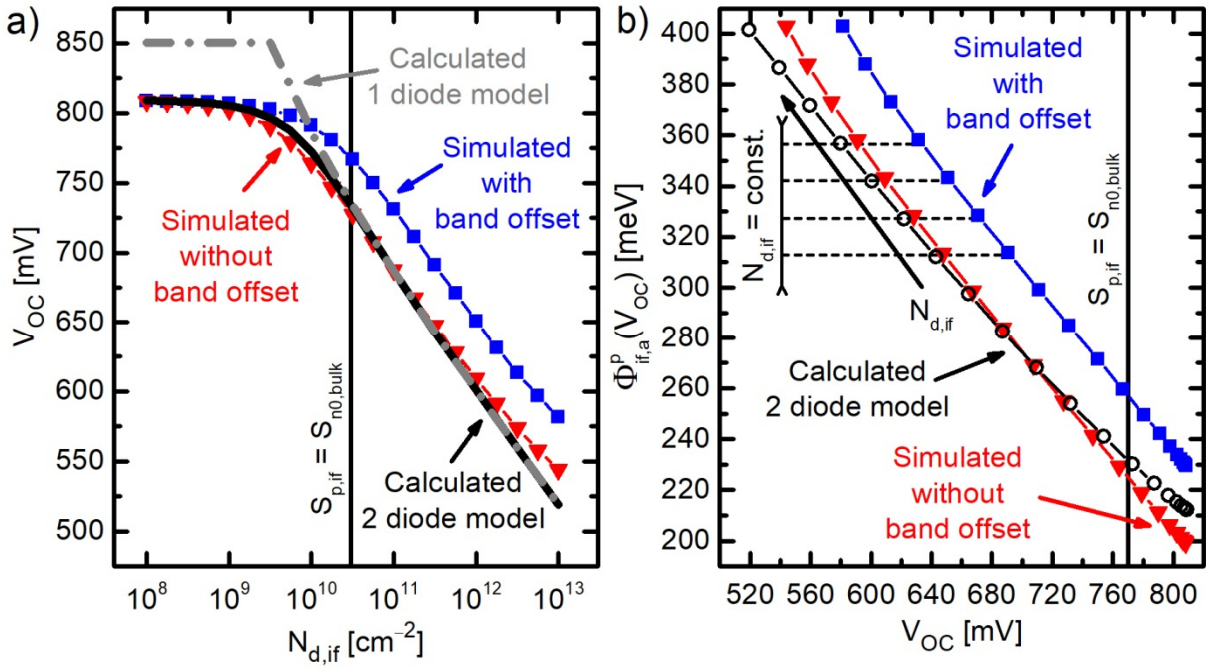


**Figure 12** (a) Simulated and calculated $V_{OC}$ as a function of the donor defect density at the absorber/buffer interface. The data were obtained using the default model in Table A - 4 without bulk defects within the absorber. (b) Hole barrier $\Phi^p_{if,a}$ at the interface calculated with equation 2.73 and plotted against $V_{OC}$ as a function $N_{d,if}$ from (a).

The impact of the band offset between absorber and buffer layer on $V_{OC}$ is demonstrated in Figure 12 a). When $\Delta E_C^{a\rightarrow b}$ changes from 0 to 0.1 eV, $V_{OC}$ increases almost constantly by ≈ 40 mV in the case of dominating IF-recombination. The origin of this phenomenon can be understood from Figure 12 b). Because of the additional downward band bending induced by the different electron affinities of absorber and buffer layer a higher bias voltage ($V_{OC}$)

becomes necessary to reduce the hole barrier $\Phi^{p}_{if,a}$ at the interface. Indicated by the constant $N_{d,if}$ levels in Figure 12 b), $\Phi^{p}_{if,a}(V_{OC})$ is identical for the 3 models. This supports the approach in equations 2.71 and 2.72 that the diode current is solely limited by holes at the interface, if the type inversion of the absorber is strong enough.

At high defect concentrations $N_{d,if} > 10^{12}$ cm$^{-2}$ in Figure 12 the deviation between simulated and calculated $V_{OC}$ values begins to increase. The reason is an upward bending of $E_{Fp,a}$ due to high recombination velocities $S_{p,if} \gtrsim 10^{4}$ cm·s$^{-1}$, enhancing the depletion of holes at the interface. Thus, the recombination current over IF-states with high recombination velocities is also triggered by the transport of holes to the surface, which is neglected by assuming flat quasi-Fermi levels within the SCR. Hence, at given forward bias $\Phi^{p}_{if,a}$ in the simulation is higher than its calculated counterpart with equations 2.73 and 2.74, explaining higher $V_{OC}$ values with higher $N_{d,if}$ in simulations.

In Figure 13 $J_{0,if}(V_{OC})$ and $A_{if}(V_{OC})$ of the recombination current density over IF-states and characteristic J-V-parameter of the default device have been simulated for varying acceptor and donor type defect properties at the interface. The device parameters are given in Table A - 4. Consistent with equation 2.76 for donor type interface states the values of $A_{if}$ are nearly constant over the complete range of defect densities in column a) and hole capture cross-sections (due to $p_{if,a} << n_{if,a}$) in column c) of Figure 13. At higher defect densities and capture cross-sections the A-factor increases slightly due to the upward bending of $E_{Fp,a}$ arising at $N_{d,if} \approx 10^{11}$ cm$^{-2}$ or $\sigma_p/\sigma_n \approx 10^{-3}$.

For a straightforward interpretation of simulated results in Figure 13 the absorber bulk defect was omitted to exclude recombination within the depletion region of the absorber. Also recombination of minority charge carriers at the metal contacts has been supressed. Accordingly, dominating interface recombination (under $V_{OC}$) can be assumed for donor type interface states when $S_{p,if} >> D_{n,a}/L_{n,a} = (D_{n,a}/\tau_{n,rad})^{1/2}$ is fulfilled. In Figure 12 a) ($S_{n0,bulk} = D_{n,a}/L_{n,a}$) and Figure 13 column a) the condition $S_{p,if} = D_{n,a}/L_{n,a}$ is reached for $N_{d,if} \approx 3\cdot10^{10}$ cm$^{-2}$. With $N_{d,if} = 10^{11}$ cm$^{-2}$ in column c) of Figure 13 $S_{p,if} = D_{n,a}/L_{n,a}$ is reached for an hole capture cross-section of $\sigma_p \approx 3\cdot10^{-16}$ cm$^{2}$ or $\sigma_p/\sigma_n \approx 3\cdot10^{-4}$. On the left of $S_{p,if} = D_{n,a}/L_{n,a}$ dominating bulk recombination can be considered, on the right dominating interface recombination.

In contrast to a constant $A_{if}(V_{OC})$ in column a) and c) of Figure 13 the other J-V parameters are strongly affected by the defect density $N_{d,if}$ and hole capture cross-section $\sigma_p$ of interface donor states. The saturation current density $J_{0,if}(V_{OC})$ plotted on a double logarithmic scale in column a) and c) reveals a power law. Fitting $J_{0,if}$ over the complete $N_{d,if}$ range as well as for

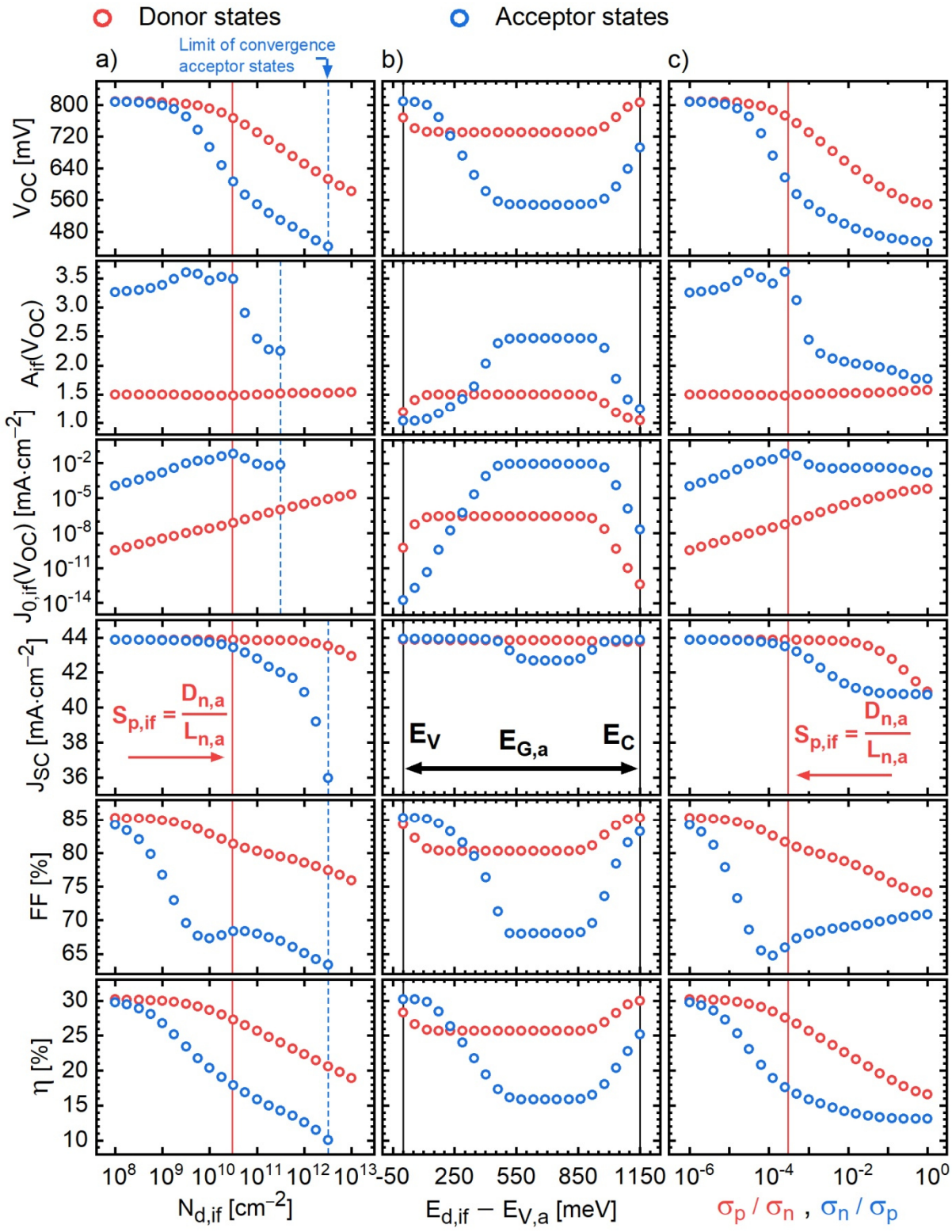


**Figure 13** Simulated J-V-parameter to investigate the impact of donor and acceptor type defects located at the absorber/buffer interface on the device performance of the default model given in Table A - 4. To keep the model simple the recombination level within the absorber bulk was removed, as well recombination of minority charge carriers at the metal contacts was eliminated. Column a) depicts the J-V-characteristics as a function of the acceptor/donor density $N_{d,if}$ at the absorber/buffer interface, the other trap parameter were fixed to the values in Table A - 4. The impact of the energy level is shown in column b). Collumn c) illustrates the effect of the hole capture cross section $\sigma_{p,if}$ (normalized to $\sigma_n = 10^{-12}$ cm$^2$) in the case of donor type defects and vice versa the electron capture cross section in the case of acceptor states.

$\sigma_p/\sigma_n < 0.1$ in both cases an exponent of 0.97 can be obtained. This confirms equation 2.77 where $J_{0,if} \propto S_{p,if} \propto \sigma_p \cdot N_{d,if}$ . However, for large $\sigma_p$ the exponent reduces, explained by a less limitation of the interface recombination current density via holes $S_{n,if}n_{if,a} >> S_{p,if}p_{if,a} \rightarrow S_{n,if}n_{if,a} \gtrsim S_{p,if}p_{if,a}$.

For high $N_{d,if}$ even $J_{SC}$ is declining in column a) in spite of a large hole barrier $\Phi^{p}_{if,a}(0)$ at the inverted interface under V = 0 V. The same effect can be observed for large hole capture cross-sections in column (c). $J_{SC}$ starts to decline for the ratio $\sigma_p/\sigma_n \approx 10^{-2}$ with $\sigma_n$ fixed to $10^{-12}$ cm$^2$. For $\sigma_p/\sigma_n = 1$ the approximation of completely occupied trap states with $\gamma_{D,if}(V_{OC}) \approx 0.002$ is still valid. This is not fulfilled anymore when the trap level moves closer to the conduction band like in column (b) of Figure 13. A defect level of $E_{d,if} - E_{V,a} = 0.8$ eV gives $\gamma_{D,if}(V_{OC}) \approx 0.002$ too, at $E_{d,if} - E_{V,a} = 1$ eV the occupation density under $V_{OC}$ reduces to $\approx$ 50%, giving $\gamma_{D,if}(V_{OC}) \approx 0.5$, affecting the potential curve within the SCR. Hence, compared to the demarcation level at the valence band $V_{OC}$, FF, and $\eta$ are increased after passing the demarcation level at the conduction band.

*Acceptor type interface states:*

As emerging from Figure 13 the circumstances of dominating interface recombination change dramatically if the IF-states become acceptors. In that case the proportionalities found in equations 2.76 and 2.77 are not applicable anymore over the complete ranges of $N_{d,if}$ and $\sigma_n/\sigma_p$ in column a), respectively c). Since, for acceptor like IF-states in a p-n$^-$-n-n$^+$-structure with a type inversion of the absorber at the interface it is highly probable that additional negative charged interface states alter the potential curve of the SCR, reducing the strength of type inversion at the interface. Hence, the depletion width of the absorber, as derived in equation 2.16, is modified by an additional length $w^*_{if}$ arising from charged interface states.

$$w_a = \left(\vartheta w^*_{if} + \delta d_b\right)\left(\sqrt{1 + \frac{1}{\vartheta - 1} + \frac{\delta^2 d_b^2}{\left(\vartheta w^*_{if} + \delta d_b\right)^2}\left(\beta - \frac{1}{\vartheta - 1} + 2\vartheta\frac{\Delta\varphi_{SCR}(V)}{\varphi^*}\right)} - 1\right) \qquad \textbf{2.83}$$

The Greek symbols in equation 2.83 are equivalent to equations 2.17. The extension or reduction of $w_a$ by charged interface states with $w^*_{if}$ depends on the inverse doping density of the hr-window (i-ZnO) and results to

$$w_{if}^{*} = +\gamma_{A,if}\frac{\varepsilon_a N_{d,if}}{\varepsilon_{hrw} N_{D,hrw}} \qquad \left(= -\gamma_{D,if}\frac{\varepsilon_a N_{d,if}}{\varepsilon_{hrw} N_{D,hrw}}\right). \qquad \textbf{2.84}$$

A negative $w_{if}^{*}$ indicates an addition (Donors) and a positive $w_{if}^{*}$ indicates a subtraction (Acceptors) to the depletion width $w_a$ of the absorber. In the case of very small $N_{d,if}$ or $\sigma_n$ giving $\gamma_{A,if} \approx 0$ it follows $w_{if}^{*} \approx 0$, thus equation 2.83 can be transferred into the solution without charged IF-states given with equation 2.16. For donor IF-states equations 2.83 and 2.84 hold as long as the buffer layer can be assumed to be completely depleted.

Another important consideration is the severe dependence of $w_{if}^{*}$ on illumination and voltage biasing. Resulting from equation 2.70 it is $\gamma_{A,if}(V) \approx (S_{n,if}n_{if,a})/(S_{n,if}n_{if,a} + S_{p,if}p_{if,a})$ in the case of $E_{d,if} \approx E_{g,a}/2$. Since $S_{n,if} << S_{p,if}$ for acceptor states the condition $S_{n,if}n_{if,a} >> S_{p,if}p_{if,a}$ for donor states, giving $\gamma_{D,if}(V) \approx 1$ for $V = V_{OC}$, is not valid anymore in spite of an inverted interface $n_{if,a} >> p_{if,a}$. Thus, the ionization of acceptor-like IF-states is defined by both $n_{if,a}$ and $p_{if,a}$. In this case the formula of the potential $\varphi_{if,a}(V)$ at the interface becomes an implicit equation. In the same way the recombination rate $U_{SRH,if}(V)$ given in equation 2.66 can not be reduced to one charge carrier concentration. Accordingly, for a defect level located on midgap equation 2.66 can be modified to

$$U_{SRH,if}(V) \approx \frac{S_{n,if}n_{if,a}S_{p,if}p_{if,a}}{S_{n,if}n_{if,a} + S_{p,if}p_{if,a}}, \qquad \textbf{2.85}$$

which impedes the comparison of coefficients as performed in equations 2.72 – 2.78 to estimate i.e. the diode quality factor.

Nevertheless, in order to evaluate the impact of charged IF-states on the recombination current and henceforward on the activation energy a case differentiation can be applied by assuming 3 different scenarios with (1) $S_{n,if}n_{if,a} << S_{p,if}p_{if,a}$ for either less inversion or possibly realized by $\sigma_n << \sigma_p$ ; (2) $S_{n,if}n_{if,a} >> S_{p,if}p_{if,a}$ for strong inversion and/or large electron capture cross sections $\sigma_n \approx \sigma_p$ ; as well as (3) $S_{n,if}n_{if,a} \approx S_{p,if}p_{if,a}$ for less inversion and/or $\sigma_n \lesssim \sigma_p$.

*(1) $S_{n,if}n_{if,a} << S_{p,if}p_{if,a}$:*

In this limit the occupation (= degree of ionization) of the interface states can be approximated to $\gamma_{A,if}(V) \approx 0 = \text{const.}$ for $V \leq V_{OC}$. This condition corresponds to the previously investigated case of completely occupied donor states, with the difference that

henceforward electrons $n_{if,a}$ are limiting the recombination current. Following the procedure as applied to donor type interface states the parameters A, $J_0$ and $E_A$ are derived as follows

$$A = \left(1 - \vartheta + \vartheta \Big/ \sqrt{1 + \beta + \frac{2\vartheta \cdot \Delta\varphi_{SCR}(V_{OC})}{\varphi^*}}\right)^{-1} \quad \textbf{2.86}$$

$$J_0 = qS_{n,if}N_{C,b}\left(\frac{N_{A,a}}{N_{V,a}}\right)^{\vartheta-1}\left(\frac{N_{D,hrw}}{N_{C,lrw}}\right)^{\vartheta} exp\{-2\vartheta\} exp\left\{-(k_BT)^{-1}\left((1-\vartheta)E_{g,a}\right.\right.$$
$$\left.\left. - q\varphi^*\left(1 + \frac{\beta}{2} - \sqrt{1 + \beta + \frac{2\vartheta \cdot \Delta\varphi_{SCR}(V_{OC})}{\varphi^*}}\right) + qV_{OC}\vartheta \Big/ \sqrt{1 + \beta + \frac{2\vartheta \cdot \Delta\varphi_{SCR}(V_{OC})}{\varphi^*}}\right)\right\} \quad \textbf{2.87}$$

$$E_A = E_{g,a} - \frac{\frac{q^2 d_b^2 N_{D,b}^2}{2}\left(\varepsilon_{hrw}N_{D,hrw} - \varepsilon_b N_{D,b}\right)}{\varepsilon_a N_{A,a}\left(2\varepsilon_{hrw}N_{D,hrw} - \varepsilon_b N_{D,b} + 2\sqrt{\varepsilon_{hrw}N_{D,hrw} \cdot \left(\varepsilon_{hrw}N_{D,hrw} - \varepsilon_b N_{D,b}\right)}\right)}. \quad \textbf{2.88}$$

In turn all quantities of the recombination current density are not being functions of the IF-defect properties, except $S_{n,if} \propto \sigma_n N_{d,if}$. This is approximately confirmed for $A_{if}$ and $J_{0,if}$ in column c) of Figure 13 for $\sigma_n/\sigma_p \leq 3 \cdot 10^{-4}$. In this range the degree of ionization is found to be $\gamma_{A,if}(V_{OC}) \approx 0$. However due to the positive off-set in the conduction band between absorber and buffer layer instead to be constant $A_{if}$ increases slightly from ≈ 3.3 to ≈ 3.6 and instead of $J_{0,if} \propto \sigma_n$ a power law with $J_{0,if} \propto \sigma_n^{1.17}$ is found. If $\sigma_n/\sigma_p$ exceeds $3 \cdot 10^{-4}$ the parameters $A_{if}$ and $J_{0,if}$ start to decrease due to the increasing $\gamma_{A,if}(V_{OC})$, which is not reflected by the other J-V-parameters like $V_{OC}$, since $J_{0,if}$ and $A_{if}$ are functions of $V_{OC}$ itself. However $\gamma_{A,if}(V_{OC}) > 0$ is not in accordance with case (1). A similarity appears by comparing the progressions of $A_{if}$ and $J_{0,if}$ in column a) and column c) of Figure 13. For small $N_{d,if}$ it was considered from equation 2.84 that $w_{if}^* \approx 0$. Hence, due to $\sigma_n/\sigma_p = 10^{-3}$, giving $S_{n,if}n_{if,a} < S_{p,if}p_{if,a}$ under $V_{OC}$ equations 2.86 and 2.87 are also applicable to $N_{d,if} \leq 3 \cdot 10^{10}$ cm$^{-2}$. In column a) the deviations of $J_{0,if}$ and $A_{if}$ to the theory are in the same order as in column c), which is again a result of the conduction band off-set, impacting the potential curve within the SCR.

The activation energy in equation 2.88 corresponds to the band gap energy of the absorber modified by a reduction term. This expression amounts to ≈ $6 \cdot 10^{-5}$ eV, using the values of the default model provided in Table A - 4. Therefore, it is quite fair to estimate $E_A \approx E_{g,a}$ in the case of completely unoccupied acceptor states at the interface.

*(2) $S_{n,if}n_{if,a} >> S_{p,if}p_{if,a}$:*

Situation (2) with $S_{n,if}n_{if,a} >> S_{p,if}p_{if,a}$ at $V_{OC}$ will give $\gamma_{A,if}(V_{OC}) \approx 1$ = const. and results in the other extremum of completely charged IF-states.

$$A = \left( \vartheta - \vartheta \Big/ \sqrt{1 + \frac{1}{\vartheta - 1} + \frac{1}{(\nu+1)^2}\left(\beta - \frac{1}{\vartheta - 1} + 2\vartheta \frac{\Delta\varphi_{SCR}(V_{OC})}{\varphi^*}\right)} \right)^{-1} \quad \textbf{2.89}$$

$$\begin{aligned} J_0 = {} & qS_{p,if}N_{A,a}\left(\frac{N_{V,a}N_{C,lrw}}{N_{A,a}N_{D,iw}}\right)^{\vartheta} exp\{2\vartheta\} exp\left\{-(k_BT)^{-1}\left[\vartheta E_{g,a}\right.\right. \\ & + q\varphi^*\left((\nu+1)^2 + \frac{\beta}{2} + \frac{(\nu+1)^2 - 1}{2(\vartheta - 1)}\right) \\ & - q\varphi^*(\nu+1)^2\sqrt{1 + \frac{1}{\vartheta - 1} + \frac{1}{(\nu+1)^2}\left(\beta - \frac{1}{\vartheta - 1} + 2\vartheta\frac{\Delta\varphi_{SCR}(V_{OC})}{\varphi^*}\right)} \\ & \left.\left. - qV_{OC}\,\vartheta \Big/ \sqrt{1 + \frac{1}{\vartheta - 1} + \frac{1}{(\nu+1)^2}\left(\beta - \frac{1}{\vartheta - 1} + 2\vartheta\frac{\Delta\varphi_{SCR}(V_{OC})}{\varphi^*}\right)}\right]\right\} \end{aligned} \quad \textbf{2.90}$$

$$E_A = E_{g,a} + \frac{q^2 d_b^2 N_{D,b}^2}{2}\left(\frac{1}{\varepsilon_b N_{D,b}}\left(1 - \frac{2N_{d,if}}{N_{D,b}d_b}\right) - \frac{1}{\varepsilon_{hrw}N_{D,hrw}}\left(1 - \frac{N_{d,if}}{N_{D,b}d_b}\right)^2\right). \quad \textbf{2.91}$$

In equations 2.89, 2.90 the variable $\nu = \vartheta w_{if}^*/\delta d_b$ was introduced for the sake of a better overview. In equation 2.91 the activation energy $E_A$ is a function of the density $N_{d,if}$ of IF-states. For low defect densities $N_{d,if} << N_{D,b}d_b = 5\cdot10^9$ cm$^{-2}$ the activation energy correspond to the found $E_A$ in equation 2.81 for donor IF-states. Reaching those low defect densities the J-V characteristics of the device will no longer dominated by IF-recombination (see Figure 13). However, there is a critical defect density $N_{d,if}^{crit}$ at the interface, from where on the second term in equation 2.91 reduces $E_A$ to lower values than the band gap energy.

$$N_{d,if}^{crit} = N_{D,b}d_b - \frac{\varepsilon_{hrw}}{\varepsilon_b}N_{D,hrw}d_b + d_b\sqrt{\frac{\varepsilon_{hrw}^2}{\varepsilon_b^2}N_{D,hrw}^2 - \frac{\varepsilon_{hrw}}{\varepsilon_b}N_{D,b}N_{D,hrw}} \quad \textbf{2.92}$$

In the case of the default model in Table A - 4 the critical density of IF-states amounts to $N_{d,if}^{crit} \approx 2.5\cdot10^9$ cm$^{-2}$.

Provided that $E_{d,if} - E_V = E_{g,a}/2 = 0.575$ eV and $N_{d,if} = 10^{11}$ cm$^{-2}$, to arrive at scenario (2) with $\gamma_{A,if}(V_{OC}) \approx 1$ the capture cross sections of $N_{d,if}$ have to be set equal to each other. With $\sigma_n = \sigma_p = 10^{-12}$ cm$^2$ following equation 2.91 the activation energy results to $E_A \approx E_{g,a} - 0.09$ eV = 1.06 eV.

*(3) $S_{n,if}n_{if,a} \approx S_{p,if}p_{if,a}$:*

By replacing $S_{n,if}n_{if,a}$ with $S_{p,if}p_{if,a}$ in equations 2.70 and 2.85 it is straight forward that the degree of ionization becomes $\gamma_{A,if}(V_{OC}) \approx 0.5$ and the recombination current equivalent to equation 2.72 is divided by a factor of 2. Thus, with some simple deliberations the saturation current density itself as well as the variable ν in equations 2.89 and 2.90 are multiplied by a factor of 0.5. Consequently ½ $N_{d,if}$ can be directly inserted into equation 2.91 giving an activation energy reduced by 43 meV compared to the band gap energy $E_{g,a}$ of the absorber.

# 3. Measurement techniques

On the basis of previous section 2.3, in the following a more profound view is given on the $V_{OC}$ methods for identifying the dominant region of recombination in solar cells. For device simulation in chapter 4.4 defect spectroscopy of solar cells is treated in more in detail.
To monitor the impact of ALE on the dynamics of minority charge carries within the absorber layer, time-resolved photoluminescence measurements (TRPL) were performed on bare CIGSe layers. A simple correlation between minority carrier lifetime and TRPL decay time is often not possible. Maiberg et al. give a comprehensive experimental and theoretical background to this method [29, 121, 162, 163],[Höl7],[Höl9]. Important for the TRPL measurement is the time correlated single photon counting (TCSPC) technique. Fundamentals about TCSPC can be found in references [164-168].
The effect of ALE on the surface morphology of bare CIGSe absorbers was investigated with X-ray photoelectron spectroscopy (XPS). Basics of this method are well explained in the literature [169], measurement details of this work are explained within the publication [Höl1] (see section 4.1). To obtain the CIGSe/CdS interface morphology of complete solar cells glow discharge optical emission spectroscopy (GDOES) was employed. An elaborate explanation of this technique is given in references [170-172].

## 3.1. Open circuit voltage ($V_{OC}$) measurements

### 3.1.1. $V_{OC}$ as a function of temperature

Plotting $V_{OC}(T)$ against temperature and extrapolating of $V_{OC}(T)$ to $V_{OC}(0\ K) = E_A$ by a linear fit (see Ref. [Höl1]) is an accredited method to obtain $E_A$ of $J_0$ [173-176]. As found in section 2.3 partially or completely dominating interface recombination can be concluded, if $V_{OC}(T)$ yields $E_A < E_{g,a}$. On the other hand if the $V_{OC}(T)$ measurement exhibits $E_A \cong E_{g,a}$ all recombination paths (QNR, SCR, IF) are possibly limiting the device performance. However, all of the measured activation energies in section 4 [Höl1],[Höl3] are increased by $\geq 30$ meV compared to $E_{g,a} = 1.15$ eV. From GDOES measurement and the deduced band diagram in Figure 5 it becomes obvious that $E_{g,a}$ at the interface can differ from process to process. This deviation amounts to a statistical error of $\pm$ 10 meV and is not responsible for the systematic shift of the activation energy with $E_A > E_{g,a}$. Another origin of this systematic shift is due to

the temperature dependence of the material parameters $N_V$ and $N_C$. But also the physical quantities such as $v_{th}$ and defect parameters such as $\sigma_{n,p}$ are temperature dependent. Thus, in contrast to the ideal activation energies derived in section 2.3, this section shows that $E_A(T)$ becomes a function of temperature too. Figure 14 a) shows linear fitted and extrapolated $V_{OC}(T)$-curves for different temperature ranges of interest. The data were obtained on the default device in Table A - 4, limited by radiative recombination. In that case $J_0$ is given with equations 2.32 and 2.33, reformulation with respect to the temperature dependencies yields

$$J_0(T) = J_{00} exp\left\{-\frac{E_A}{k_B T}\right\} = \frac{qN_{C,a}(T)N_{V,a}(T)}{N_{A,a}}\sqrt{\frac{D_{n,a}(T)}{\tau_{n,a}(T)}}\,exp\left\{-\frac{E_{g,a}}{k_B T}\right\}, \qquad \textbf{3.1}$$

disregarding the weak temperature dependency of the band gap energy [177, 178]. Further the dopants $N_{A,a}$ are assumed to be hydrogen like, fulfilling impurity exhaustion over the complete temperature range of interest.

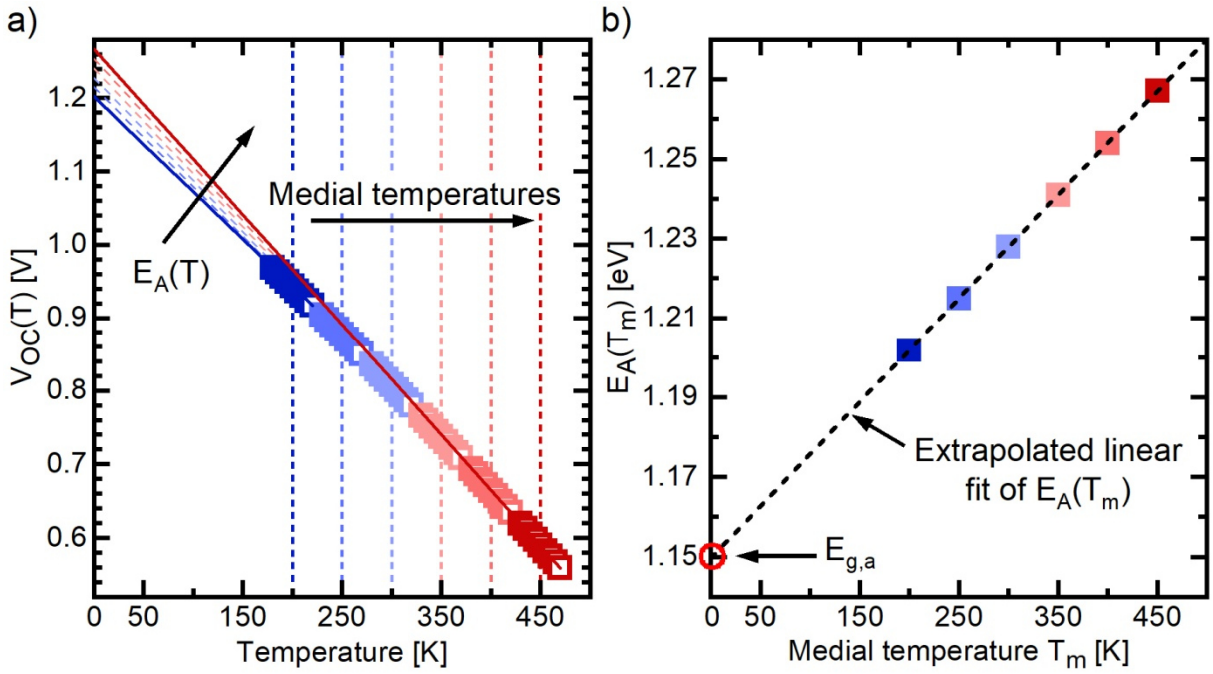


**Figure 14** (a) Simulated $V_{OC}(T)$ values by means of the radiative limited default model in Table A - 4. To generate the case of diffusion limited QNR recombination the temperature dependency of $\tau_{n,a}$ was adjusted to $T^{-1/2}$. Solid and dashed lines in (a) illustrate the extrapolated linear fit of $V_{OC}(T)$ for different medial temperatures specified by the colour code. (b) Derived activation energies $E_A$ from (a) plotted against the medial temperatures of the underlying temperature ranges, indicated by the colour code of the particular points.

Inserting equation 3.1 into 2.46 and extrapolating to 0 K yields in accordance to Figure 14 b) an activation energy as a linear function of temperature.

$$E_A(T_m) = E_{g,a} + k_B T_m \sum_i c_i \cdot \alpha_i \qquad \textbf{3.2}$$

Here $T_m$ corresponds to the medial temperature (see Figure 14) and $c_i \cdot \alpha_i$ to the temperature exponent of the particular physical quantity in equation 3.1. As shown in the previous sections the temperature exponents are related to $N_C \cdot N_V \propto T^3 \rightarrow c \cdot \alpha = 3$, $D_{n,a} \propto T^{-1/2} \rightarrow c \cdot \alpha = -\frac{1}{2} \cdot 1/2$ and for the radiative lifetime $\tau_{n,a} \propto B^{-1} \propto T^{3/2} \rightarrow c \cdot \alpha = -\frac{1}{2} \cdot 3/2$ [152]. Thus, at each medial temperature the activation energy is increased by $+ 2k_B T_m$, if radiative recombination is dominant. However for a polycrystalline solar cell, as it is de facto the case for CIGSe, QNR recombination possibly takes place by non-radiative recombination at grain boundaries. An important role during this process plays the transport of minority charge carriers via diffusion to the grain boundaries. In this regard, the temperature dependency of $\tau_{n,a}$ equals to the temperature dependency of $D_{n,a} \propto T^{-1/2}$ and they will cancel out each other in equation 3.2. In that case, $E_A(T_m)$ is increased by $+ 3k_B T_m$ compared to $E_{g,a}$, merely because of the contribution by the effective density of states. However, this scenario cannot be simulated in 1 dimension. That's why, in order to derive the results in Figure 14 the simulation model for dominating QNR recombination is still limited by radiative recombination, but the temperature dependency of $\tau_{n,a}$ is set to $T^{-1/2}$.

An overview of $E_A(T_m)$ for the several regions of dominant recombination is depicted in Figure 15 a). The utilized model was again the default model in Table A - 4. To ensure that only one region of recombination is dominating the device all other recombination channels are suppressed during simulation i.e. by removing IF-states while simulating dominant SCR-recombination. Analogous to prevailing QNR-recombination, if the device is limited by SCR- or IF-recombination due to donors, $E_A(T_m)$ follows equally to equation 3.2 a linear trend with an extrapolated $E_A(0K) \approx E_{g,a}$. However, in both cases a higher $\sum c_i \cdot \alpha_i$ is obtained because of the additional contributions from the temperature dependency of the recombination rate over defects. Temperature relevant rate parameters are the capture cross sections and thermal velocities. For SCR-recombination it follows from $J_{SCR}(V)$ in equation 2.65 that $\sum c_i \cdot \alpha_i \approx 4.2$ ($A_{300K} \approx 1.4$, $E_{z,m} \propto V_{bi} \propto -k_B T$) and for IF-Donor recombination $\sum c_i \cdot \alpha_i \approx 4.5$ ($\vartheta \approx 1$) taking $J_0$ from equation 2.77.

If temperature dependent charges and defect related occupation probabilities are involved in $V_{OC}(T)$ measurements it becomes evident from Figure 15 a) that the extracted activation

energies do not follow the previous found rules anymore. A pronounced deviation of $E_A(T_m)$ can be observed for IF-Acceptor recombination. But especially at high temperatures ($T \gtrsim 360$ K) also $E_A(T_m)$ of SCR recombination begins to deviate from the linear solution in equation 3.2. Reasonable for this non-conformance is the temperature dependency of the diode ideality factor, changing continuously from $A \approx 1.4$ at 300 K to $A \approx 2$ at 460 K with the result that $\sum c_i \cdot \alpha_i$ becomes a function of temperature too.

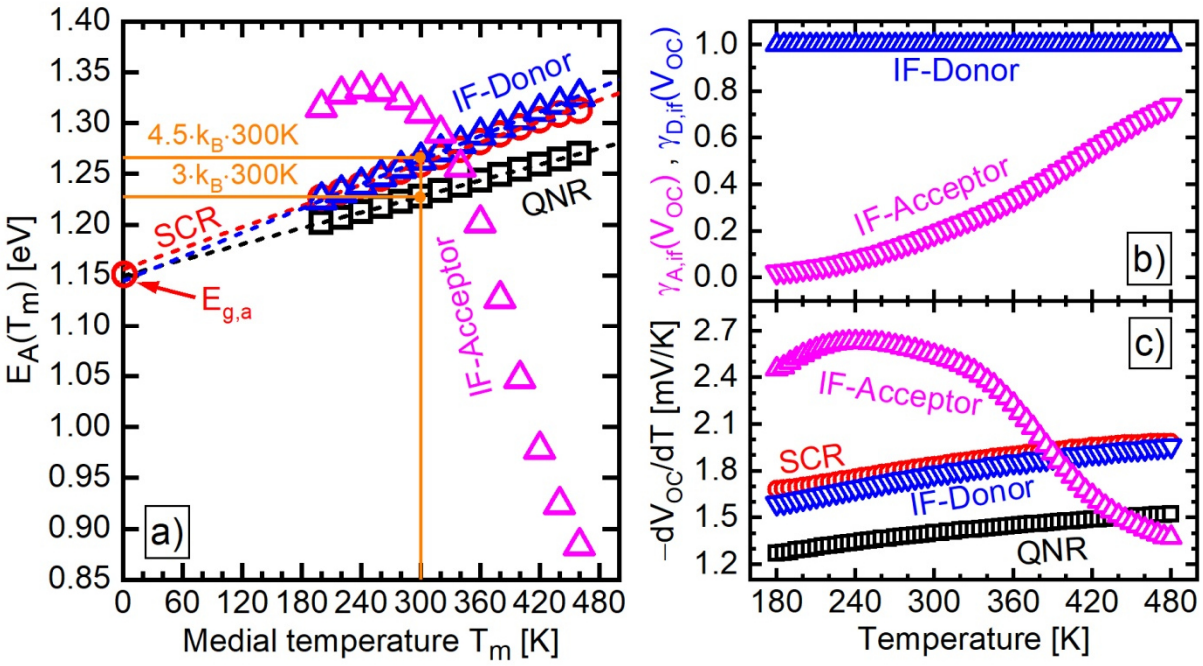


**Figure 15** (a) Activation energies as a function of medial temperatures for different dominating recombination paths, obtained on the default model in Table A - 4 by simulating $V_{OC}(T)$ and extrapolating the linear fit to 0K. (b) Electron occupation probabilities $\gamma_{A,if}(V_{OC})$ and $\gamma_{D,if}(V_{OC})$ dependent on temperature for acceptor, respectively donor type defect states at the interface. (c) Differential change of $V_{OC}$ with temperature subjected to several regions of recombination controlling the device characteristics.

In the case of IF-acceptor states the A-factor alone is no satisfying explanation for the non-conformance of $E_A(T_m)$ to the linear model in equation 3.2. It is furthermore the temperature dependent occupation probability $\gamma_{A,if}(V_{OC})$ shown in Figure 15 b) impacting the variation of $V_{OC}$ with temperature depicted by $-dV_{OC}/dT$ in Figure 15 c). Thus, comparing the curvature of $E_A(T_m)$ in Figure 15 a) and $-dV_{OC}/dT$ in Figure 15 c) it is visible that both following an equal trend. Two interwoven mechanisms are responsible for disturbing the estimation of $E_A$ from $V_{OC}(T)$ measurements for IF-acceptor states in Figure 15. The first mechanism is the change of charge carrier trap rates $S_{n,if}n_{if,a}$ and $S_{p,if}p_{if,a}$ illustrated by the temperature dependent occupation probability $\gamma_{A,if}(V_{OC})$ in Figure 15 b). With respect to section 2.3.3

($S_{n,if}n_{if,a} << S_{p,if}p_{if,a}$) at low temperatures ($T \lesssim 240$ K) the IF-recombination rate is due to $S_{n,if} << S_{p,if}$ practically restricted to electrons, giving $\gamma_{A,if}(V_{OC}) \approx 0$ despite $n_{if,a} > p_{if,a}$ (inversion at IF) under $V_{OC}$. Because of the limitation by majority charge carriers in the case of dominating recombination over IF-acceptor states the reduction of $V_{OC}$ with temperature is pronounced higher than of the other dominating recombination sites as shown by $-dV_{OC}/dT$ in Figure 15 c). A maximum of $-dV_{OC}/dT$ is found at $T \approx 240$ K, afterwards with increasing temperatures $-dV_{OC}/dT$ decreases initially slowly and after surpassing $T \approx 340$ K accelerated. This can be explained with the increasing trap occupation $\gamma_{A,if}(V_{OC})$ with higher temperatures. Increasing $\gamma_{A,if}(V_{OC})$ means that the recombination rate $S_{p,if}p_{if,a}$ under $V_{OC}$ decreases, reducing $-dV_{OC}/dT$. At $T \approx 410$ K, where $\gamma_{A,if}(V_{OC}) \gtrsim 0.5$ the recombination rate over IF-acceptor-states is limited by holes ($S_{n,if}n_{if,a} > S_{p,if}p_{if,a}$) and the reduction in $-dV_{OC}/dT$ decelerates. The second mechanism is the simultaneously scaling up of negative charges at the absorber surface due to the increasing $\gamma_{A,if}(V_{OC})$ with temperature, forcing $E_{Fn}$ closer to mid-gap. As a result, the electron barrier at the interface increases with temperature and counteracts to the thermal activated recombination process. Accordingly, the slope of the straight $V_{OC}(T)$ plots reduces as indicated by a reduction of $-dV_{OC}/dT$ in Figure 15 c) and equally $E_A(T_m)$ declines after reaching its maximum at $T_m \approx 240$ K. Beyond $T_m = 360$ K the linear extrapolation of $V_{OC}(T)$ to 0 K culminates to activation energies much lower than $E_{g,a}$. If the defect density increases with $N_{d,if} > 10^{11}$ cm$^{-2}$ or the trap level moves closer to the valence band with $E_{d,if} - E_{V,a} < 0.575$ eV the distribution of $E_A(T_m)$ in Figure 15 a) shifts to lower temperatures and $E_A < E_{g,a}$ becomes likewise possible at $T_m = 300$ K.

### 3.1.2. $V_{OC}$ as a function of time

The $V_{OC}(t)$-method utilizes the illumination triggered increase of $N_{A,a}$ due to the metastable behaviour of CIGSe absorbers as described in chapter 2.1.5. To avoid additional light enhanced modifications of the window layers the solar cells are illuminated with red light ($E_{h\cdot\nu} < E_{g,CdS}$). During the measurement the samples are active cooled from the backside and kept on 25°C (STC = standard testing conditions). The temperature and $V_{OC}$ are measured continuously in 1.5 second steps for 3 hours. An additional temperature correction is performed by measuring $\Delta V_{OC}/\Delta T$ in the vicinity of 25°C and recalculating each measurement point to 25°C.

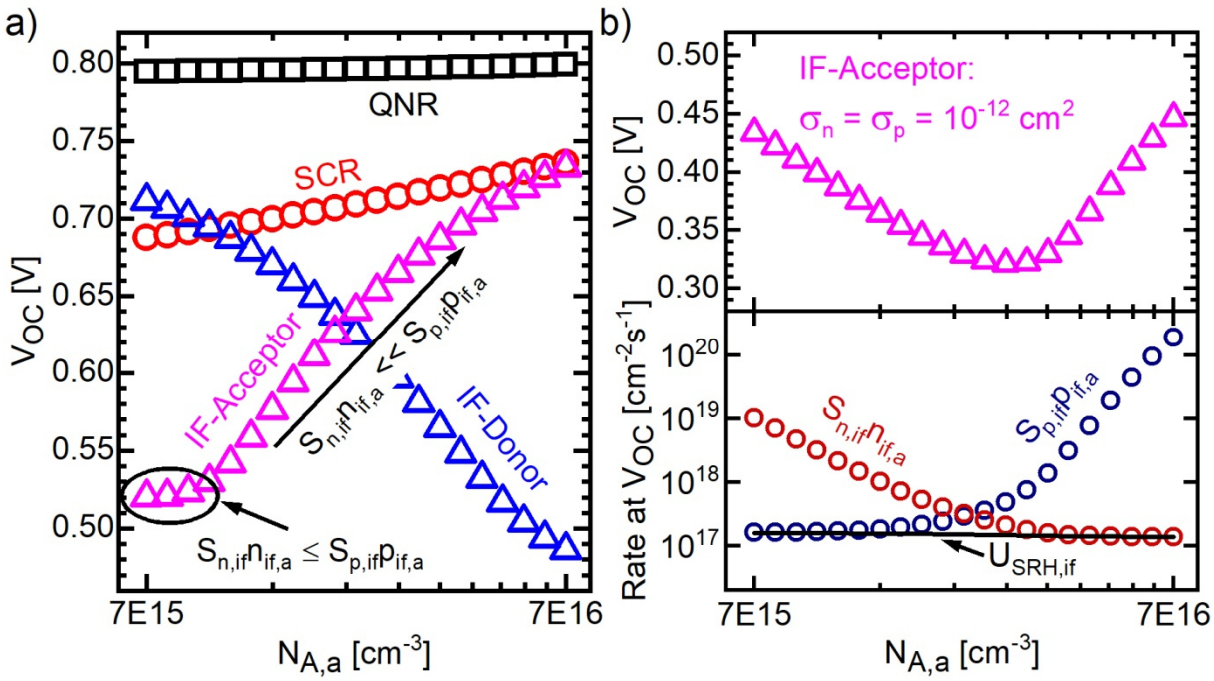


**Figure 16** a) Simulated open circuit voltage $V_{OC}$ as a function of the absorber doping density $N_{A,a}$ and the dominating region of recombination by modifying the default model in Table A - 4. Dominating SCR recombination was achieved by equal capture cross-sections of the bulk defect, analogous to the situation $\sigma_n/\sigma_p = 10^0$ in column d) of Figure 11. In the case of dominating recombination over IF-donor or acceptor states the capture cross-sections were asymmetric, resulting in $S_{n,if} = 10^3 \cdot S_{p,if}$ for donors and $S_{p,if} = 10^3 \cdot S_{n,if}$ for acceptors. b) $V_{OC}$ (top) and the recombination rate at $V_{OC}$ (bottom) as a function of the absorber doping for an acceptor type interface defect with equal capture cross sections.

Decisive for the determination of the dominant region of recombination is the slope trend of the $V_{OC}(t)$-transient. If recombination within the QNR of the absorber limits the device it can be deduced from equation 2.32 that with increasing $N_{A,a}$ the saturation current density $J_0$ declines. Thus, for dominating QNR recombination the $V_{OC}(t)$-transient should reveal an increasing trend with progressing illumination time. The identical behaviour exists for SCR recombination. With increasing $N_{A,a}$ the electric field $E_{z,m}$ in equation 2.65 scales up, causing a declining $J_0$ under the assumption that the A-factor remains nearly constant as illustrated in column a) of Figure 11. Hence, an ascending $V_{OC}(t)$-transient ($V_{OC}(t) \equiv V_{OC}(N_{A,a})$) as shown in Figure 16 a) is a strong indicator for dominating QNR as well as SCR recombination.

On the other hand, if the $V_{OC}(t)$-transient reveals a declining trend the existence of dominating interface recombination is highly probable. In the case of IF-donor states the recombination current density $J_{if}$ in equation 2.72 increases with $N_{A,a}$ due to a decreasing hole barrier $\Phi^p_{if,a}$ at the interface. This case is true as long as $S_{n,if}n_{if,a} >> S_{p,if}p_{if,a}$ with $\gamma_{D,if}(V_{OC}) \approx 1$ is valid. However, for IF-acceptor states the slope of the $V_{OC}(t)$-transient depends strongly on the

capture cross-sections of electrons and holes as well as the defect energy level, defining the dominating recombination rate $S_{n,if}n_{if,a}$ or $S_{p,if}p_{if,a}$ and with this the occupation probability. In Figure 16 a) compared to IF-donor states an opposed increasing trend for the $V_{OC}(t)$-transient under dominating IF-recombination with acceptor states is found. The reason for this opposite slope trend lies in the 3 orders of magnitude higher $S_{p,if}$ than $S_{n,if}$. As a result, despite $n_{if,a} > p_{if,a}$ (inversion), the recombination rate over IF-acceptor states is limited by $n_{if,a}$. With higher doping density $N_{A,a}$ the electron barrier $\Phi^{n}_{if,a}$ at the interface increases, enhancing $V_{OC}$. Accordingly, to obtain a decending $V_{OC}(t)$-transient the condition $S_{n,if}n_{if,a} >> S_{p,if}p_{if,a}$ has to become true, which would be the case for lower doping densities than the minimum $N_{A,a} = 7\cdot10^{15}$ cm$^{-3}$ in Figure 16 a). This is alternatively confirmed in Figure 16 b) by simulating $V_{OC}(N_{A,a}) \equiv V_{OC}(t)$ with equal capture cross-sections for electrons and holes ($\sigma_n = \sigma_p = 10^{-12}$ cm$^2$) of the IF-acceptor states (the remaining quantities of the simulation model have been kept constant). In this case the condition $S_{n,if}n_{if,a} >> S_{p,if}p_{if,a}$ is reached for $N_{A,a} \approx 7\cdot10^{15}$ cm$^{-3}$ and a decending trend of $V_{OC}(N_{A,a}) \equiv V_{OC}(t)$ is obtained. After surpassing $N_{A,a} \approx 10^{16}$ cm$^{-3}$ the recombination rate becomes limited by electrons with $S_{n,if}n_{if,a} < S_{p,if}p_{if,a}$ as depicted in the bottom graph of Figure 16 b). The minimum in $V_{OC}$ is reached until the interface recombination current density is solely limited by electrons ($U_{SRH,if} \approx S_{n,if}n_{if,a}$) and $V_{OC}(N_{A,a}) \equiv V_{OC}(t)$ begins to increase.

To summarize this section, for $V_{OC}(t)$-measurements it can be concluded that an increasing slope trend of $V_{OC}(t)$-transients allows no unambiguous determination or exclusion of dominant recombination sites within the solar cell. In this case additional methods like $V_{OC}(T)$-measurements or voltage dependend admittance spectroscopy have to be utilized. However, measuring a $V_{OC}(t)$-transient with a decreasing slope trend is a strong indicator for dominating recombination at the CIGSe/CdS interface.

## 3.2. Admittance spectroscopy

The response of a solar cell to a small AC test-signal delivers essential information about its electronic properties like doping densities or defect states within the band gap. Figure 17 sketches the simplified measurement circuit to determine the admittance or impedance of a solar cell from AC probing. Due to an auto balance bridge the n-side of the solar cell is set to zero potential (Virtual ground) with the high input resistance of the operational amplifier it follows $I_{ref} \cong I_x$.

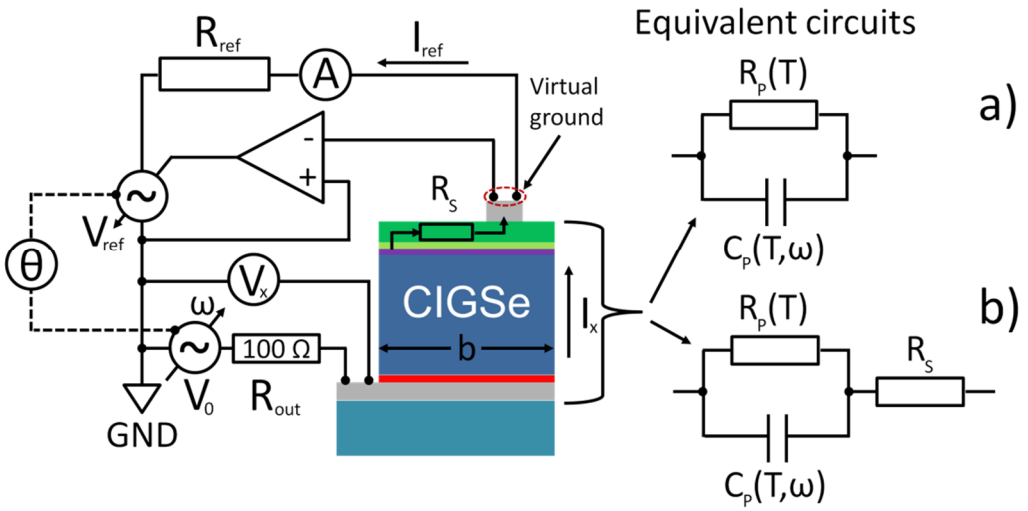


**Figure 17** Simplified measurement configuration of a solar cell during admittance spectroscopy. The equivalent circuits on the right hand side correspond to an ideal solar cell (a) without and (b) with a series resistance $R_S$ induced by the covered distance of the electrical current to the grid finger through the ZnO:Al layer. All other variables are explained within the text.

Because of $R_{ref}$, current $I_{ref}$ is in phase with $V_{ref}$ and the phase shift θ between $V_x$ and $I_x$ can be obtained by phase comparison of $V_0$ and $V_{ref}$. In this work an *Agilent E4980A* LCR-meter with an output resistance of $R_{out}$ = 100 Ω was used to test the samples. This setup employs equivalent circuit a) on the right hand side of Figure 17 to extract the test unit's (solar cell) capacitance $C_p$ and resistance $R_p$ analogous to equation 3.3 and 3.4.

$$\omega \cdot C_p = \frac{\frac{V_0}{V_x} - 1}{R_{out}} \cdot \sin\theta \qquad \textbf{3.3}$$

$$R_p = \frac{R_{out}}{\left(\frac{V_0}{V_x} - 1\right) \cdot \cos\theta} \qquad \textbf{3.4}$$

In equation 3.3 as well as 3.4, $V_0$ is the root mean square voltage of the test-signal and $V_x$ the voltage drop over the device, $R_{out}$ the output resistance of the LCR-meter and ω represents the angular frequency. By comparing the left and right side of equation 3.3 the high-pass property ($V_x \rightarrow 0$ for $\omega \rightarrow \infty$) of circuit a) in Figure 17 becomes visible.

The most considerable source of error of capacitance measurements is a resistance $R_s$ connected in series with the parallel circuit as shown by equivalent circuit b) in Figure 17. Reasons for an additional series resistance are manifold and of intrinsic or extrinsic character. Intrinsic, the predominantly resisting contribution acting as a series resistance is the sheet resistance of the AZO layer, denoted by $R_s$ in Figure 17. Extrinsic, the wire length and

electrical contacts may provide further series resistances. In particular electrical contacts can hold further capacitances in series, distorting the measured capacitance.

Firstly the role of a series resistance on the measured capacitance $C_{meas}$ is investigated. This is the case that equivalent circuit b) is the actually measured system state, but the measured data are analysed with equivalent circuit a). Via the complex admittances $\underline{Y}_p$ of the $R_p \| C_p$-element and $1/R_s$ for the series resistance, the complete complex admittance $\underline{Y}$ of circuit b) can be written as:

$$\underline{Y} = \left(\frac{1}{Y_p} + R_s\right)^{-1} = \left(\frac{1}{\frac{1}{R_p} + j\omega C_p} + R_s\right)^{-1}$$

$$= \frac{R_p + R_s + \left(\omega C_p\right)^2 R_s R_p^2}{\left(R_p + R_s\right)^2 + \left(\omega C_p\right)^2 R_s^2 R_p^2} + \frac{j\omega C_p}{\left(1 + \frac{R_s}{R_p}\right)^2 + \left(\omega C_p R_s\right)^2}. \quad \textbf{3.5}$$

Thus the measured values $C_{meas}$ and $R_{meas}$ after circuit a) in presence of a series resistance can be deduced by equations 3.6 - 3.8 with the result that both parameters become frequency dependent. For a sufficient small frequency ($\omega \ll 1/C_p R_s$) and series resistance ($R_s \ll R_p$), the measured capacitance can be determined to $C_{meas} \approx C_p$, however in the case of $\omega \to \infty$, $C_{meas} = 0$ is valid and independent from $R_s$.

$$\underline{Y}_{meas} = \frac{1}{R_{meas}} + j\omega C_{meas} \quad \textbf{3.6}$$

$$C_{meas} = \frac{Im\left(\underline{Y}_{meas}\right)}{\omega} = \frac{C_p}{\left(1 + \frac{R_s}{R_p}\right)^2 + \left(\omega C_p R_s\right)^2} \quad \textbf{3.7}$$

$$R_{meas} = \frac{1}{Re(Y_{meas})} = R_p \cdot \frac{\left(1 + \frac{R_s}{R_p}\right)^2 + \left(\omega C_p\right)^2 R_s^2}{1 + \frac{R_s}{R_p} + \left(\omega C_p\right)^2 R_s R_p} \quad \textbf{3.8}$$

The series resistance due to the lateral charge carrier transport through the window layer to the grid finger can be minimized by reducing the cell dimension b in Figure 17.

### 3.2.1. Equivalent circuit and Schottky barrier at the back contact

The bottom graph of Figure 18 depicts the band diagram of the default model from Table A - 4 equipped with a Schottky barrier formed at the back contact (BC). To keep the model

simple deep defects within the absorber are not regarded in this section and will be discussed in the next section 3.2.2. The barrier for majority charge carriers at the back contact can be treated analogous to the junction barrier at the front interface. Thus the equivalent circuit of a Schottky barrier can be described by a parallel connection of a resistor $R_{BC}$ and a capacitance $C_{BC}$. Further all other regions of the solar cell can be modelled likewise, resulting in the equivalent circuit shown in the upper part of Figure 18.

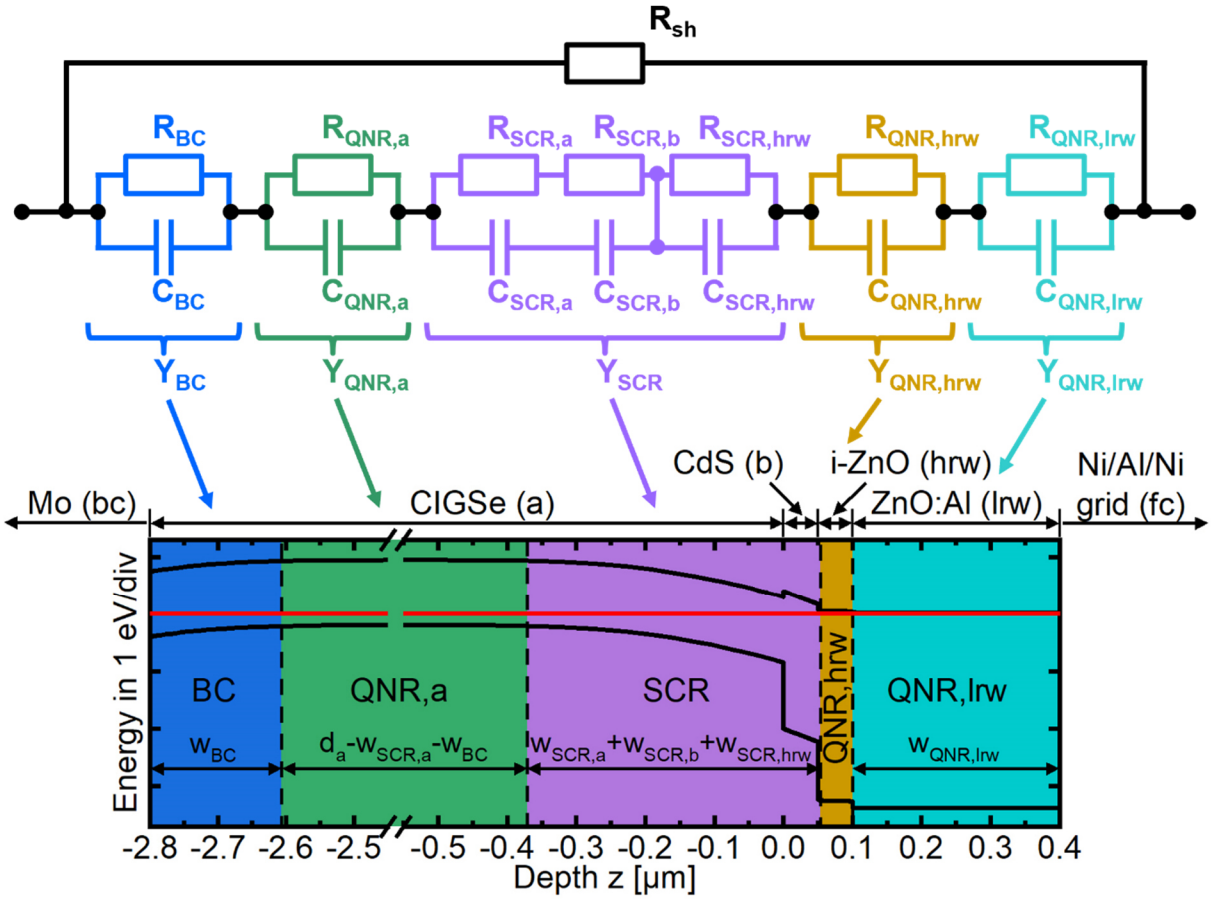


**Figure 18** Equilibrium band diagram (T = 300 K) and corresponding equivalent circuit regarding the majority charge carriers of the default device equipped with a Schottky barrier ($\Phi_{BC}$ = 0.4 eV) at the back contact (BC).

The resistors of the QNR regions i.e. $R_{QNR,a}$ are restricted to the majority charge carriers with

$$R_{QNR,a} = \frac{d_a - w_{SCR,a} - w_{BC}}{q\mu_{p,a}p_a} \qquad \textbf{3.9}$$

and the QNR capacitance $C_{QNR,a}$ follows analogous to the approach in equation 2.23 with

$$C_{QNR,a} = \frac{\varepsilon_a}{d_a - w_{SCR,a} - w_{BC}}. \qquad \textbf{3.10}$$

Both quantities [R] = Ω·cm$^2$ and [C] = nF·cm$^{-2}$ are related to the device area. In experiment the area is measured with a software tool by taking a picture of the cell and drawing a closed polygon along the cell edges. With the pixel number within the polygon and the pixel size the area becomes measureable. However there are several sources of error mainly (1) the fringed edges of the cell due to mechanical scribing, (2) the definition of the pixel size by means of an element with a known distance within the picture and (3) the aberration of the camera optics. An estimation of the area error revealed ≈ 5%, which can be taken directly as the error of the capacitance. Since the measurement of a reference circuit consisting of a 10 nF capacitor and 10 kΩ resistor connected in parallel exhibited an error of ≈ 0.1% in the frequency range from $10^2$ to $10^6$ Hz for the measured values by the LCR-meter.

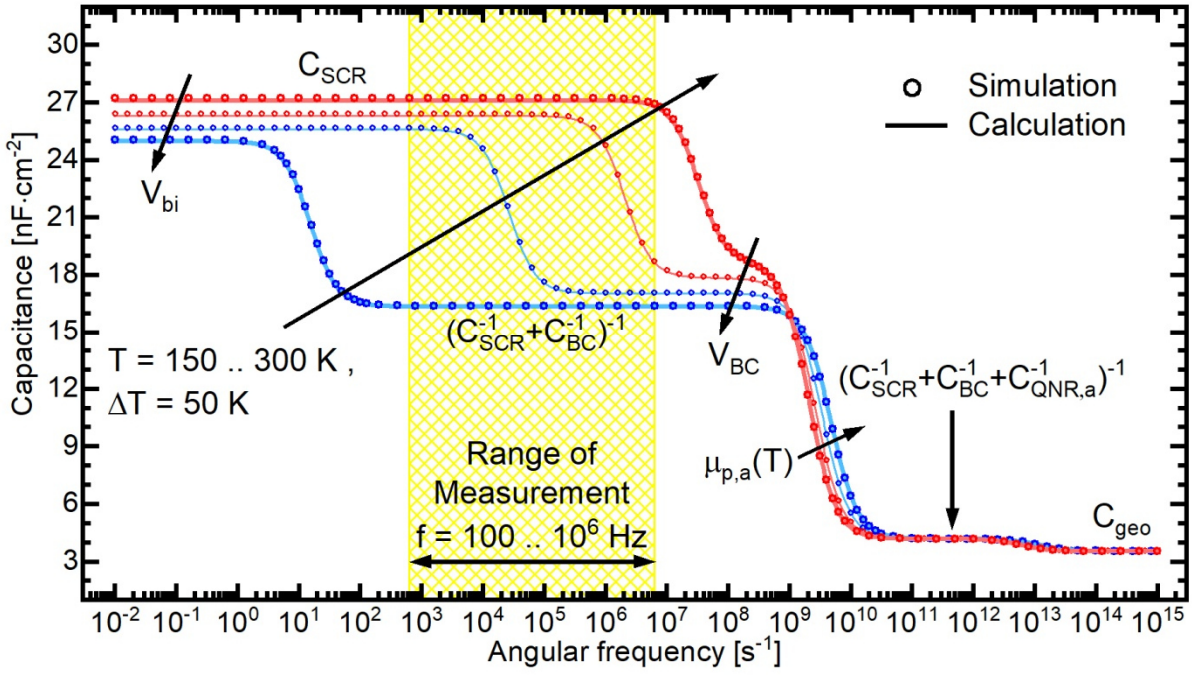


**Figure 19** Calculated (solid lines) and simulated (open circles) admittance spectra of the default model given in Table A - 4 as a function of temperature. For calculation the equivalent circuit in Figure 18 was utilized. To illustrate only the impact of a back contact barrier with $\Phi_{BC}$ = 0.4 eV defect levels within the absorber and at the interfaces were excluded.

Based on Figure 19, in the following it will be shown that for the interpretation of admittance measurements it is sufficient to utilize the imaginary part of $\underline{Y}_{meas}$ in the form of the capacitance. Plots of the capacitance over the logarithm of the angular frequency

(subsequently designated with C-f) and as a function of temperature are shown in Figure 19. C-f curves represented by solid lines in Figure 19 are calculated with the equivalent circuit depicted in Figure 18. The open circles in Figure 19 are obtained by numerical simulations. For both, simulations and calculations the input data were the physical quantities of the default model in Table A - 4. In addition the model is equipped with a transport barrier with $\Phi_{BC}$ = 0.4 eV for holes at the back contact as depicted in Figure 18. Figure 19 discloses a good match between simulated data by solving numerically the semiconductor equations and analytical data by calculating the equivalent circuit in Figure 18. The determination of the capacitance from calculations is conducted equally to the measurement case. Firstly, the complex admittance $\underline{Y}$ of the complete device can be calculated with

$$\underline{Y} = \frac{1}{R_{sh}} + \left( \frac{1}{\underline{Y}_{BC}} + \frac{1}{\underline{Y}_{QNR,a}} + \frac{1}{\underline{Y}_{SCR}} + \frac{1}{\underline{Y}_{QNR,hrw}} + \frac{1}{\underline{Y}_{QNR,lrw}} \right)^{-1}. \qquad \textbf{3.11}$$

Due to the negligible modification of the device admittance by the depletion or accumulation regions within the window layers, these admittances are not regarded in equation 3.11 and Figure 18. Subsequently, by applying equivalent circuit a) of Figure 17 on $\underline{Y}$ the capacitance can be obtained analogous to equation 3.7 with C = Im($\underline{Y}$)/ω. The capacitance curves in Figure 19 reveal 3 explicit steps in their progression. For the lowest temperature T = 150 K one will find 4 distinct plateaus indicated by $C_{SCR}$, $\left(C_{SCR}^{-1}+C_{BC}^{-1}\right)^{-1}$, $\left(C_{SCR}^{-1}+C_{BC}^{-1}+C_{QNR,a}^{-1}\right)^{-1}$, and $C_{geo}$. Because of $R_{SCR}$ representing the highest resistance within the device the capacitance converges to $C_{SCR}$ for low frequencies. $C_{SCR}$ was calculated with equation 2.22 and $R_{SCR}$ analogous to equation 2.25 by integrating the inverse conductance 1/σ(z) over the SCR. A weak temperature dependency can be found for $C_{SCR}$ due to the temperature dependency of $V_{bi}$ in accordance with equation 2.14. The 2nd capacitance plateau results from the hole barrier at the back contact. A strong temperature dependency is visible for the step from $C_{SCR}$ to $\left(C_{SCR}^{-1}+C_{BC}^{-1}\right)^{-1}$. This strong temperature dependency of the characteristic frequency $\omega_{BC}$ follows from the temperature activated resistance $\omega_{BC} \propto R_{BC}^{-1} \propto \exp\{-\Phi_{BC}/k_BT\}$. Accordingly, $\Phi_{BC}$ becomes experimentally available by an Arrhenius plot of $\ln(\omega_{BC}\cdot T)$ [Höl13]. For the calculated C-f curves in Figure 19 $R_{BC}$ was obtained by integrating 1/σ(z) from $z = -d_a$ to $z = -d_a + w_{BC}$. The capacitance of the depletion region at the back contact has been estimated with $C_{BC} = \varepsilon_a/w_{BC}$. Due to the weak temperature dependency of the built in voltages $V_{bi}$ and $V_{BC}$ the 2nd capacitance plateau reveals likewise a weak temperature dependency. In contrast, no temperature dependency can be observed for the 3rd and 4th capacitance plateau. Moreover, the 2nd and 3rd capacitance steps are a weak

function of temperature too. This weak temperature dependency originates from the weak temperature activated dielectric relaxation of the quasi-neutral regions with $QNR_a$ causing the 2nd capacitance step as well as $QNR_{hrw}$ and $QNR_{lrw}$ causing the 3rd capacitance step. From Figure 18 the capacitance of $QNR_a$ can be deduced to

$$C_{QNRa} = \frac{\varepsilon_a}{d_a - w_{SCR,a} - w_{BC}} \qquad \textbf{3.12}$$

and the resistance of $QNR_a$ is under the assumption of solely present hydrogen like acceptor states $N_{A,a}$ determined by

$$R_{QNRa} = \frac{d_a - w_{SCR,a} - w_{BC}}{q\mu_{p,a}N_{A,a}}. \qquad \textbf{3.13}$$

The characteristic frequency $\omega_{QNRa}$ of the dielectric relaxation of the absorber follows to

$$\omega_{QNRa} = \frac{1}{R_{QNRa}C_{QNRa}} = \frac{q\mu_{p,a}N_{A,a}}{\varepsilon_a}, \qquad \textbf{3.14}$$

giving the temperature dependency $\omega_{QNRa} \propto \mu_{p,a} \propto T^{-3/2}$. In the case that the doping density of the absorber is defined by less shallow acceptors with $E_{A,a}$ the temperature dependency of the characteristic frequency increases to $\omega_{QNRa} \propto \mu_{p,a}/\left(\exp\{(E_{A,a}\text{-}E_F)/k_BT\} + 1\right)$.

For thick absorber layers with $d_a >> d_b$ it can be shown that the 3rd capacitance plateau corresponds approximately to the geometrical capacitance $C_{geo,a}$ of the absorber.

$$C_{geo,a} \approx \left(C_{SCR}^{-1} + C_{BC}^{-1} + C_{QNR,a}^{-1}\right)^{-1} = \frac{\varepsilon_a\varepsilon_b}{\varepsilon_a d_b + \varepsilon_b d_a} \approx \frac{\varepsilon_a}{d_a} \qquad \textbf{3.15}$$

In equation 3.15 $C_{SCR}$ has been taken from equation 2.22 and $C_{QNR,a}$ from equation 3.12 the capacitance of the back contact barrier is $C_{BC} = \varepsilon_a/w_{BC}$.

The 4th capacitance plateau indicated with $C_{geo}$ in Figure 19 arises from the dielectric relaxation of the complete device. Due to the high doping density of the window layers the frequency range of $C_{geo}$ is close to the visible range of the electro-magnetic (EM) spectrum. For device modelling a doping density of $N_{D,lrw} \approx 2\cdot10^{18}$ cm$^{-3}$ has been chosen to keep the low-resistive window layer non-degenerated. However, in the case of realistic devices the lrw-layer is usually degenerated and it can be assumed that $C_{geo}$ will be obtained in the visible range of the EM spectrum. Thus, $C_{geo}$ is experimentally not observable even with LCR-meter operating with frequencies in the THz range. The frequency range of 100 Hz to 1 MHz used in this work for admittance spectroscopy is indicated by the yellow shaded box in Figure 19.

By varying the temperature the capacitance step of the back contact barrier passes through this frequency range and can be analyzed. Usually, signals in admittance spectroscopy originating from deep defects or transport barriers for the photo-current, which are crucial for solar cell operation possess high activation energies. Hence, these features are not observed in admittance spectroscopy due to low characteristic frequencies $f_0 < 100$ Hz even for high temperatures T > 300 K.

### 3.2.2. Volume and interface defects

In view of the capacitance contribution of a volume defect within the absorber, energetically located within the band gap, this case was comprehensive analysed by Walter et al. [106]. With the result that, if the defect level intersects or grazes the Fermi-level, usually within the depletion region of the absorber (see Figure 3 in Paper 4, section 4.4), and is able to be thermally emptied or occupied by electrons, then a contribution by the defect to the junction capacitance is observable. The origin of this capacitance contribution is a phase shift of the alternating current density induced by the defect related capture and emission process of charge carriers within the bands evoked by the alternating voltage. If the frequency of the alternating voltage reaches and exceeds the characteristic frequency $\omega_d$ of the changeability of defect occupation, the capacitance contribution by the defect to the junction capacitance becomes negligible. This condition is characterized by a step in the measured capacitance. As shown by virtue of an interface defect level in Figure 20 a), usually at the low frequency side of the capacitance step the measured capacitance corresponds to the sum $C_{SCR} + C_d$, with $C_d$ the capacitance contribution by the defect, then the high frequency side is determined by the junction capacitance $C_{SCR}$. This is true, if there are no other admittance modifications by further defects or transport barriers are existent. In the case of an acceptor like defect state centred at $E_d - E_V > E_F - E_V$ (QNR) with asymmetric capture cross-sections $\sigma_p >> \sigma_n$ and/or an intersection point with the Fermi-level at $z = -z_i > -w_a$ where $p_a(-z_i) >> n_a(-z_i)$, the characteristic frequency can be deduced from equation 2.69 as shown in Ref. [106] to

$$\omega_d = 2\sigma_p v_p p_0(-z_i) = 2\sigma_p v_p N_{V,a} exp\left\{-\frac{E_a}{k_B T}\right\}. \qquad \textbf{3.16}$$

At $z = -z_i$ the activation energy corresponds with $E_a = E_d - E_V$ (= $E_F - E_V$) to the defect energy level. The characteristic frequency $\omega_d$ in equation 3.16 represents the inflection point of the capacitance step. Hence, $\omega_d$ can be found straightforward by determining the local maximum

in the derivative $-\omega \cdot dC/d\omega$ of the measured capacitance frequency curves. The activation energy becomes determinable by an Arrhenius-plot of $\ln(\omega_d \cdot T^{-2})$ [179]. The multiplication with $T^{-2}$ within the logarithm is due to the temperature dependency of $v_p \propto T^{1/2}$ and $N_{V,a} \propto T^{3/2}$, the capture cross-section $\sigma_p$ is assumed to be temperature independent.

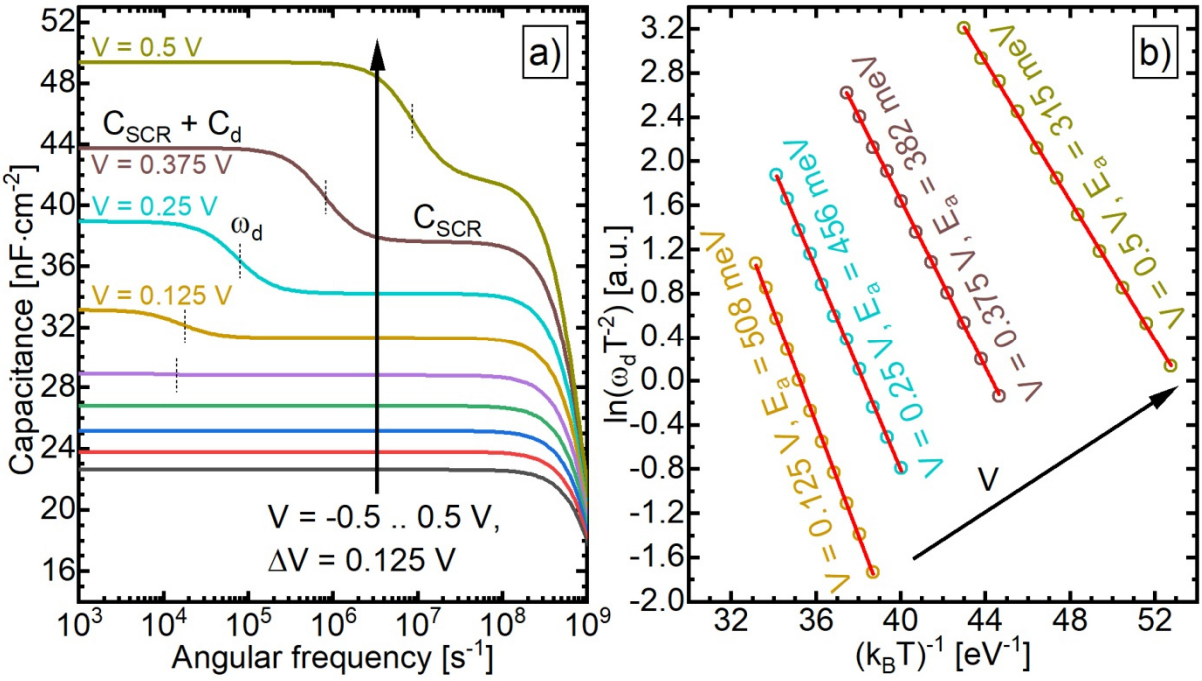


**Figure 20** (a) Capacitance frequency curves as a function of the applied bias voltage simulated by means of the default model in Table A - 4 with acceptor states at the CIGSe/CdS interface settled at a dicrete level of $E_d - E_V = E_g/2$. Simulations were performed under a constant temperature of T = 300 K. The dashed vertical lines are indicating the characteristic frequency $\omega_d$. (b) Arrhenius plots of the temperature corrected logarithm of the characteristic frequency $\ln(\omega_d T^{-2})$ for determining the activation energy $E_a$ as a function of the DC bias of the capacitance step shown at 300 K in (a).

As mentioned above, the intersection of defect and Fermi level is a prerequisite for determining the defect energy level from admittance spectroscopy. Further, at the intersection point the change of occupied defect states becomes maximally, giving the maximum possible capacitance contribution by the considered defect level [106]. With regard to spatially narrow defects, as it is the case for interface defects, the response of IF-states by AC-probing depends strongly on the position of the Fermi-level at the interface. This means in the case of an inverted absorber/buffer interface deep defects would not be observed in equilibrium admittance spectroscopy (completely occupied). This is visible in Figure 20 a) where for bias voltages in reverse direction up to V = 0 V no or a negligible capacitance step is observed. However, by applying a bias voltage in forward direction, a condition is created where the occupation of the interface defect level located on midgap of the absorber can be significantly

modified by the AC test signal. Then a contribution by this defect to the junction capacitance becomes available and with increasing forward bias the height of the capacitance step and concomitant the amplitude of the alternating occupation probability of the defect enhances.
In Figure 20 an energetically discrete distributed acceptor like ($\sigma_p = 10^3 \cdot \sigma_n$) defect state was utilized for simulating the voltage dependent capacitance contribution. After equation 3.16 for a bulk defect the obtained characteristic frequencies $\omega_d$ and the activation energy $E_a$ of the capacitance steps of this kind of defect are independent from the DC bias voltage. However, as shown in Figure 20 a) and b) for interface states both $\omega_d$ and $E_a$ are a function of the DC bias voltage. While $\omega_d$ increases, $E_a$ reduces with increasing forward bias. To obtain from measured voltage dependent admittance spectra the characteristic parameters of interface defects like energy level or capture-cross sections the modulated recombination current density $J_{if} = J_{if}(V_{DC}) + \tilde{J}_{if}$ over IF-states has to be derived. With equation 2.66 and $J_{if} = q \cdot (U_{SRH,if}(V_{DC}) + \tilde{U}_{SRH,if})$ the capacitance contribution by IF-states $C_d = \mathrm{Im}(\tilde{J}_{if})/\omega$ can be related to the defect parameters [106, 180, 181]. However, this requires the knowledge about the positions of the quasi-Fermi levels at the interface. Experimentally, these quantities are difficult to access and the modelling of voltage dependent admittance results by device simulations becomes mandatory for quantifying the defect properties of IF-states.

# 4. Experimental results and device simulation

The subject of this thesis is the understanding of optoelectronic effects in CIGSe semiconductors which occur under different environmental conditions, in particular exposure to air-light combinations. On the one hand it deals with the strategy to experimentally uncover the effects of air-light-exposure (ALE) on bare CIGSe absorber layers and complete solar cells. On the other hand, an electronic simulation model is proposed which describes the impact of ALE on the solar cell physics. The presentation of these studies takes place in the form of peer-reviewed publications [Höl1],[Höl2],[Höl3],[Höl4] in the following referred to by Paper 1, 2, 3, 4. Interpretations of the results in the stated articles are founded on the fundamentals in chapter 2 and the examinations of the measurement methods in chapter 3. Supporting information and considerations for the comprehensive understanding of the presented studies are given in the subsections of sections 4.1 - 4.4.

## 4.1. ALE induced surface modification

The first indications for ALE surface modification were obtained after long-term TRPL measurements on bare CIGSe layers in ambient air. The TRPL decay time at the end of a particular experiment performed at a particular location of the sample was significantly reduced with respect to the decay time measured at the beginning of the experiment. However by changing the location of excitation on the sample surface, the initial decay time was observed, in spite of identical air exposure. This underlined the role of light for the observed degradation process and culminated in the first publication identifying the ALE effect given in this section with Paper 1. The ALE effect in Paper 1 is named as WLS (white light soak) since at the time of publication the abbreviation ALE was not established. Accordingly, WLS (= ALE) denotes the exposure of bare CIGSe layers to the ambient atmosphere under illumination with 1 sun equivalent white light.

TRPL-measurements in Paper 1 show that the formerly known degradation of the minority charge carrier lifetime of CIGSe due to air-exposure accelerates under illumination. This adds on the one hand to the previous results of Metzger et al. [25, 40]. On the other hand, by applying for the first time XPS-measurements in connection with TRPL-measurements, Paper 1 combines this TRPL-lifetime degradation directly with a modification of the CIGSe surface chemistry. The important results from XPS-measurements are that (1) only the bonding

characteristics of Na, O, and Se are affected by ALE and (2) an accumulation of O and Na on the surface is caused by ALE.

Both methods, TRPL and (even more so) XPS, are sensitive to the surface. Thus, if ALE also affects the bulk region of the CIGSe layer is not determinable with these two methods. Therefore, in order to solve this problem, in Paper 1 complete solar cells were manufactured from CIGSe absorbers with different ALE times. Concomitant to the reducing TRPL-decay time of the bare CIGSe layers, $V_{OC}$ of the related solar cells monotonously decreases with increasing ALE time. That means the detrimental modification of the CIGSe absorber due to ALE persists throughout processing the buffer and window layers. This indicates that the dominant recombination region of the solar cell is the same as the dominant recombination region of the initial bare CIGSe layer. By determining the activation energy of the saturation current density from $V_{OC}(T)$ measurements in Paper 1, the dominant recombination mechanism of solar cells from ALE-treated absorber takes place at the interface. Hence, the reduction of TRPL-decay time due to ALE of bare CIGSe layer is referred to an increased recombination rate of minority charge carriers at the surface.

In conclusion the presented results in Paper 1 are firstly important for manufactures. But also for researchers who are investigating CIGSe absorber layers with charge carrier generating methods either directly in ambient air or after air exposure.

# Light induced degradation of $Cu(In,Ga)Se_2$ thin film surfaces

**T. Hölscher, S. Förster, T. Schneider, M. Maiberg, W. Widdra, and R. Scheer**

*Institute of Physics, Martin-Luther-University Halle-Wittenberg, 06120 Halle, Germany*

We investigate light-induced degradation of $Cu(In,Ga)Se_2$ (CIGSe) layers by means of time-resolved photoluminescence (TRPL) measurements. Illumination in the range of minutes with 1 sun white light equivalent leads to a strong reduction of the carrier lifetime as determined by TRPL. Ambient storage in the dark, however, does not cause degradation. X-ray photoelectron spectroscopy of the CIGSe surface reveals a light induced enhancement of Na 1s and O 1s core-level emission. The position of the O 1s peak at 531.6 eV is related to a Na-O-CIGSe bonding complex. The light-induced degradation of the CIGSe layer finally translates into inferior open circuit voltages due to the dominance of interface recombination in completed solar cell devices. This study has implications for laboratory research and may need to be regarded in CIGSe module production.

Link to original publication: http://dx.doi.org/10.1063/1.4992116

### 4.1.1. Supporting information and considerations of Paper 1

*Correction TRPL decay times*

In Paper 1 it was shown that illumination of bare CIGSe layers in ambient (humid) air causes a strong reduction of the decay time in TRPL-measurements. This leads to the assumption that a degradation of the minority charge carrier lifetime takes place during the application of the TRPL-method itself. Typical parameters for the laser-excitation in TRPL measurements are given in Table II of Paper 1 in this section. Therewith, the sample is exposed to an average laser light intensity of $\approx 10^{-3}$ $Wcm^{-2}$ (0.01 suns) for a measurement time of ≈ 30 s. With respect to Figure 1 of Paper 2 in the next section 4.2 this corresponds to an ALE light dose of 0.03 $Jcm^{-2}$ and implicates a reduction of the average decay time by 5 - 10% during the measurements in the as fabricated or 18 h storage state. That means it could be expected that the first two sets of decay constants in the inset of Figure 2 in Paper 1 deviate systematically to lower values compared to the "true" decay constants without illumination. After 1 min illumination with 1 sun equivalent white light, called white light soak (WLS), the reduction of decay time caused by the TRPL measurement itself becomes negligible, since the absolute light dose amounts to ≈ 6 $Jcm^{-2}$, which is located in the region where the reduction of decay time levels off for an intensity of $\approx 10^{-3}$ $Wcm^{-2}$ (see Figure 1 in Paper 2).

*Na-passivation in dry air*

Figure 2 of Paper 1 depicts elongated TRPL-transients of the investigated CIGSe layers after a storage period in dry air (+ $N_2$) and darkness. This observation is a general characteristic of CIGSe layers with Sodium doping. Usually, the maximum of the time constants is reached after ca. 10 h and stabilizes for 1 - 2 days, if the samples are remaining in darkness and dry air. In comparison with Figure 1 in Paper 1 the latter sample state serves as the starting point of the ALE experiments. In contrast, CIGSe layers without Na reveal no increase of decay times after similar or longer storage periods in dry air. This gives reasons that Sodium is involved in the process of passivation leading to increased decay constants after the exposure to dry air in darkness. The mechanism behind the passivation process may be related to a Na-catalyzed oxygenation of selenium vacancies as explained in section 2.1.3 and assumed in Paper 1.

*Experimental and method related ALE*

As shown in Figure 3 of Paper 1, keeping CIGSe layers in dry air or even high-vacuum without illumination is no guarantee against the reduction of TRPL decay times. Provided that the layers were exposed to ambient (humid) air, this give reasons that a participation of adsorbed or already reacted air components, preferable $H_2O$, are involved in the degradation process.

Further illumination in high-vacuum for 1 h reveals again a strong reduction of the TRPL decay time indicating a photo-catalyzed surface modification. However, the measured TRPL decay is definitively less fast than the decay measured after 10 min illumination in ambient air (compare Figure 2 and 3 in Paper 1). Thus, it is imaginable that the surface reaction is limited by the amount of physically or chemically adsorbed $H_2O$ on the surface. In contrast, the ambient atmosphere constitutes an infinite source of $H_2O$ and the surface reaction proceeds uninhibited, resulting in a stronger reduction of TRPL decay time after a shorter illumination period. Further, exposure to X-rays in ultra high-vacuum causes a similar strong decrease in TRPL time constants, which indicates the involvement of excited charge carriers, presumable electrons, in the detrimental surface reaction. In XPS-measurements this may produce an error due to the method itself especially in the case of non-ALE layers exposed to ambient (humid) air in darkness, serving as the reference.

By comparing the TRPL decay time reduction under high-vacuum in Figure 3 of Paper 1 the participation of excited electrons during ALE reaction becomes equally evident. Thus, after 3 days storage in darkness (thermal excitation) the time constants decrease much less than after 1 h illumination (photon excitation).

*Chemistry of AE and ALE*

Three distinct differences in the surface chemistry of ALE compared to non-ALE CIGSe layers can be observed in Figure 4 of Paper 1 with (1) a segregation of Na and O at the very surface, (2) a shift of the O 1s and Na 1s XPS peaks to lower binding energies, and (3) an rising signal of the Se - O bonding. Observation (1) in combination with (3) implies that a bonding complex consisting of O, Na (as found by Heske et al. [46]), and maybe of Se is formed. In spite of this the role of Na during ALE and AE is not straightforward. It is shown by Heske et al. [46] that the adsorption of $H_2O$ takes place at Na bonding sites. Thus, in the case of accumulated Na at the CIGSe surface the Na 1s peak is centred at a binding energy of $E_b \approx 1073.0$ eV. After adsorption of $H_2O$ a shift of the Na 1s peak to a lower binding energy of $E_b \approx 1072.3$ eV is observed in [46]. An identical binding energy of $E_b \approx 1072.2$ eV is found

for the non-illuminated AE sample in Figure 4 of Paper 1, leading to the assumption that Na at the surface of the AE sample is mostly involved in the $H_2O$ adsorption. Further, it can be shown in [46] after desorption of $H_2O$ the Na 1s peak shifts back to the former higher binding energy of $E_b \approx 1073.0$ eV of the clean surface. A reduced intensity of the Na 1s peak after $H_2O$ desorption indicates a Na desorption as well [46].

It is suggested by Heske et al. [45] that the binding type of accumulated Na on the free surface is of enhanced metallic character. In Figure 21 it can be shown that upon $H_2O$ adsorption, the Na 1s binding energy and the kinetic energy of the Na $KL_{23}L_{23}$ Auger signal are shifted to lower values – indicating a Na bonding state of enhanced ionic character [45, 46]. Further, Figure 21 demonstrates identical Auger parameter of Na for surfaces exposed to ambient air without illumination (AE no light) from Paper 1 and surfaces with adsorbed $H_2O$ (ads. $H_2O$) from [46]. However, the bonding character of Oxygen for these 2 surface states is different, as discussed below.

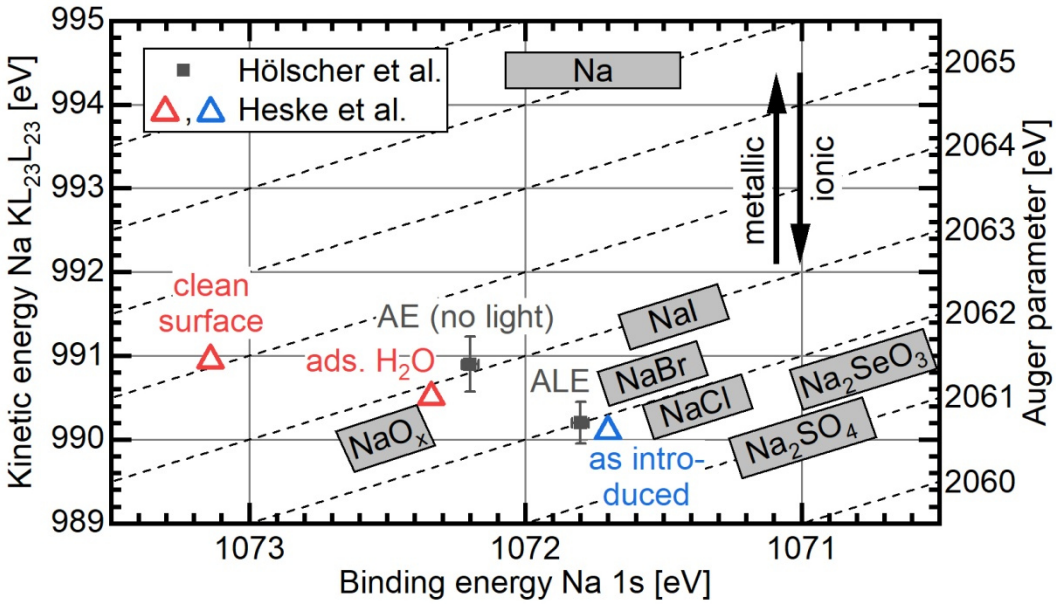


**Figure 21** Characteristics of the Auger Na $KL_{23}L_{23}$ kinetic energy as a function of the Na 1s binding energy for different surface conditions obtained by Heske et al. (red triangles = [46], blue triangles = [45]), respectively paper 1 (squares). The scattered lines represent constant Auger parameter level with a distance of 1 eV, scaled on the right hand side. Determined Auger parameter regions of common Na compounds are indicated by grey squares taken from Ref. [182].

The Auger parameters with ≈ 2063 eV of the latter 2 Na species are in quantitative proximity to the one of $NaO_x$ compounds. In contrast, with an Auger parameter of ≈ 2064 eV the Na compound of the clean surface from Heske et al. [46] matches well that of $NaSe_x$ [139].

For the ALE treated sample, a stronger ionic binding character of Na can be concluded from Figure 21. Thus, the Auger parameter with ≈ 2062 eV corresponds fairly well to the Sodium salts, preferable $Na_2SeO_3$ or other Na-Se-O compounds. Further, the appearance of a Se-O signal for the ALE treated sample in Figure 4 of Paper 1 supports the thesis of a Na-O-Se complex formed due to ALE.

In accordance with the Na 1s peak, likewise the O 1s peak of the ALE sample reveals a lower binding energy with $E_b \approx 531.6$ eV compared to the AE sample with $E_b \approx 532.5$ eV in Figure 4 of Paper 1. In Ref. [46] it is shown that the O 1s peak for adsorbed $H_2O$ on the CIGSe surface is centred at a binding energy of $E_b \approx 534.0$ eV. Here raises the question if the O 1s peak of the AE sample stands for a third, may be passivating species. Or, is this peak the result of an overlap of the adsorbed O species located at 534.0 eV and the detrimental O species located at 531.6 eV. The answer can be obtained from Figure 22. By a multiple-peak fit consisting of 2 peaks centred at 531.6 eV and 534.0 eV, the O 1s peak from the AE sample in Paper 1 cannot reconstructed in Figure 22 a). Only by adding a third peak with a variable peak centre produces a satisfactory fitting result. In Figure 22 b) a binding energy of $E_b \approx$ 532.3 eV is found for the third O species. This third O species is a conceivable explanation for increased TRPL decay times observed on CIGSe layers after storage in dry air and darkness. If this oxygen species originates from additional adsorbents such as $NO_x$, $SO_x$, and $CO_x$ or from a reaction product of Na and O cannot completely solved in this work. No peak shifts of N, S, and C signals in XPS-measurements are observable between the ALE and the AE sample in Paper 1. Hence, a Na-O bonding complex seems to be most probable.

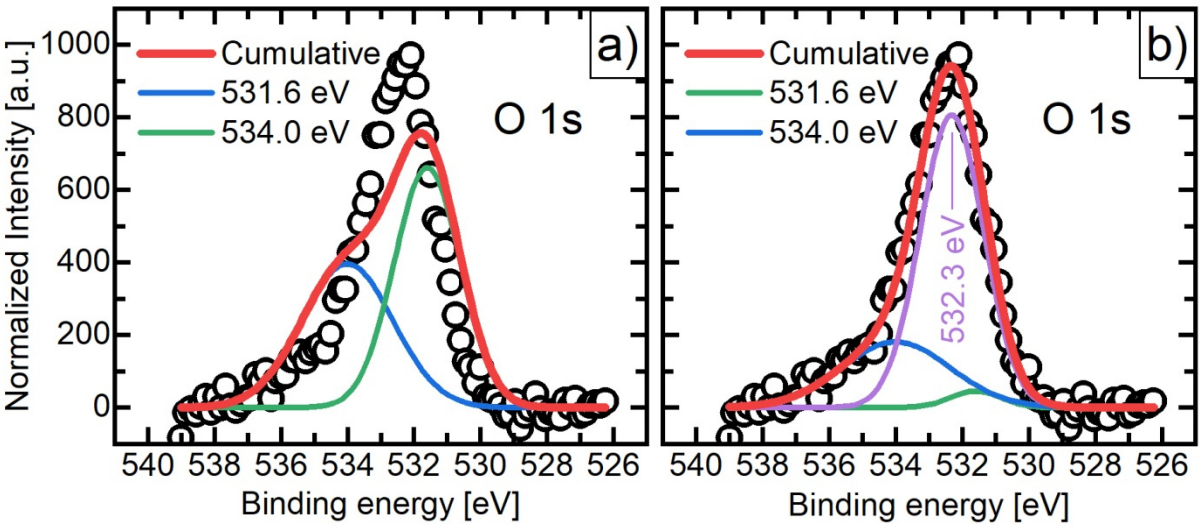


**Figure 22** Peak fits of the O 1s core-level of the non-illuminated AE sample shown in Figure 4 of paper 1. With (a) two overlapping Voigt profiles centred invariable at 531.6 eV and 534.0 eV as well as (b) supplemented by a third Voigt profile with a fitted peak centre at 532.3 eV.

A further consistencies between Paper 1 and Ref. [46] is the detrimental O species located at a binding energy of $E_b \approx 531.6$ eV. Thus, with a stepwise annealing from 100 K to room temperature a shift of the O 1s peak from 534.0 eV for adsorbed $H_2O$ to 531.6 eV observed in Ref. [46]. Giving reasons that the O state after annealing is identical to the one observed for the ALE sample in Paper 1. The question that remains is, if the O 1s peak shift in [46] is triggered by increasing temperature or by X-ray exposure. Nevertheless, from the finding of [46] a formation of $Na_2CO_3$ responsible for the detrimental ALE-effect can be excluded. Because the CIGSe surfaces were exposed to $H_2O$ after a sputter cleaning step and subsequently annealed in ultra-high vacuum.

*Indications for ALE modifications localized on the surface*

A first indication that ALE solely affects the surface can be traced back to the observed Se-O and Na 2s signals in Figure 4 of Paper 1. XPS investigations by Heske et al. [45] revealed that these 2 signals vanish after cleaning the surface by sputtering. The investigated sample in [45] was exposed to ambient air, may be in combination with light. Indications that the "as introduced" status of this sample is equivalent to the ALE treated status in Paper 1 have been obtained from the similar Auger parameters in Figure 21. Niles et al. [139] observed via depth dependent XPS that the concentration of Se bonded to O decreases rapidly by 2 orders of magnitude within the first 4 nm. Whereas, the Oxygen concentration decreases only by 1 order of magnitude at a distance of 12 nm referred to the surface [139].
At the end of Paper 1 it can be shown by $V_{OC}(T)$-measurements that solar cells with ALE absorbers are dominated by recombination at the CIGSe/CdS interface. This emphasizes the previous argumentation that the lifetime reduction in TRPL-measurements due to ALE can be ascribed to a detrimental modification of the CIGSe surface. Details about the verification of interface recombination are discussed in section 4.3.

## 4.2. Disclosure of ALE kinetics and self-healing by HLS

The effects of ALE on bare CIGSe layers in Paper 1 of the previous section are obtained with an illumination intensity corresponding to 1 sun (0.1 W $cm^{-2}$). Exposure of CIGSe layers to such high light intensities is not usual in the processes of manufacturing or handling with contact to ambient air. Therefore, Paper 2 studies ALE as a function of light intensity and light dose. It is shown that reducing the light intensity far below 1 sun is no guarantee against degradation of the TRPL lifetime. The applied light intensities during ALE in Paper 2 are related to a well illuminated laboratory, estimated with 0.003 suns ($3 \cdot 10^{-4}$ W·$cm^{-2}$). Hence, an important observation in Paper 2 is that a retention time for 10 min of the bare CIGSe layer under laboratory conditions reduces the averaged TRPL decay constant down to 30% of its initial value.

In advancement to Paper 1, Paper 2 tracks the impairing effect of ALE on one and the same sample. It is shown by use of TRPL-measurements on CIGSe/CdS devices that the increased recombination of ALE-absorbers is still present after CBD of the CdS buffer layer. A kinetic inhibition of the ALE effect is concluded in Paper 2 from the comparison of TRPL-lifetime reductions of samples with different ALE times but identical light dose. A stronger lifetime reduction of an absorber results into a higher performance deterioration of the completed solar cell.

A fundamental discovery of Paper 2 is the (self-) recovery of ALE devices after HLS under open circuit condition ($HLS_{OC}$). Thus, all J-V-parameters (except $J_{SC}$) are levelling up to the values of the non-ALE sample. However this reparation process is metastable and can be revised by applying voltages $\leq$ 0 V independent from illumination (DA, $HLS_{CC}$). The reparation process is accelerated by increased temperatures (here: 85°C), indicating diffusion and/or chemical reactions during the metastable changes of solar cells. Further accompaniments of HLS and the problem of reduced $J_{SC}$ after HLS are discussed in section 4.3.

# Critical role of air-light exposure on co-evaporated $Cu(In,Ga)Se_2$ solar cells

**Torsten Hölscher, Thomas Schneider, Matthias Maiberg, and Roland Scheer**

*Institute of Physics, Martin-Luther-University Halle-Wittenberg, 06120 Halle, Germany*

We present a comprehensive study concerning the light exposure of bare $Cu(In,Ga)Se_2$ (CIGSe) layers in ambient air and its impact on the electrical properties of the solar cells. With time-resolved photoluminescence (TRPL) a degradation of the minority charge carrier lifetime after air-light exposure of CIGSe layers is observed. This degradation is related to a light induced modification of the CIGSe surface and persists upon completion of the solar cells. A strong reduction in solar cell performance from ~16% down to ~13% reflects the degradation effect of the solar cell's absorber. The deteriorated solar cell performance can be recovered by light soaking of the complete solar cell at increased temperatures of 85 °C.

Link to original publication: https://doi.org/10.7567/JJAP.57.08RC07

### 4.2.1. Supporting information and considerations of Paper 2

*Participation of excited charge carriers during ALE reaction*

In Figure 1 (b) of Paper 2 a severe TRPL-lifetime reduction of up to ≈ 15% is obtained after 12 h AE in darkness for sample CIGSe D. As a reminder, while storing bare CIGSe layers for the identical time period in dry air (+$N_2$) no degradation of the lifetime is observable. This points towards a similar degradation process as effected by ALE, but with thermal excitation of charge carriers instead of light excitation.

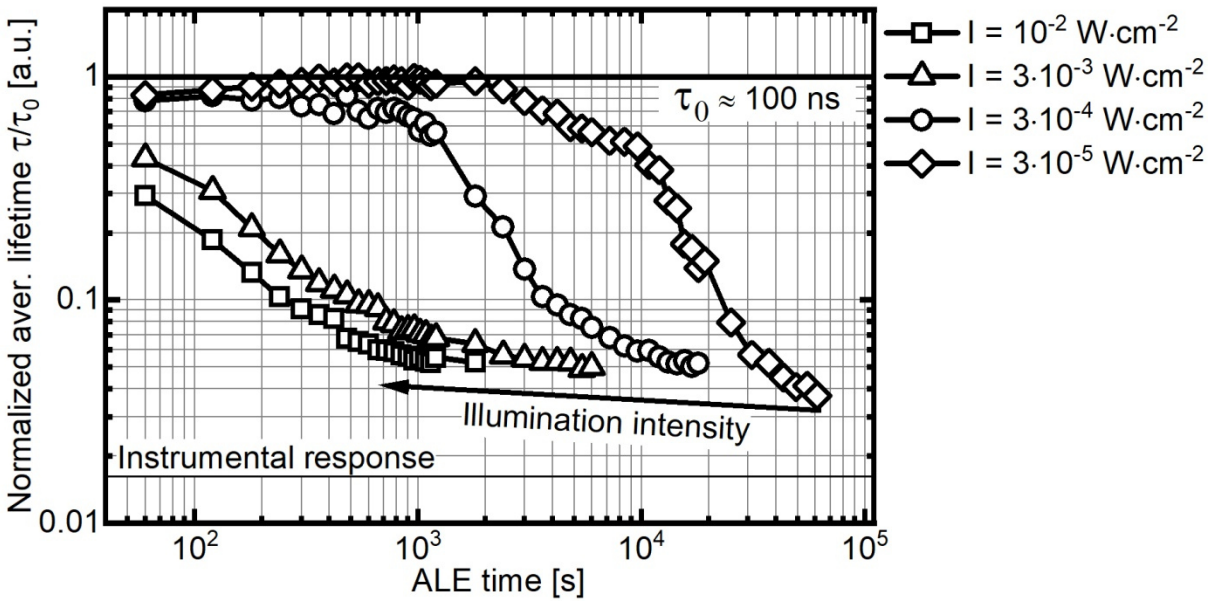


**Figure 23** Normalized average decay times as a function of ALE duration for 4 different illumination intensities obtained on bare CIGSe layer of one and the same batch. The initial lifetime of $\tau_0 \approx 100$ ns is used for normalisation.

A further indication that excited charge carriers are involved in the ALE surface modification can be obtained from Figure 23. The shapes of the curves in Figure 23 remind of the kinetics of chemical equilibrium reactions. The reaction velocity depends on the light intensity during ALE, equally to the injection level of excited charge carriers. The 2 lowest intensities in Figure 23 are kinetically inhibited in the first 700 s for $I = 3 \cdot 10^{-4}$ Wcm$^{-2}$, and in the first 2000 s for $I = 3 \cdot 10^{-5}$ Wcm$^{-2}$. The sample illuminated with the lowest ALE intensity, however, first exhibits an increasing trend (after the initial decay of the lifetime from the reference level $\tau_0$). A possible explanation is that the deteriorating ALE reaction is overcompensated by a passivation reaction. The lifetime enhancement under very low ALE intensities in Figure 23 is

may be subjected to the identical passivation effect observed in Figure 2 of Paper 1 after storage in dry air and darkness.

*Band bending at the bare absorber surface*

In the former section a competing passivation reaction was considered for the temporarily increasing trend of the normalized decay times under very low ALE intensities. An alternative explanation of this effect can be given with the band bending situation at the surface. It is shown by Heske et al. in Ref. [46] that accumulation of Na at the surface, as equally observed for ALE, effects a downward bending of the bands at the surface. On the other hand in Ref. [46] a reduction of the downward band bending is found after $H_2O$ adsorption, which is referred by the authors to the passivation of Na at the surface. No further band bending in [46] is induced by the detrimental surface reaction of Na + $H_2O$(ads.) + CIGSe.

With regard to TRPL measurements a severe downward band bending due to Na accumulation at the surface is able to reduce the recombination rate over surface states. The reason is the transport of excited holes away from the surface into the bulk causing a reduction of the hole density at the surface. This translates into a local separation of holes within the bulk from electrons at the surface, reducing the recombination rate over surface states. As a consequence, the TRPL decay should be dominated by transport mechanisms of electrons and holes to recombine with each other. This apparent passivation mechanism (via band bending) depends on the position of the Fermi-level as well as on the density and type of defects at the surface. In order to prove this hypothesis further experiments such as ultra-violet photoelectron spectroscopy (UPS) are necessary.

By further elapse of ALE time, it is assumed that at the point where the decay times in Figure 23 start to fall the downward bend banding reduces and surface recombination becomes dominant due to a reduced local separation of charge carriers. However, to describe the strong reduction of the decay time down to 0.05 (5 ns) at the end of ALE in Figure 23 a supporting downward band bending at the surface is mandatory. This can be shown by assuming no surface band bending. In that case, following Maiberg and Scheer [162], the TRPL lifetime $\tau_{n,S}$ is limited by diffusion of minority charge carriers to the surface and can be approximated by

$$\tau_{n,S} = \frac{d_a}{S_n} + \frac{2}{5} \cdot \frac{q}{k_B T} \cdot \frac{d_a^2}{\mu_n}. \qquad \textbf{4.1}$$

Using the maximum recombination velocity of $S_n = 10^7$ cm/s for T = 300 K and an absorber thickness of $d_a$ = 2.8 µm the electron mobility has to be $\mu_n \gtrsim 250$ $cm^2V^{-1}s^{-s}$ to achieve the

final lifetimes of $\lesssim$ 5 ns in Figure 23. But, simulations of TRPL experiments reveal electron mobilities with $\mu_n \lesssim 10$ $cm^2V^{-1}s^{-1}$ [Höl7], which would corroborate the existence of a downward band bending in the case of dominating surface recombination due to ALE.

*Metastable TRPL-transients of CIGSe/CdS devices*

In section 3.4 of Paper 2 a metastable character is found for solar cells with ALE absorbers. First it should be mentioned that the depicted progress of J-V-characteristics in Figure 5 of Paper 2 is also observed on devices with non-ALE absorbers, but with smaller amplitude.

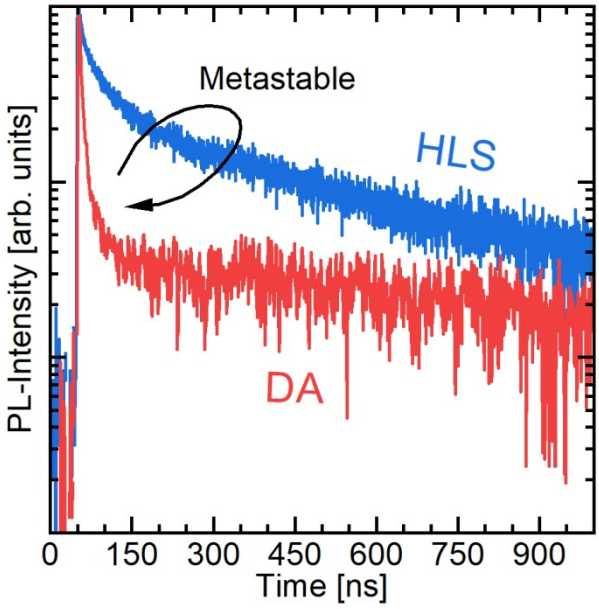


**Figure 24** Metastable changes of TRPL-transients examined on CdS covered non-ALE CIGSe layers.

With respect to Figure 24 a metastable character is observable in TRPL-measurements of non-ALE CIGSe + CdS hetero structures too. The shapes of the 2 transients in Figure 24 indicate an enhanced separation of charge carriers in the HLS state. Charge carrier separation translates into a fast initial decay (separation) and a slow second decay (reinjection). The time constant of charge carrier separation is direct proportional to the depletion width of the absorber $w_a$ [163]. This means the steeper the initial decay the smaller is $w_a$. For a completely depleted buffer layer the depletion width of the absorber as a function of the doping density can be determined from the charge neutrality condition $N_{A,a}w_a = N_{D,b}d_b$. With this in mind, the shapes of the TRPL transients in Figure 24 can be interpreted as follows. In the case of the DA state the separation process is slowly enough (large $w_a$) that a distinct initial decay appears in TRPL measurements. After HLS the initial time constant decreases (small $w_a$) and

cannot resolved by the TRPL setup (time resolution ≈ 1.5 ns) anymore. Further, after passing through the initial decay in Figure 24 the PL-Intensity of the HLS transient is ≈ 1 order of magnitude higher, compared to the DA transient. In combination with a faster second decay after HLS this observation can be explained with (1) a smaller depletion width $w_a$, reducing the spatial distance of separated charge carriers and (2) a lower barrier for reinjection of excited electrons into the absorber bulk (or holes into the depletion region), enhancing the possibility of recombination. The former conclusions point towards an increased p-type doping of the absorber after HLS and may be explains the metastable character of solar cells with non-ALE absorbers. However, as shown in the next section, the recovery of solar cell with ALE absorbers can be referred to a different mechanism evoked by HLS.

## 4.3. Existence and elimination of dominant interface-recombination

After disclosing the phenomenology of ALE and HLS in the previous sections with Paper 1 and Paper 2, this section concentrates with Paper 3 on the microscopic description of solar cell modifications due to ALE and HLS. In Paper 1 it could be shown with XPS-measurements that ALE modifies the CIGSe surface chemistry. By means of $V_{OC}(T)$-measurements it was concluded in Paper 1 that this surface modification drives the completed solar cells into dominant interface recombination, reducing $V_{OC}$ and device efficiency. Recent $V_{OC}(T)$-measurements in Paper 3 are confirming the $V_{OC}(T)$-results of Paper 1. Investigations by 2 further independent methods, namely $V_{OC}(t)$-measurements and voltage dependent admittance spectroscopy, Paper 3 gives the unique evidence that interface recombination plays a dominant role in solar cells made of ALE absorbers. In this context, voltage dependent admittance spectroscopy in Paper 3 gives the ability to concatenate interface recombination with the occurrence of a spatially narrow defect response, usually caused by interface states. In the case of non-ALE samples $V_{OC}(T)$- and $V_{OC}(t)$-measurements indicates no limitation by interface recombination and hence the occurrence of the spatially narrow defect response is absent, emphasizing the relationship of interface recombination and this admittance signature.
As shown in Paper 2 HLS under open circuit condition increases the J-V-parameter (except for $J_{SC}$) of ALE devices to an identical level observed on non-ALE devices. In Paper 3 this improvement can be correlated with $V_{OC}(t)$- and $V_{OC}(T)$-measurements to a relocation of the dominant recombination region from the interface into the absorber bulk (SCR or QNR). This finding is accompanied by a suppression of the spatially narrow defect signal in voltage dependent admittance spectroscopy. With GDOES-measurements before and after applying HLS it can be demonstrated in Paper 3 that the latter results come along with a segregation of Na at the CIGSe/CdS interface.
From the known accumulation of Na found with XPS-measurements in Paper 1 for ALE absorbers, an ambivalent role for Na is concluded in Paper 3. Hence, during ALE the availability of Na acts detrimental to the electronic quality of the absorber surface. Conversely, after HLS a passivation of interface defects by Na becomes evident for devices with ALE absorbers. If this observed passivation effect can be extended to other defect states is still under debate.

# Impact of air-light exposure on the electrical properties of $Cu(In,Ga)Se_2$ solar cells

**Torsten Hölscher, Thomas Schneider, Matthias Maiberg, and Roland Scheer**

*Institute of Physics, Martin-Luther-University Halle-Wittenberg, 06120 Halle, Germany*

The impact of air-light exposure of bare $Cu(In,Ga)Se_2$ layers is investigated by measuring the performance of completed solar cells. Solar cells formed from air-light exposed absorbers reveal inferior cell parameters by about 10% regarding open circuit voltage, fill factor, and efficiency compared to cells from non-illuminated absorbers. Time-dependent and temperature-dependent open circuit voltage measurements give reasons that the solar cell impairment by air-light exposure of the bare absorbers is due to interface recombination. Interface states are detected by admittance spectroscopy. Heat-light soaking of complete solar cells – having formerly degraded interfaces – recovers the solar cell parameters up to the non-degraded levels. Paradoxically, both the air-light induced degradation of bare absorbers and the revision of cell parameters after light annealing go along with a light induced segregation of sodium at the $Cu(In,Ga)Se_2$ surface and $Cu(In,Ga)Se_2$/CdS interface, respectively.

Link to original publication: https://doi.org/10.1002/pip.3041

### 4.3.1. Supporting information and considerations of Paper 3

*Closer inspection of $V_{OC}(t)$-transients*

The study in Paper 3 uses the methods $V_{OC}(T)$, $V_{OC}(t)$, and voltage dependent admittance spectroscopy as introduced in sections 3.1 and 3.2. For simplification, in Paper 3 the results of $V_{OC}(T)$ and $V_{OC}(t)$ are discussed on the basis of a $pn^+$ structure, giving a type inversion at the interface of the lower doped p-type material. Further the capture cross sections for electrons and holes of interface states are assumed to be equal in Paper 3, resulting in a common reference current density given with equation 3. In spite of this, the conclusions in Paper 3 are not in conflict with the predictions in section 3.1. Moreover, the analysis of the $V_{OC}(t)$ method examined on a $p\text{-}n^-\text{-}n\text{-}n^+$ structure in 3.1.2 allows an alternative interpretation of the $V_{OC}(t)$ transients shown in Figure 3 B) of Paper 3. The subject of interest is the change in slope trend after $t \approx 3000$ s of the $V_{OC}(t)$ transients obtained on the 10 and 60 min ALE cells. A possible explanation for this occurrence is given in Paper 3 with passivation of interface state due to long time illumination analogous to the HLS effect. Another explanation can be deduced from Figure 16 on page 68. In the case of acceptor like interface states (as found in Paper 4) for the declining part of the $V_{OC}(t)$-transient it holds $S_{n,if}n_{if,a} > S_{p,if}p_{if,a}$ and the recombination current density over inface states is limited by the voltage dependent hole density at the surface. After passing through the minimum of the $V_{oc}(t)$ transient at $t \approx 3000$ s the recombination current density becomes limited by electrons ($S_{n,if}n_{if,a} < S_{p,if}p_{if,a}$) causing an increasing trend of $V_{OC}(t)$. As shown in Figure 16 on page 68 the change of a decreasing to an increasing slop can be directly correlated to an increasing doping density $N_{A,a}$ of the absorber, resulting in an increased electron and decreased hole barrier at the CIGSe/CdS interface.

*Indication for dominating SCR recombination after HLS*

In Paper 3, Figure 6 A) it remarkable that for both, ALE and non-ALE-samples, the activation energy $E_A$ of the saturation current density increases to 1.28 eV after HLS. In section 3.1.1 (see Figure 15) it was figured out that $E_A = E_{g,a} + 3 \cdot kT$ should be obtained for a device limited by QNR recombination. With the narrowing of a uniform band gap energy corresponding to $E_{g,a} = 1.15$ eV, in Paper 3 the non-ALE device before HLS can be verified with $E_A = 1.24$ eV $\approx E_{g,a} + 3 \cdot kT$ to be dominated by QNR recombination. After HLS the activation energy is increased by additional 0.04 eV ≈ 1.5 kT giving $E_A = 1.28$ eV $\approx E_{g,a} + 4.5 \cdot kT$. The relation $E_A = E_{g,a} + 4.5 \cdot kT$ was found in section 3.1.1 for (1) a device limited by recombination over donor states at the interface or (2) a device dominated by recombination within the SCR.

Under the made assumption that $V_{OC}(t)$ under red light illumination is a function of the doping density $V_{OC}(t) \rightarrow V_{OC}(N_{A,a})$ as well, dominating recombination over donor states at the interface after HLS can be ruled out. Because in section 3.1.2 (Figure 16, page 68) a decreasing trend of $V_{OC}$ for increasing $N_{A,a}$ is found in the case of dominant recombination over IF-donor states. Hence, with the observation of $E_A = 1.28$ eV $\approx E_{g,a} + 4.5 \cdot kT$ in Figure 6 A) and increasing trends for all $V_{OC}(t)$-transients in Figure 6 B) of Paper 3, dominating SCR recombination should be taken into account after HLS, which seems to be independent from the ALE status of the absorber. **W**ith this background it can be concluded that HLS drives the solar cell into dominating SCR recombination.

*Reduced depletion width of the absorber after HLS*

A systematic by-product of HLS is the reduction of $J_{SC}$ by $\approx 1$ mA·cm$^{-2}$. From Figure 5 in Paper 3 it is apparent that this effect is independent from the ALE status of the absorber layer. For solar cells with non-ALE absorbers this produces a loss in device efficiency after HLS. With the external quantum efficiency (EQE), measured on a non-ALE device, in Figure 25 the loss in $J_{SC}$ after HLS can be referred to range of the light spectrum. A reduced collection-efficiency for long wavelengths is a typical sign of a shorter depletion width $w_a$ usually caused by an increased doping density $N_{A,a}$ of the absorber. This finding supports the postulated change in depletion width, describing the metastability of TRPL transients obtained on CIGSe + CdS hetero-structures in section 4.2.1.

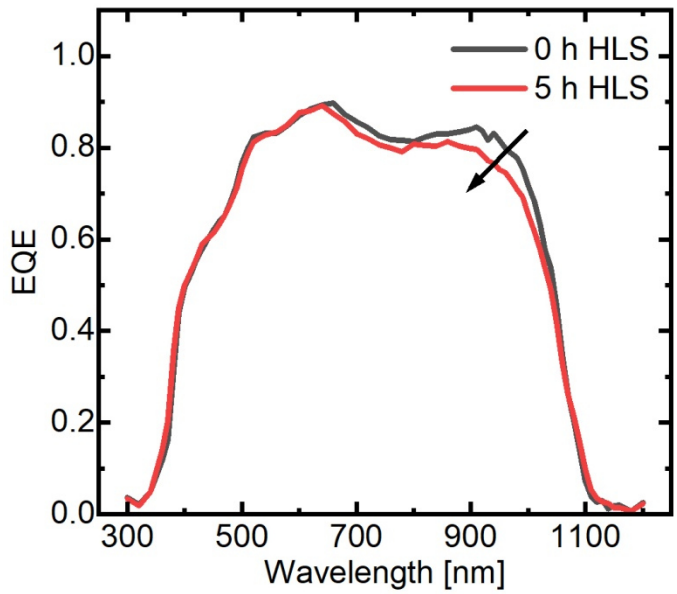


**Figure 25** External quantum efficiency as function of HLS duration measured on the non-ALE device of the study in paper 3.

## 4.4. Quantification of interface defects and device modelling

An important result from Paper 3 of the previous section was the identification of an interface defect level responsible for dominating interface recombination in solar cells made of ALE absorbers. In order to elucidate the physical properties of these defect states, in Paper 4 one-dimensional numerical device simulations with SCAPS 1d is performed.

From a detailed analysis of voltage dependent admittance spectra, 3 distinct signals are found for ALE devices in Paper 4. These signals can be ascribed to the common N1-effect, a deep bulk defect (B), and the ALE induced interface defect (IF). By comparing simulated admittance- and J-V-data with the experimental curves the parameter room of the 3 signatures could be narrowed down to the following solutions.

N1 This signal is best modelled in Paper 4 with a transport barrier for majority carriers at the back contact as proposed by Eisenbarth et al. [77]. However, Paper 4 regards for the first time the weak temperature dependence of the characteristic frequency of the N1-feature in admittance spectroscopy. Thus the transport barrier has to be supplemented by an interfacial layer (IL) in between the absorber and the metallic back contact. This layer is specified by an unusual low effective density of states of the valence band ($N_V \approx 10^{16}$ cm$^{-3}$) to allow the weak temperature dependence of the N1 characteristic frequency.

(B) In Paper 4 a deep donor trap located energetically close to midgap well describes this signature. (B) here is referred to the 2nd ionization-level D2(+/++) of the shallow minority charge carrier trap D2(0/+) found in earlier studies by simulations of TRPL-experiments [Höl7],[Höl8],[Höl9]. This assumption is based on (1) the strong asymmetrical capture cross sections for electrons ($\sigma_n = 10^{-11}$ cm$^2$) and holes ($\sigma_p = 10^{-19}$ cm$^2$) as well as (2) the identical defect density of (B) and D2(0/+).

(IF) Finally, in Paper 4 the interface states caused by ALE are found to be of acceptor type. Hence, the capture cross sections amount to $\sigma_p = 3 \cdot 10^{-11}$ cm$^2$ for holes and $\sigma_n = 4 \cdot 10^{-16}$ cm$^2$ for electrons. Energetically, the IF-defect is Gaussian distributed with a standard deviation of $\sigma(E_d) = 0.15$ eV located at $E_d = 0.3$ eV above the valence band. The integrated 2 dimensional defect density resulted in $N_d = 3.5 \cdot 10^{11}$ cm$^{-2}$.

The main achievements of Paper 4 are the establishment of a physical model for the ALE affected CIGSe/CdS interface as well as an alternative interpretation of the N1-response in admittance spectroscopy.

# Device simulation of $Cu(In,Ga)Se_2$ solar cells by means of voltage dependent admittance spectroscopy

**Torsten Hölscher[1], Thomas Walter[2], Thomas Schneider[1], Matthias Maiberg[1], and Roland Scheer[1]**

*[1]Martin-Luther-University Halle-Wittenberg, Von-Danckelmann-Platz 3, 06120 Halle, Germany*

*[2]University of Applied Sciences Ulm, Albert-Einstein-Allee 55, 89081 Ulm, Germany*

The simulation of solar cell devices is important for the understanding of defect physics and loss mechanisms in real solar cells. On the other hand, voltage dependent admittance spectroscopy delivers essential information for establishing a baseline simulation model of $Cu(In,Ga)Se_2$ (CIGSe) solar cells. Here we give an explanation for the weak temperature dependence of the N1-signal, the latter being not compatible with a bulk defect or with a simple hole barrier at the Mo back contact. Furthermore, we find a $E_{d,IF} - E_V \approx 0.3$ eV deep recombination-active acceptor state at the absorber/buffer interface made of air-light exposed CIGSe absorbers. This gives us the ability to explain the reduction of power conversion efficiency of solar cells made from air-light exposed absorbers. From the voltage dependent capacitance step of this interface defect we can deduce the formerly unknown position of the Fermi level at the hetero junction in equilibrium which is close to mid-gap. Simulation of dark J-V curves allows a refinement of the parameter of this absorber/buffer interface defect, resulting in a defect density of $N_{d,IF} \approx 3.5 \cdot 10^{11}$ cm$^{-2}$ as well as capture cross sections of $\sigma_n \approx 4 \cdot 10^{-16}$ cm$^2$ for electrons and $\sigma_p \approx 3 \cdot 10^{-11}$ cm$^2$ for holes.

Link to original publication: https://doi.org/10.1016/j.tsf.2018.11.022

# 5. Conclusion

The objective of this work was to disclose the decisive role of light during air exposure (AE) of bare CIGSe layers and its impact on complete solar cells. In this context the abbreviation ALE for air-light exposure was introduced. To discriminate between the effects induced by AE and ALE, bare CIGSe absorber layers were exposed to ambient (humid) air for identical time frames, but with (ALE) and without (AE) white light illumination. The crucial differences found for AE and ALE absorbers are summarized in the following enumeration.

1. With TRPL-measurements it was shown that ALE with high light intensities (1 sun) causes after a short time (10 min) a severe reduction by 2 orders of magnitude for the evaluated minority charge carrier lifetime. Reducing the ALE light intensity by a certain factor cannot be transferred to an extension of ALE-time by the same factor. Accordingly, ALE with 0.03 suns for 10 min elicits equally a severe lifetime reduction of up to 1 order of magnitude in TRPL measurements. In contrast, even after 12 h storage of CIGSe absorbers in ambient (humid) air without illumination, almost no reduction in TRPL-lifetime is observed.
2. The investigation of CIGSe surfaces via XPS after ALE and AE with identical time frames revealed in the case of the ALE sample a higher concentration of Na and O at the very surface. Further, it could be shown that ALE effects a shifting of the Na 1s and O 1s signal peaks to lower binding energies. These peak shifts have been attributed to a chemical reaction of O and Na at the CIGSe surface, forming a detrimental Na-O-CIGSe complex as suggested by Heske et al. [46]

After identifying the ALE-effect on bare CIGSe absorber layers, solar cells made from ALE absorbers became the subject of investigations. Generally, reduced J-V-parameter (except $J_{SC}$) are obtained on devices with ALE absorbers, indicating that the detrimental surface modification found with XPS is not removed throughout processing the buffer (and window) layer. The reduction in J-V-parameter depends on the ALE-time and light intensity, but not on the ALE light dose. Correspondingly, it was shown that a constant ALE light dose under varying ALE-times and light intensities gives different degrees of J-V-parameter reduction. With the result that the longest ALE-time in combination with the lowest light intensity causes the highest decrease in J-V-parameter, pointing towards a kinetically inhibited reaction during ALE. In this work the highest reductions in J-V-parameter due to ALE have been observed with $\Delta V_{OC} \approx -140$ mV, $\Delta FF \approx -10\%$, and $\Delta\eta \approx -5\%$. By means of $V_{OC}(T)$- and

$V_{OC}$(t)-measurements these reductions were traced to dominant recombination at the absorber/buffer interface. The reason for increased interface recombination could be related to the occurrence of an interface defect signature obtained on ALE devices in voltage dependent admittance spectroscopy. In comparison, for non-ALE samples no dominant interface recombination were deduced from $V_{OC}$(T)- and $V_{OC}$(t)-measurements. Thus, no signature of an interface defect was detected in voltage dependent admittance spectroscopy of non-ALE solar cells.

In the further course it could be shown that after applying a HLS for several hours under open-circuit conditions recovers the inferior J-V-parameter of ALE cells comparable to the level of non-ALE cells. However, after DA the J-V-parameter relaxes back to the former inferior state. By a repeated application of HLS the solar improves again, indicating a metastable characteristic of the HLS and DA state. A similar behaviour was also observed for solar cells with non-ALE absorbers. For these samples the metastable character was referred to a change of the absorber doping density (increased after HLS, reduced after DA.) The increased absorber doping density was considered responsible for the reduced $J_{SC}$ after HLS due to a shortened depletion width within the absorber. Consequently, HLS has a detrimental effect on the performance of non-ALE solar cells. The improving effect of HLS on ALE devices could be referred to a spatially redistribution of Sodium. In this context, GDOES depth profiles revealed a HLS induced accumulation of Na at the absorber/buffer interface. In combination with the vanishing of the interface defect response in voltage dependent admittance spectroscopy, a passivating role was concluded for Sodium. If the redistribution of Na is also responsible for the increased absorber doping after HLS is addressed to future work. Finally, the properties of the detrimental defect states at the absorber/buffer interface caused by ALE were uncovered by 1 dimensional device simulations. This interface defect was found to be of acceptor type levelled on $E_d - E_V = 0.3$ eV with a density of $N_d = 3.5 \cdot 10^{11}$ $cm^{-2}$. The energetic distance to $E_V$ of this defect level matches well the activation energy of the often observed N2-signature in admittance spectroscopy of the literature [106, 183]. If the here found interface signature could also be responsible for the N2-bulk signature is still under debate.

The results of this work are relevant for manufactures and laboratories, which are working with bare CIGSe layers under ambient conditions. On the other hand the ALE effect should be regarded in device development. As observed by Reichardt et al. [184] replacing the CdS buffer layer by Zn(O,OH) creates a photo-induced oxygenation of Se at the absorber/buffer interface due to X-ray irradiation.

# 6. Outlook

Proposals for future works concerning the ALE effect are given with the following key notes.

- In this study the soda lime glass substrate was acting as the source for Sodium incorporation into the CIGSe layer. A more modern method is the incorporation of Sodium by a NaF post-deposition treatment. Preliminary results reveal equally a strong reduction of TRPL-lifetimes after ALE (see Figure 6 on page 21). But, the J-V-parameter of complete solar cells appeared to be unaffected by ALE. The reasons are still unclear.
- Further, doping of CIGSe with Na and additional heavier alkaline metals (K, Cs, Rb) is a prerequisite for achieving highly efficient solar cells. In the case of Potassium, from XPS and SIMS measurements a $KInSe_2$ layer is found on the CIGSe surface [7]. In spite of the changed surface chemistry, TRPL measurements in Figure 26 reveal likewise a significant lifetime reduction after ALE for CIGSe layers with additional doping of heavier alkaline dopants (K, Cs, Rb). However, due to the lack of non-ALE absorbers, acting as references, solar cells have not been fabricated from these absorbers. Accordingly, if the TRPL-lifetime reductions in Figure 26 translate as well into inferior performances of complete solar cells have not yet been verified.

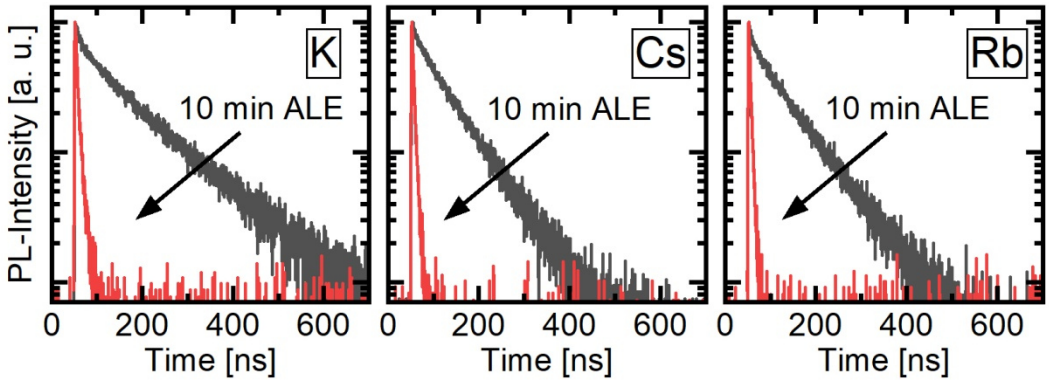


**Figure 26** TRPL-transients before (black) and after 10 min ALE (red) of 3 CIGSe layers differing in the additional doping element K, Cs, and Rb. The light intensity during ALE was 0.1 $W \cdot cm^{-2}$. Na-doping of the CIGSe layers took place via in-diffusion from the SLG substrate at high substrate temperatures. Incorporation of K, Cs, and Rb was achieved by PDT.

- UPS measurements seem to be suitable to enlightening the transport phenomena of minority charge carriers during TRPL measurements. By determining the surface band

bending and Fermi-level position with UPS, a simulation model for the description of the strong lifetime reduction in TRPL experiments could be established. This gives deeper insights into the status of ALE CIGSe layers before depositing the CdS buffer layer. And, may be counteractions to revise the ALE effect can be developed.

- To uncover the role of excited charge carriers on the ALE reaction, ALE with photon energies smaller than the CIGSe band gap could be performed. As light sources IR-lasers or IR-LEDs with a narrow line width should be chosen. Because, it was found that ALE with white light illumination through to different long-pass filters delivered no consistent results in TRPL-measurements. So that the strongest lifetime reduction was observed on the sample illuminated with the longest wavelength range of the white light source.
- Temperature dependent ALE with low light intensities should give the ability to determine the activation energy and may be the kinetic inhibition of ALE reactions.

# References


[1] M. A. Green, Y. Hishikawa, E. D. Dunlop, D. H. Levi, J. Hohl-Ebinger, and A. W. Y. Ho-Baillie, Solar cell efficiency tables (version 52), *Progress in Photovoltaics*, **26**, 7, 427-436 (2018).

[2] M. Raugei, E. Leccisi, and V. M. Fthenakis, What Are the Energy and Environmental Impacts of Adding Battery Storage to Photovoltaics? A Generalized Life Cycle Assessment, *Energy Technology*, 1901146 (2020).

[3] K. P. Bhandari, J. M. Collier, R. J. Ellingson, and D. S. Apul, Energy payback time (EPBT) and energy return on energy invested (EROI) of solar photovoltaic systems: A systematic review and meta-analysis, *Renewable & Sustainable Energy Reviews*, **47**, 133-141 (2015).

[4] T. Feurer, P. Reinhard, E. Avancini, B. Bissig, J. Lockinger, P. Fuchs, R. Carron, T. P. Weiss, J. Perrenoud, S. Stutterheim, S. Buecheler, and A. N. Tiwari, Progress in thin film CIGS photovoltaics - Research and development, manufacturing, and applications, *Progress in Photovoltaics*, **25**, 7, 645-667 (2017).

[5] F. Kessler, D. Hariskos, S. Spiering, E. Lotter, H. Huber, and R. Wuerz, CIGS Thin Film Photovoltaic—Approaches and Challenges, in: High-Efficient Low-Cost Photovoltaics, Springer, 175-218, (2020).

[6] V. M. Fthenakis, Life Cycle Analysis of Photovoltaics: Strategic Technology Assessment, in: A Comprehensive Guide to Solar Energy Systems, Elsevier, 427-442, (2018).

[7] A. Chirila, P. Reinhard, F. Pianezzi, P. Bloesch, A. R. Uhl, C. Fella, L. Kranz, D. Keller, C. Gretener, H. Hagendorfer, D. Jaeger, R. Erni, S. Nishiwaki, S. Buecheler, and A. N. Tiwari, Potassium-induced surface modification of Cu(In,Ga)$Se_2$ thin films for high-efficiency solar cells, *Nature Materials*, **12**, 12, 1107-1111 (2013).

[8] J. F. Guillemoles, The puzzle of Cu(In,Ga)$Se_2$ (CIGS) solar cells stability, *Thin Solid Films*, **403**, 405-409 (2002).

[9] H. W. Schock and R. Noufi, CIGS-based solar cells for the next millennium, *Progress in Photovoltaics*, **8**, 1, 151-160 (2000).

[10] M. Powalla, S. Paetel, D. Hariskos, R. Wuerz, F. Kessler, P. Lechner, W. Wischmann, and T. M. Friedlmeier, Advances in Cost-Efficient Thin-Film Photovoltaics Based on Cu(In, Ga)$Se_2$, *Engineering*, **3**, 4, 445-451 (2017).

[11] T. Unold and H. W. Schock, Nonconventional (Non-Silicon-Based) Photovoltaic Materials, *Annual Review of Materials Research, Vol 41*, **41**, 297-321 (2011).

[12] H. W. Schock and K. Bogus, Development of CIS solar cells for space applications, in *2nd World Conference Photovoltaic Solar Energy Conversion*, Vienna, 3586-3589 (1998).

[13] P. Jackson, R. Wuerz, D. Hariskos, E. Lotter, W. Witte, and M. Powalla, Effects of heavy alkali elementsin Cu(In,Ga)$Se_2$ solar cells with efficiencies up to 22.6%, *Physica Status Solidi-Rapid Research Letters*, **10**, 8, 583-586 (2016).

[14] R. Kamada, T. Yagioka, S. Adachi, A. Handa, K. F. Tai, T. Kato, and H. Sugimoto, New World Record Cu(In,Ga)(Se,S)$_2$ Thin Film Solar Cell Efficiency Beyond 22%, *2016 Ieee 43rd Photovoltaic Specialists Conference (Pvsc)*, 1287-1291 (2016).

[15] J. Nishinaga, T. Nagai, T. Sugaya, H. Shibata, and S. Niki, Single-crystal Cu(In,Ga)$Se_2$ solar cells grown on GaAs substrates, *Applied Physics Express*, **11**, 8, (2018).

[16] S. Siebentritt, M. Igalson, C. Persson, and S. Lany, The electronic structure of chalcopyrites-bands, point defects and grain boundaries, *Progress in Photovoltaics*, **18**, 6, 390-410 (2010).

[17] C. S. Jiang, I. L. Repins, L. M. Mansfield, M. A. Contreras, H. R. Moutinho, K. Ramanathan, R. Noufi, and M. M. Al-Jassim, Electrical conduction channel along the grain boundaries of Cu(In,Ga)$Se_2$ thin films, *Applied Physics Letters*, **102**, 25, (2013).

[18] N. A. Stolwijk, S. Obeidi, J. Bastek, R. Wuerz, and A. Eicke, Fe diffusion in polycrystalline Cu(In,Ga)$Se_2$ layers for thin-film solar cells, *Applied Physics Letters*, **96**, 24, (2010).

[19] C. Persson and A. Zunger, Anomalous grain boundary physics in polycrystalline $CuInSe_2$: The existence of a hole barrier, *Physical Review Letters*, **91**, 26, (2003).

[20] D. Azulay, O. Millo, I. Balberg, H. W. Schock, I. Visoly-Fisher, and D. Cahen, Current routes in polycrystalline $CuInSe_2$ and Cu(In,Ga)$Se_2$ films, *Solar Energy Materials and Solar Cells*, **91**, 1, 85-90 (2007).

[21] D. F. Marron, S. Sadewasser, A. Meeder, T. Glatzel, and M. C. Lux-Steiner, Electrical activity at grain boundaries of Cu(In,Ga)$Se_2$ thin films, *Physical Review B*, **71**, 3, (2005).

[22] D. Abou-Ras, B. Schaffer, M. Schaffer, S. S. Schmidt, R. Caballero, and T. Unold, Direct Insight into Grain Boundary Reconstruction in Polycrystalline Cu(In, Ga)$Se_2$ with Atomic Resolution, *Physical Review Letters*, **108**, 7, (2012).

[23] Z. H. Zhang, X. C. Tang, O. Kiowski, M. Hetterich, U. Lemmer, M. Powalla, and H. Holscher, Reevaluation of the beneficial effect of Cu(In,Ga)$Se_2$ grain boundaries using Kelvin probe force microscopy, *Applied Physics Letters*, **100**, 20, (2012).

[24] M. Burgelman, P. Nollet, and S. Degrave, Modelling polycrystalline semiconductor solar cells, *Thin Solid Films*, **361**, 527-532 (2000).

[25] W. K. Metzger, I. L. Repins, and M. A. Contreras, Long lifetimes in high-efficiency Cu(In,Ga)$Se_2$ solar cells, *Applied Physics Letters*, **93**, 2, (2008).

[26] D. Baek, Carrier Lifetimes in Thin-film Photovoltaics, *Journal of the Korean Physical Society*, **67**, 6, 1064-1070 (2015).

[27] S. A. Dinca, E. A. Schiff, W. N. Shafarman, B. Egaas, R. Noufi, and D. L. Young, Electron drift-mobility measurements in polycrystalline $CuIn_{1-x}Ga_xSe_2$ solar cells, *Applied Physics Letters*, **100**, 10, (2012).

[28] J. Lee, J. D. Cohen, and W. N. Shafarman, The determination of carrier mobilities in CIGS photovoltaic devices using high-frequency admittance measurements, *Thin Solid Films*, **480**, 336-340 (2005).

[29] M. Maiberg, F. Bertram, M. Müller, and R. Scheer, Theoretical study of time-resolved luminescence in semiconductors. IV. Lateral inhomogeneities, *Journal of Applied Physics*, **121**, 8, (2017).

[30] U. Rau and H. W. Schock, Electronic properties of Cu(In,Ga)$Se_2$ heterojunction solar cells-recent achievements, current understanding, and future challenges, *Applied Physics a-Materials Science & Processing*, **69**, 2, 131-147 (1999).

[31] D. Abou-Ras, S. Wagner, B. J. Stanbery, H. W. Schock, R. Scheer, L. Stolt, S. Siebentritt, D. Lincot, C. Eberspacher, K. Kushiya, and A. N. Tiwari, Innovation highway: Breakthrough milestones and key developments in chalcopyrite photovoltaics from a retrospective viewpoint, *Thin Solid Films*, **633**, 2-12 (2017).

[32] W. S. Chen, J. M. Stewart, W. E. Devaney, R. A. Mickelsen, and B. J. Stanbery, Thin film $CuInGaSe_2$ cell development, in *Conference Record of the 23rd IEEE Photovoltaic Specialists Conference*, Louisville (KY, USA), 422-425 (1993).

[33] J. Hedstrom, H. Ohlsen, M. Bodegard, A. Kylner, L. Stolt, D. Hariskos, M. Ruckh, and H. Schock, ZnO/CdS/Cu(In,Ga)$Se_2$ thin film solar cells with improved performance, in *Conference Record of the 23rd IEEE Photovoltaic Specialists Conference*, Louisville (KY, USA), 364-371 (1993).

[34] A. Laemmle, R. Wuerz, and M. Powalla, Efficiency enhancement of Cu(In,Ga)$Se_2$ thin-film solar cells by a post-deposition treatment with potassium fluoride, *Physica Status Solidi-Rapid Research Letters*, **7**, 9, 631-634 (2013).

[35] Y. Sun, S. P. Lin, W. Li, S. Q. Cheng, Y. X. Zhang, Y. M. Liu, and W. Liu, Review on Alkali Element Doping in Cu(In, Ga)$Se_2$ Thin Films and Solar Cells, *Engineering*, **3**, 4, 452-459 (2017).

[36] P. Jackson, R. Wurz, U. Rau, J. Mattheis, M. Kurth, T. Schlotzer, G. Bilger, and J. H. Werner, High quality baseline for high efficiency, Cu($In_{1-x}$,$Ga_x$)$Se_2$ solar cells, *Progress in Photovoltaics*, **15**, 6, 507-519 (2007).

[37] S. Niki, M. Contreras, I. Repins, M. Powalla, K. Kushiya, S. Ishizuka, and K. Matsubara, CIGS absorbers and processes, *Progress in Photovoltaics*, **18**, 6, 453-466 (2010).

[38] V. Probst, W. Stetter, W. Riedl, H. Vogt, M. Wendl, H. Calwer, S. Zweigart, K. D. Ufert, B. Freienstein, H. Cerva, and F. H. Karg, Rapid CIS-process for high efficiency PV-modules: development towards large area processing, *Thin Solid Films*, **387**, 1-2, 262-267 (2001).

[39] A. Redinger, S. Levcenko, C. J. Hages, D. Greiner, C. A. Kaufmann, and T. Unold, Time resolved photoluminescence on Cu(In, Ga)$Se_2$ absorbers: Distinguishing degradation and trap states, *Applied Physics Letters*, **110**, 12, (2017).

[40] W. K. Metzger, I. L. Repins, M. Romero, P. Dippo, M. Contreras, R. Noufi, and D. Levi, Recombination kinetics and stability in polycrystalline Cu(In,Ga)$Se_2$ solar cells, *Thin Solid Films*, **517**, 7, 2360-2364 (2009).

[41] G. El-Hajje, D. Ory, M. Paire, J. F. Guillemoles, and L. Lombez, Contactless characterization of metastable defects in Cu(In,Ga)$Se_2$ solar cells using time-resolved photoluminescence, *Solar Energy Materials and Solar Cells*, **145**, 462-467 (2016).

[42] S. Shirakata, S. Yudate, J. Honda, and N. Iwado, Photoluminescence of Cu(In,Ga)$Se_2$ in the Solar Cell Preparation Process, *Japanese Journal of Applied Physics*, **50**, 5, (2011).

[43] T. P. Weiss, R. Carron, M. H. Wolter, J. Löckinger, E. Avancini, S. Siebentritt, S. Buecheler, and A. N. Tiwari, Time-resolved photoluminescence on double graded

$Cu(In,Ga)Se_2$ – impact of front surface recombination and its temperature dependence, *Science and Technology of Advanced Materials*, just-accepted, (2019).

[44] S. Shirakata, H. Ohta, K. Ishihara, T. Takagi, A. Atarashi, and S. Yudate, Photoluminescence characterization of surface degradation mechanism in $Cu(In,Ga)Se_2$ thin films grown on Mo/soda lime glass substrate, *Japanese Journal of Applied Physics*, **53**, 5, (2014).

[45] C. Heske, R. Fink, E. Umbach, W. Riedl, and F. Karg, Na-induced effects on the electronic structure and composition of $Cu(In,Ga)Se_2$ thin-film surfaces, *Applied Physics Letters*, **68**, 24, 3431-3433 (1996).

[46] C. Heske, G. Richter, Z. H. Chen, R. Fink, E. Umbach, W. Riedl, and F. Karg, Influence of Na and $H_2O$ on the surface properties of $Cu(In,Ga)Se_2$ thin films, *Journal of Applied Physics*, **82**, 5, 2411-2420 (1997).

[47] D. Braunger, D. Hariskos, and H. Schock, Na-related stability issues in highly efficient polycrystalline $Cu(In,Ga)Se_2$ solar cells, in *Proc 2nd World Conference on Photovoltaic Energy Conversion (WCPEC)*, 511-514 (1998).

[48] D. Braunger, D. Hariskos, G. Bilger, U. Rau, and H. W. Schock, Influence of sodium on the growth of polycrystalline $Cu(In,Ga)Se_2$ thin films, *Thin Solid Films*, **361**, 161-166 (2000).

[49] D. Regesch, L. Gutay, J. K. Larsen, V. Depredurand, D. Tanaka, Y. Aida, and S. Siebentritt, Degradation and passivation of $CuInSe_2$, *Applied Physics Letters*, **101**, 11, (2012).

[50] R. Scheer and H.-W. Schock, Chalcogenide photovoltaics: physics, technologies, and thin film devices, John Wiley & Sons, (2011).

[51] Y. Hamakawa, Thin-film solar cells: next generation photovoltaics and its applications, 1 st ed., Springer-Verlag Berlin Heidelberg New York, (2004).

[52] G. Conibeer and A. Willoughby, Solar Cell Materials, John Wiley & Sons, Ltd, (2014).

[53] R. Hill and M. D. Archer, Clean electricity from photovoltaics, Imperial College Press, chapter 7, 277-345 (2001).

[54] S. Nishiwaki, N. Kohara, T. Negami, and T. Wada, $MoSe_2$ layer formation at $Cu(In,Ga)Se_2$/Mo interfaces in high efficiency $Cu(In_{1-x}Ga_x)Se_2$ solar cells, *Japanese Journal of Applied Physics*, **37**, 1ab, Part 2 L71-L73 (1998).

[55] T. Wada, N. Kohara, S. Nishiwaki, and T. Negami, Characterization of the Cu(In,Ga)$Se_2$/Mo interface in CIGS solar cells, *Thin Solid Films*, **387**, 1-2, 118-122 (2001).

[56] R. Caballero, M. Nichterwitz, A. Steigert, A. Eicke, I. Lauermann, H. W. Schock, and C. A. Kaufmann, Impact of Na on $MoSe_2$ formation at the CIGSe/Mo interface in thin-film solar cells on polyimide foil at low process temperatures, *Acta Materialia*, **63**, 54-62 (2014).

[57] D. Abou-Ras, G. Kostorz, D. Bremaud, M. Kalin, F. V. Kurdesau, A. N. Tiwari, and M. Dobeli, Formation and characterisation of $MoSe_2$ for Cu(In,Ga)$Se_2$ based solar cells, *Thin Solid Films*, **480**, 433-438 (2005).

[58] T. Klinkert, B. Theys, G. Patriarche, M. Jubault, F. Donsanti, J. F. Guillemoles, and D. Lincot, New insights into the Mo/Cu(In,Ga)$Se_2$ interface in thin film solar cells: Formation and properties of the $MoSe_2$ interfacial layer, *Journal of Chemical Physics*, **145**, 15, (2016).

[59] E. Jarzembowski, M. Maiberg, F. Obereigner, K. Kaufmann, S. Krause, and R. Scheer, Optical and electrical characterization of Cu(In,Ga)$Se_2$ thin film solar cells with varied absorber layer thickness, *Thin Solid Films*, **576**, 75-80 (2015).

[60] A. M. Gabor, J. R. Tuttle, D. S. Albin, M. A. Contreras, R. Noufi, and A. M. Hermann, High-Efficiency $CuIn_xGa_{1-x}Se_2$ Solar-Cells Made from $(In_x,Ga_{1-x})_2Se_3$ Precursor Films, *Applied Physics Letters*, **65**, 2, 198-200 (1994).

[61] R. Caballero, V. Izquierdo-Roca, X. Fontane, C. A. Kaufmann, J. Alvarez-Garcia, A. Eicke, L. Calvo-Barrio, A. Perez-Rodriguez, H. W. Schock, and J. R. Morante, Cu deficiency in multi-stage co-evaporated Cu(In,Ga)$Se_2$ for solar cells applications: Microstructure and Ga in-depth alloying, *Acta Materialia*, **58**, 9, 3468-3476 (2010).

[62] I. Repins, M. A. Contreras, B. Egaas, C. DeHart, J. Scharf, C. L. Perkins, B. To, and R. Noufi, 19.9%-efficient ZnO/CdS/$CuInGaSe_2$ solar cell with 81.2% fill factor, *Progress in Photovoltaics*, **16**, 3, 235-239 (2008).

[63] R. Scheer, A. Perez-Rodriguez, and W. K. Metzger, Advanced diagnostic and control methods of processes and layers in CIGS solar cells and modules, *Progress in Photovoltaics*, **18**, 6, 467-480 (2010).

[64] T. Friedlmeier, D. Braunger, D. Hariskos, M. Kaiser, H. Wanka, and H. Schock, Nucleation and growth of the CdS buffer layer on Cu(In,Ga)$Se_2$ thin films, in *Conference Record of the Twenty Fifth IEEE Photovoltaic Specialists Conference*, 845-848 (1996).

[65] J. Kessler, K. Velthaus, M. Ruckh, R. Laichinger, H. Schock, D. Lincot, R. Ortega, and J. Vedel, Chemical bath deposition of CdS on $CuInSe_2$, etching effects and growth kinetics, *Sixth Int. PVSEC*, Oxford IBH Publishing, 1005-1010 (1992).

[66] R. Ortega-Borges and D. Lincot, Mechanism of chemical bath deposition of cadmium sulfide thin films in the ammonia-thiourea system in situ kinetic study and modelization, *Journal of the Electrochemical Society*, **140**, 12, 3464-3473 (1993).

[67] N. Naghavi, G. Renou, V. Bockelee, F. Donsanti, P. Genevee, M. Jubault, J. F. Guillemoles, and D. Lincot, Chemical deposition methods for Cd-free buffer layers in CI(G)S solar cells: Role of window layers, *Thin Solid Films*, **519**, 21, 7600-7605 (2011).

[68] W. Witte, S. Spiering, and D. Hariskos, Substitution of the CdS buffer layer in CIGS thin-film solar cells: Status of current research and record cell efficiencies, *Vakuum in Forschung und Praxis*, **26**, 1, 23-27 (2014).

[69] U. Rau and M. Schmidt, Electronic properties of ZnO/CdS/$Cu(In,Ga)Se_2$ solar cells aspects of heterojunction formation, *Thin Solid Films*, **387**, 1-2, 141-146 (2001).

[70] J. Merino, J. Martín de Vidales, S. Mahanty, R. Díaz, F. Rueda, and M. León, Composition effects on the crystal structure of $CuInSe_2$, *Journal of applied physics*, **80**, 10, 5610-5616 (1996).

[71] L. Mandel, R. Tomlinson, and M. Hampshire, Crystal data for $CuGaSe_2$, *Journal of Applied Crystallography*, **10**, 2, 130-131 (1977).

[72] J. E. Jaffe and A. Zunger, Electronic structure of the ternary chalcopyrite semiconductors $CuAlS_2$, $CuGaS_2$, $CuInS_2$, $CuAlSe_2$, $CuGaSe_2$, and $CuInSe_2$, *Physical Review B*, **28**, 10, 5822-5847 (1983).

[73] S. Rühle, Tabulated values of the Shockley–Queisser limit for single junction solar cells, *Solar Energy*, **130**, 139-147 (2016).

[74] K. Orgassa, Coherent Optical Analysis of the ZnO/CdS/$Cu(In,Ga)Se_2$ thin film solar cell, Shaker Verlag, (2004).

[75] M. Cwil, M. Igalson, P. Zabierowski, and S. Siebentritt, Charge and doping distributions by capacitance profiling in $Cu(In,Ga)Se_2$ solar cells, *Journal of Applied Physics*, **103**, 6, 063701 (2008).

[76] M. Richter, C. Schubbert, P. Eraerds, J. Parisi, I. Riedel, T. Dalibor, and J. Palm, Comprehensive simulation model for Cu(In,Ga)(Se,S)$_2$ solar cells, *Solar Energy Materials and Solar Cells*, **132**, 162-171 (2015).

[77] T. Eisenbarth, T. Unold, R. Caballero, C. A. Kaufmann, and H.-W. Schock, Interpretation of admittance, capacitance-voltage, and current-voltage signatures in Cu(In,Ga)Se$_2$ thin film solar cells, *Journal of Applied Physics*, **107**, 3, 034509 (2010).

[78] T. P. Weiss, S. Nishiwaki, B. Bissig, S. Buecheler, and A. N. Tiwari, Voltage dependent admittance spectroscopy for the detection of near interface defect states for thin film solar cells, *Physical Chemistry Chemical Physics*, **19**, 45, 30410-30417 (2017).

[79] M. A. Contreras, I. Repins, W. K. Metzger, M. Romero, and D. Abou-Ras, Se activity and its effect on Cu(In,Ga)Se$_2$ photovoltaic thin films, *physica status solidi (a)*, **206**, 5, 1042-1048 (2009).

[80] S. Zhang, S.-H. Wei, A. Zunger, and H. Katayama-Yoshida, Defect physics of the CuInSe$_2$ chalcopyrite semiconductor, *Physical Review B*, **57**, 16, 9642 (1998).

[81] J. Bekaert, R. Saniz, B. Partoens, and D. Lamoen, Native point defects in CuIn$_{1-x}$Ga$_x$Se$_2$: hybrid density functional calculations predict the origin of p-and n-type conductivity, *Physical Chemistry Chemical Physics*, **16**, 40, 22299-22308 (2014).

[82] S.-H. Wei, S. Zhang, and A. Zunger, Effects of Ga addition to CuInSe$_2$ on its electronic, structural, and defect properties, *Applied physics letters*, **72**, 24, 3199-3201 (1998).

[83] S. H. Wei and A. Zunger, Band offsets and optical bowings of chalcopyrites and Zn-based II-VI alloys, *Journal of Applied Physics*, **78**, 6, 3846-3856 (1995).

[84] W. Shockley and H. J. Queisser, Detailed Balance Limit of Efficiency of p-n Junction Solar Cells, *Journal of Applied Physics*, **32**, 3, 510-& (1961).

[85] S. Siebentritt and U. Rau, Wide-gap chalcopyrites, Springer-Verlag Berlin Heidelberg, (2006).

[86] G. Bauer, R. Brüggemann, S. Tardon, S. Vignoli, and R. Kniese, Quasi-Fermi level splitting and identification of recombination losses from room temperature luminescence in Cu (In$_{1-x}$Ga$_x$)Se$_2$ thin films versus optical band gap, *Thin Solid Films*, **480-481**, 410-414 (2005).

[87] J. V. Li, S. Grover, M. A. Contreras, K. Ramanathan, D. Kuciauskas, and R. Noufi, A recombination analysis of Cu(In,Ga)$Se_2$ solar cells with low and high Ga compositions, *Solar Energy Materials and Solar Cells*, **124**, 143-149 (2014).

[88] M. A. Contreras, L. M. Mansfield, B. Egaas, J. Li, M. Romero, R. Noufi, E. Rudiger-Voigt, and W. Mannstadt, Wide bandgap Cu(In,Ga)$Se_2$ solar cells with improved energy conversion efficiency, *Progress in Photovoltaics: Research and Applications*, **20**, 7, 843-850 (2012).

[89] S. Zahedi-Azad and R. Scheer, Quenching interface recombination in wide bandgap Cu(In,Ga)$Se_2$ by potassium treatment, *physica status solidi c*, **14**, 6, 1600203 (2017).

[90] L. Oikkonen, M. Ganchenkova, A. Seitsonen, and R. M. Nieminen, Mass transport in $CuInSe_2$ from first principles, *Journal of Applied Physics*, **113**, 13, 133510 (2013).

[91] W. Witte, D. Abou-Ras, K. Albe, G. H. Bauer, F. Bertram, C. Boit, R. Brüggemann, J. Christen, J. Dietrich, and A. Eicke, Gallium gradients in Cu(In,Ga)$Se_2$ thin-film solar cells, *Progress in Photovoltaics: Research and Applications*, **23**, 6, 717-733 (2015).

[92] D. J. Schroeder, G. D. Berry, and A. A. Rockett, Gallium diffusion and diffusivity in $CuInSe_2$ epitaxial layers, *Applied Physics Letters*, **69**, 26, 4068-4070 (1996).

[93] J. Pohl and K. Albe, Thermodynamics and kinetics of the copper vacancy in $CuInSe_2$, $CuGaSe_2$, $CuInS_2$, and $CuGaS_2$ from screened-exchange hybrid density functional theory, *Journal of Applied Physics*, **108**, 2, 023509 (2010).

[94] B. Sapoval and C. Hermann, Physics of semiconductors, Springer-Verlag New York, (1995).

[95] J. M. Luttinger and W. Kohn, Motion of electrons and holes in perturbed periodic fields, *Physical Review*, **97**, 4, 869-883 (1955).

[96] H. Weinert, H. Neumann, H. J. Höbler, G. Kühn, and N. Van Nam, Infrared Faraday Effect in n-Type $CuInSe_2$, *physica status solidi (b)*, **81**, 1, K59-K61 (1977).

[97] C. Persson, Anisotropic hole-mass tensor of $CuIn_{1-x}Ga_x(S,Se)_2$: Presence of free carriers narrows the energy gap, *Applied Physics Letters*, **93**, 7, (2008).

[98] C. Persson, Y.-J. Zhao, S. Lany, and A. Zunger, n-type doping of $CuInSe_2$ and $CuGaSe_2$, *Physical Review B*, **72**, 3, 035211 (2005).

[99] L. E. Oikkonen, M. G. Ganchenkova, A. P. Seitsonen, and R. M. Nieminen, Effect of sodium incorporation into $CuInSe_2$ from first principles, *Journal of Applied Physics*, **114**, 8, (2013).

[100] E. Ghorbani, J. Kiss, H. Mirhosseini, G. Roma, M. Schmidt, J. Windeln, T. D. Kiihne, and C. Felser, Hybrid-Functional Calculations on the Incorporation of Na and K Impurities into the $CuInSe_2$ and $Culn_5Se_8$ Solar-Cell Materials, *Journal of Physical Chemistry C*, **119**, 45, 25197-25203 (2015).

[101] T. Maeda, A. Kawabata, and T. Wada, First-principles study on alkali-metal effect of Li, Na, and K in $CuInSe_2$ and $CuGaSe_2$, *Japanese Journal of Applied Physics*, **54**, 8S1, 08KC20 (2015).

[102] C. Kılıç and A. Zunger, n-type doping and passivation of $CuInSe_2$ and $CuGaSe_2$ by hydrogen, *Physical Review B*, **68**, 7, 075201 (2003).

[103] J. Bekaert, R. Saniz, B. Partoens, and D. Lamoen, First-principles study of carbon impurities in $CuInSe_2$ and $CuGaSe_2$, present in non-vacuum synthesis methods, *Journal of Applied Physics*, **117**, 1, 015104 (2015).

[104] S. Lany, Y.-J. Zhao, C. Persson, and A. Zunger, Halogen n-type doping of chalcopyrite semiconductors, *Applied Physics Letters*, **86**, 4, 042109 (2005).

[105] M. Igalson and P. Zabierowski, Transient capacitance spectroscopy of defect levels in CIGS devices, *Thin Solid Films*, **361**, 371-377 (2000).

[106] T. Walter, R. Herberholz, C. Muller, and H. W. Schock, Determination of defect distributions from admittance measurements and application to $Cu(In,Ga)Se_2$ based heterojunctions, *Journal of Applied Physics*, **80**, 8, 4411-4420 (1996).

[107] S. Lany and A. Zunger, Intrinsic D X Centers in Ternary Chalcopyrite Semiconductors, *Physical review letters*, **100**, 1, 016401 (2008).

[108] M. Igalson and P. Zabierowski, Electron traps in $Cu(In,Ga)Se_2$ absorbers of thin film solar cells studied by junction capacitance techniques, *Optoelectronics review*, 4, 261-268 (2003).

[109] M. Igalson and M. Edoff, Compensating donors in $Cu(In,Ga)Se_2$ absorbers of solar cells, *Thin Solid Films*, **480**, 322-326 (2005).

[110] Q. Cao, O. Gunawan, M. Copel, K. B. Reuter, S. J. Chey, V. R. Deline, and D. B. Mitzi, Defects in $Cu(In,Ga)Se_2$ chalcopyrite semiconductors: A comparative study of

material properties, defect states, and photovoltaic performance, *Advanced Energy Materials*, **1**, 5, 845-853 (2011).

[111] M. Igalson and A. Urbaniak, Defect states in the CIGS solar cells by photocapacitance and deep level optical spectroscopy, *Bulletin of the Polish Academy of Sciences: Technical Sciences*, **53**, 2, 157-161 (2005).

[112] W. Shockley and W. T. Read, Statistics of the Recombinations of Holes and Electrons, *Physical Review*, **87**, 5, 835-842 (1952).

[113] A. Stoneham, II. Non-radiative processes in insulators and semiconductors, *Philosophical Magazine*, **36**, 4, 983-997 (1977).

[114] A. Stoneham, Non-radiative transitions in semiconductors, *Reports on Progress in Physics*, **44**, 12, 1251-1295 (1981).

[115] S.-H. Wei and S. Zhang, Defect properties of $CuInSe_2$ and $CuGaSe_2$, *Journal of Physics and Chemistry of Solids*, **66**, 11, 1994-1999 (2005).

[116] P. Landsberg, Non-Radiative Transitions in Semiconductors, *physica status solidi (b)*, **41**, 2, 457-489 (1970).

[117] W. Michaelis and M. Pilkuhn, Radiative recombination in silicon p-n junctions, *physica status solidi (b)*, **36**, 1, 311-319 (1969).

[118] T. Kirchartz, U. Rau, M. Kurth, J. Mattheis, and J. Werner, Comparative study of electroluminescence from $Cu(In,Ga)Se_2$ and Si solar cells, *Thin Solid Films*, **515**, 15, 6238-6242 (2007).

[119] M. A. Green, Radiative efficiency of state-of-the-art photovoltaic cells, *Progress in Photovoltaics: Research and Applications*, **20**, 4, 472-476 (2012).

[120] S. Dinca, E. A. Schiff, B. Egaas, R. Noufi, D. Young, and W. Shafarman, Hole drift mobility measurements in polycrystalline $CuIn_{1-x}Ga_xSe_2$, *Physical Review B*, **80**, 23, 235201 (2009).

[121] M. Maiberg, C. Spindler, E. Jarzembowski, and R. Scheer, Electrical characterization of $Cu(In,Ga)Se_2$-solar cells by voltage dependent time-resolved photoluminescence, *Thin Solid Films*, **582**, 379-382 (2015).

[122] F. Werner, Hall measurements on low-mobility thin films, *Journal of Applied Physics*, **122**, 13, 135306 (2017).

[123] D. J. Schroeder, J. L. Hernandez, G. D. Berry, and A. A. Rockett, Hole transport and doping states in epitaxial $CuIn_{1-x}Ga_xSe_2$, *Journal of applied physics*, **83**, 3, 1519-1526 (1998).

[124] T. Nakada, D. Iga, H. Ohbo, and A. Kunioka, Effects of sodium on $Cu(In,Ga)Se_2$-Based thin films and solar cells, *Japanese Journal of Applied Physics*, **36**, 2, 732-737 (1997).

[125] M. Ruckh, D. Schmid, M. Kaiser, R. Schaffler, T. Walter, and H. W. Schock, Influence of substrates on the electrical properties of $Cu(In,Ga)Se_2$ thin films, *Solar Energy Materials and Solar Cells*, **41-2**, 335-343 (1996).

[126] U. Rau, M. Schmitt, F. Engelhardt, O. Seifert, J. Parisi, W. Riedl, J. Rimmasch, and F. Karg, Impact of Na and S incorporation on the electronic transport mechanisms of $Cu(In,Ga)Se_2$ solar cells, *Solid State Communications*, **107**, 2, 59-63 (1998).

[127] D. J. Schroeder and A. A. Rockett, Electronic effects of sodium in epitaxial $CuIn_{1-x}Ga_xSe_2$, *Journal of Applied Physics*, **82**, 10, 4982-4985 (1997).

[128] S. H. Wei, S. B. Zhang, and A. Zunger, Effects of Na on the electrical and structural properties of $CuInSe_2$, *Journal of Applied Physics*, **85**, 10, 7214-7218 (1999).

[129] L. Kronik, D. Cahen, and H. W. Schock, Effects of sodium on polycrystalline $Cu(In,Ga)Se_2$ and its solar cell performance, *Advanced Materials*, **10**, 1, 31-36 (1998).

[130] L. Kronik, U. Rau, J. F. Guillemoles, D. Braunger, H. W. Schock, and D. Cahen, Interface redox engineering of $Cu(In,Ga)Se_2$ - based solar cells: oxygen, sodium, and chemical bath effects, *Thin Solid Films*, **361**, 353-359 (2000).

[131] D. Cahen and R. Noufi, Defect Chemical Explanation for the Effect of Air Anneal on $CdS/CulnSe_2$ Solar-Cell Performance, *Applied Physics Letters*, **54**, 6, 558-560 (1989).

[132] Z. K. Yuan, S. Y. Chen, Y. Xie, J. S. Park, H. J. Xiang, X. G. Gong, and S. H. Wei, Na-Diffusion Enhanced p-type Conductivity in $Cu(In,Ga)Se_2$: A New Mechanism for Efficient Doping in Semiconductors, *Advanced Energy Materials*, **6**, 24, (2016).

[133] F. Couzinié-Devy, N. Barreau, and J. Kessler, Re-investigation of preferential orientation of $Cu(In,Ga)Se_2$ thin films grown by the three-stage process, *Progress in Photovoltaics: Research and Applications*, **19**, 5, 527-536 (2011).

[134] M. A. Contreras, M. J. Romero, and R. Noufi, Characterization of Cu(In,Ga)$Se_2$ materials used in record performance solar cells, *Thin Solid Films*, **511**, 51-54 (2006).

[135] D. Wolf, G. Müller, W. Stetter, and F. Karg, In-situ investigation of Cu-In-Se reactions: impact of Na on CIS formation, in *Proceedings of the 2nd World Conference on Photovoltaic Solar Energy Conversion*, 2426-2430 (1998).

[136] D. Braunger, S. Zweigart, and H. Schock, The influence of Na and Ga on the incorporation of the chalcogen in polycrystalline Cu(In,Ga)$(S,Se)_2$ thin-films for photovoltaic applications, in *2nd World Conference of Photovoltaic Solar Energy Conversion, Vienna*, 1113-1116 (1998).

[137] D. Rudmann, D. Brémaud, A. Da Cunha, G. Bilger, A. Strohm, M. Kaelin, H. Zogg, and A. Tiwari, Sodium incorporation strategies for CIGS growth at different temperatures, *Thin Solid Films*, **480**, 55-60 (2005).

[138] J. Granata and J. Sites, Impact of sodium in the bulk and in grain boundaries of $CuInSe_2$, in *Proceedings of the 2nd World Conference on Photovoltaic Solar Energy Conversion*, 604-607 (1998).

[139] D. W. Niles, K. Ramanathan, F. Hasoon, R. Noufi, B. J. Tielsch, and J. E. Fulghum, Na impurity chemistry in photovoltaic CIGS thin films: Investigation with x-ray photoelectron spectroscopy, *Journal of Vacuum Science & Technology A: Vacuum, Surfaces, and Films*, **15**, 6, 3044-3049 (1997).

[140] V. Probst, J. Rimmasch, W. Riedl, W. Stetter, J. Holz, H. Harms, F. Karg, and H. Schock, The impact of controlled sodium incorporation on rapid thermal processed Cu (InGa) $Se_2$-thin films and devices, in *Proceedings of 1994 IEEE 1st World Conference on Photovoltaic Energy Conversion-WCPEC*, 144-147 (1994).

[141] M. Powalla and B. Dimmler, Scaling up issues of CIGS solar cells, *Thin Solid Films*, **361**, 540-546 (2000).

[142] K. Granath, M. Bodegård, and L. Stolt, The effect of NaF on Cu(In,Ga)$Se_2$ thin film solar cells, *Solar energy materials and solar cells*, **60**, 3, 279-293 (2000).

[143] A. Rockett, The effect of Na in polycrystalline and epitaxial single-crystal $CuIn_{1-x}Ga_xSe_2$, *Thin Solid Films*, **480**, 2-7 (2005).

[144] F. Obereigner, N. Barreau, W. Witte, and R. Scheer, Open-circuit and doping transients of Cu (In, Ga) Se2 solar cells with varying Ga content, *Journal of Applied Physics*, **117**, 5, 055704 (2015).

[145] S. Lany and A. Zunger, Light-and bias-induced metastabilities in Cu(In,Ga)$Se_2$ based solar cells caused by the ($V_{Se}$-$V_{Cu}$) vacancy complex, *Journal of Applied Physics*, **100**, 11, 113725 (2006).

[146] A. Urbaniak and M. Igalson, Creation and relaxation of light-and bias-induced metastabilities in Cu(In,Ga)$Se_2$, *Journal of Applied Physics*, **106**, 6, 063720 (2009).

[147] H. Okada and T. Minemoto, Characterization method for the relaxation process of metastable defect states in Cu(In,Ga)$Se_2$ thin films with photoisothermal capacitance transient spectroscopy, *Japanese Journal of Applied Physics*, **50**, 2R, 020203 (2011).

[148] L. Oikkonen, M. G. Ganchenkova, A. P. Seitsonen, and R. Nieminen, Vacancies in $CuInSe_2$: new insights from hybrid-functional calculations, *Journal of Physics: Condensed Matter*, **23**, 42, 422202 (2011).

[149] P. T. Erslev, J. W. Lee, W. N. Shafarman, and J. D. Cohen, The influence of Na on metastable defect kinetics in CIGS materials, *Thin Solid Films*, **517**, 7, 2277-2281 (2009).

[150] S. M. Sze and K. K. Ng, Physics of semiconductor devices, 3rd ed., John Wiley & Sons, (2006).

[151] A. Goetzberger, B. Voß, and J. Knobloch, Sonnenenergie: Photovoltaik: Physik und Technologie der Solarzelle, Teubner, (1994).

[152] W. Vanroosbroeck and W. Shockley, Photon-Radiative Recombination of Electrons and Holes in Germanium, *Physical Review*, **94**, 6, 1558-1560 (1954).

[153] S. Hegedus, D. Desai, and C. Thompson, Voltage dependent photocurrent collection in CdTe/CdS solar cells, *Progress in Photovoltaics: Research and Applications*, **15**, 7, 587-602 (2007).

[154] X. Liu and J. Sites, Solar-cell collection efficiency and its variation with voltage, *Journal of Applied Physics*, **75**, 1, 577-581 (1994).

[155] V. Nadenau, U. Rau, A. Jasenek, and H. Schock, Electronic properties of $CuGaSe_2$-based heterojunction solar cells. Part I. Transport analysis, *Journal of Applied Physics*, **87**, 1, 584-593 (2000).

[156] C.-T. Sah, R. N. Noyce, and W. Shockley, Carrier generation and recombination in pn junctions and pn junction characteristics, *Proceedings of the IRE*, **45**, 9, 1228-1243 (1957).

[157] H. Pauwels and G. Vanhoutte, The influence of interface state and energy barriers on the efficiency of heterojunction solar cells, *Journal of Physics D: Applied Physics*, **11**, 5, 649 (1978).

[158] A. Niemegeers, S. Gillis, and M. Burgelman, A user program for realistic simulation of polycrystalline heterojunction solar cells: SCAPS-1D, in *Proceedings of the 2nd World Conference on Photovoltaic Energy Conversion, Vienna, Austria*, 672-675 (1998).

[159] H. Wilhelm, H.-W. Schock, and R. Scheer, Interface recombination in heterojunction solar cells: Influence of buffer layer thickness, *Journal of Applied Physics*, **109**, 8, 084514 (2011).

[160] M. J. Adams and A. Nussbaum, Proposal for a New Approach to Heterojunction Theory, *Solid-State Electronics*, **22**, 9, 783-791 (1979).

[161] M. S. Lundstrom and R. J. Schuelke, Modeling Semiconductor Heterojunctions in Equilibrium, *Solid-State Electronics*, **25**, 8, 683-691 (1982).

[162] M. Maiberg and R. Scheer, Theoretical study of time-resolved luminescence in semiconductors. I. Decay from the steady state, *Journal of Applied Physics*, **116**, 12, (2014).

[163] M. Maiberg and R. Scheer, Theoretical study of time-resolved luminescence in semiconductors. II. Pulsed excitation, *Journal of Applied Physics*, **116**, 12, (2014).

[164] D. V. O'Connor and D. Phillips, Time-Correlated Single Photon Counting, *London: Academic Press*, (1984).

[165] W. Becker, A. Bergmann, M. A. Hink, K. Konig, K. Benndorf, and C. Biskup, Fluorescence lifetime imaging by time-correlated single-photon counting, *Microscopy Research and Technique*, **63**, 1, 58-66 (2004).

[166] C. Holzapfel, On statistics of time-to-amplitude converter systems in photon counting devices, *Review of Scientific Instruments*, **45**, 7, 894-896 (1974).

[167] B. Candy, Photomultiplier characteristics and practice relevant to photon counting, *Review of scientific instruments*, **56**, 2, 183-193 (1985).

[168] M. Wahl, Time-correlated single photon counting, *Technical Note: PicoQuant GmbH*, (2014).

[169] D. Briggs and J. Grant, Surface analysis by auger and X-ray photoelectron spectroscopy, IM Publications and SurfaceSpectra Limited, Charlton Manchester, (2003).

[170] K. Shimizu, H. Habazaki, P. Skeldon, and G. Thompson, Radiofrequency GDOES: a powerful technique for depth profiling analysis of thin films, *Surface and Interface Analysis: An International Journal devoted to the development and application of techniques for the analysis of surfaces, interfaces and thin films*, **35**, 7, 564-574 (2003).

[171] V. Efimova, Study in analytical glow discharge spectrometry and its application in materials science, Dissertation, Saechsische Landesbibliothek-Staats-und Universitaetsbibliothek Dresden, (2011).

[172] D. Abou-Ras, T. Kirchartz, and U. Rau, Advanced characterization techniques for thin film solar cells, John Wiley & Sons, (2016).

[173] M. Turcu, O. Pakma, and U. Rau, Interdependence of absorber composition and recombination mechanism in Cu(In,Ga)(Se,S)(2) heterojunction solar cells, *Applied Physics Letters*, **80**, 14, 2598-2600 (2002).

[174] R. Scheer, Activation energy of heterojunction diode currents in the limit of interface recombination, *Journal of Applied Physics*, **105**, 10, (2009).

[175] M. Rusu, W. Eisele, R. Wurz, A. Ennaoui, M. C. Lux-Steiner, T. P. Niesen, and F. Karg, Current transport in ZnO/ZnS/Cu(In,Ga)(S,Se)(2) solar cell, *Journal of Physics and Chemistry of Solids*, **64**, 9-10, 2037-2040 (2003).

[176] M. A. Green, General temperature dependence of solar cell performance and implications for device modelling, *Progress in Photovoltaics: Research and Applications*, **11**, 5, 333-340 (2003).

[177] W. Hörig, H. Neumann, H. J. Höbler, and G. Kühn, Temperature dependence of the absorption edge in cuinse2, *physica status solidi (b)*, **80**, 1, K21-K24 (1977).

[178] H. Neumann, W. Hörig, E. Reccius, W. Möller, and G. Kühn, Temperature dependence of the fundamental absorption edge in CuGaSe2, *Solid State Communications*, **27**, 4, 449-451 (1978).

[179] R. Herberholz, M. Igalson, and H. Schock, Distinction between bulk and interface states in CuInSe 2/CdS/ZnO by space charge spectroscopy, *Journal of Applied Physics*, **83**, 1, 318-325 (1998).

[180] I. Mora-Seró, Y. Luo, G. Garcia-Belmonte, J. Bisquert, D. Muñoz, C. Voz, J. Puigdollers, and R. Alcubilla, Recombination rates in heterojunction silicon solar cells analyzed by impedance spectroscopy at forward bias and under illumination, *Solar Energy Materials and Solar Cells*, **92**, 4, 505-509 (2008).

[181] P. C. Chan and C.-T. Sah, Exact equivalent circuit model for steady-state characterization of semiconductor devices with multiple-energy-level recombination centers, *IEEE Transactions on Electron Devices*, **26**, 6, 924-936 (1979).

[182] C. Wagner, W. Riggs, L. Davis, J. Moulder, and G. Muilenberg, Handbook of X-ray Photoelectron Spectroscopy, Perkin-Elmer Corp, *Eden Prairie, MN*, **38**, (1979).

[183] S. Heise, V. Gerliz, M. Hammer, J. Ohland, J. Keller, and I. Hammer-Riedel, Light-induced changes in the minority carrier diffusion length of Cu (In, Ga) Se2 absorber material, *Solar Energy Materials and Solar Cells*, **163**, 270-276 (2017).

[184] J. Reichardt, M. Bär, A. Grimm, I. Kötschau, I. Lauermann, S. Sokoll, M. Lux-Steiner, C.-H. Fischer, C. Heske, and L. Weinhardt, Inducing and monitoring photoelectrochemical reactions at surfaces and buried interfaces in Cu (In, Ga)(S, Se) 2 thin-film solar cells, *Applied Physics Letters*, **86**, 17, 172102 (2005).

# A. Appendixes

## A.1. Potential curve of a n-n$^+$-hetero-junction

Using the Schottky approximation fails in the case of deriving the potential curve for a junction with two equal doped layers like an n-n$^+$-junction. The reason is that on the higher n$^+$- doped side (here the low resistive window = lrw) the depletion of majority charge carriers will not create a positive space charge with the host doping density $N_{D,lrw}$. On the other hand the space charge region within the moderate n-doped layer (here the high resistive window = hrw) is generated by electrons diffused from the n$^+$-region into the n-region. With the interface located at z = 0 and under the assumption that the Debye length $\lambda_D$ is much smaller than the width of the layer, the Poisson equation of each space charge region reads to

$$-\frac{d^2\varphi_{hrw}}{dz^2} = \frac{dE_{z,hrw}}{dz} = \frac{\rho_{hrw}(z)}{\varepsilon_{hrw}} = \frac{q\left(N_{D,hrw} - n(z)\right)}{\varepsilon_{hrw}} \quad for\ z \leq 0\,,$$

$$-\frac{d^2\varphi_{lrw}}{dz^2} = \frac{dE_{z,lrw}}{dz} = \frac{\rho_{lrw}(z)}{\varepsilon_{lrw}} = \frac{q\left(N_{D,lrw} - n(z)\right)}{\varepsilon_{lrw}} \quad for\ z > 0\,. \qquad \textbf{A.1}$$

Under the assumption of $\lambda_{D,hrw}$, $\lambda_{D,lrw} << d_{hrw}$, $d_{lrw}$ both layers can be considered as extended to infinity. Then, in the case of impurity exhaustion, the electron densities are $n(-\infty) \approx N_{D,hrw}$ and $n(+\infty) \approx N_{D,lrw}$. The boundary conditions of the electric fields are $E_{z,hrw}(-\infty) \approx 0$ and $E_{z,lrw}(+\infty) \approx 0$. Per definition the electric potential is set to 0 for $z \rightarrow -\infty$ giving $\varphi_{hrw}(-\infty) \approx 0$. In the following an analytical solution of equation A.1 is exemplary derived for the accumulation region of the hrw-layer. With the above given boundary conditions of the electron densities and the electrostatic potential. Further by applying the chain rule for the derivative of the electric field equation A.1 can be reformulated to

$$-\frac{d^2}{dz^2}\varphi_{hrw}(z) = -E_{hrw}(z)\cdot\frac{dE_{hrw}(z)}{d\varphi_{hrw}(z)} = \frac{qN_{D,hrw}}{\varepsilon_{hrw}}\left(1 - exp\left\{\frac{q\varphi_{hrw}(z)}{k_BT}\right\}\right). \qquad \textbf{A.2}$$

Integration of equation A.2 and using the boundary conditions $E_{z,hrw}(-\infty) \approx 0$, $\varphi_{hrw}(-\infty) \approx 0$ gives

$$\frac{[E_{hrw}(z)]^2}{2} = \frac{qN_{D,hrw}}{\varepsilon_{hrw}}\left(\frac{k_BT}{q}\left(exp\left\{\frac{q\varphi_{hrw}(z)}{k_BT}\right\}-1\right)-\varphi_{hrw}(z)\right). \qquad \textbf{A.3}$$

With a series expansion of the exponential term

$$exp\left\{\frac{q\varphi_{hrw}(z)}{k_BT}\right\} \approx 1+\frac{q}{k_BT}\varphi_{hrw}(z)+\frac{1}{2}\left[\frac{q}{k_BT}\varphi_{hrw}(z)\right]^2 \qquad \textbf{A.4}$$

equation A.3 can be simplified to

$$\left[\frac{d}{dz}\varphi_{hrw}(z)\right]^2 = \frac{q^2N_{D,hrw}}{k_BT\varepsilon_{hrw}}[\varphi_{hrw}(z)]^2 = \frac{1}{\lambda_{D,hrw}^2}[\varphi_{hrw}(z)]^2 \qquad \textbf{A.5}$$

with $\varphi_{hrw}(-\infty) \approx 0$ the solution of equation A.5 is

$$\varphi_{hrw}(z) = C_1 exp\left\{\frac{z}{\lambda_{D,hrw}}\right\} \;\; for \;\; z \le 0\,. \qquad \textbf{A.6}$$

For the low resistive window one will find

$$\varphi_{lrw}(z) = \Delta\varphi_w - C_2 exp\left\{-\frac{z}{\lambda_{D,lrw}}\right\} \;\; for \;\; z > 0\,, \qquad \textbf{A.7}$$

where $\Delta\varphi_w$ correspond to the complete potential drop over the junction of the 2 window layers (see equation 2.18). The constants $C_1$ and $C_2$ can be determined from the continuity of the electric field $\varepsilon_{hrw}\cdot E_{hrw}(0) = \varepsilon_{lrw}\cdot E_{lrw}(0)$ and the electrostatic potential $\varphi_{hrw}(0) = \varphi_{lrw}(0)$ at the metallurgical interface. Finally the potential curves in the particular region are resulting to

$$\varphi_{hrw}(z) = \Delta\varphi_w \cdot \frac{\varepsilon_{lrw}\lambda_{D,hrw}}{\varepsilon_{lrw}\lambda_{D,hrw}+\varepsilon_{hrw}\lambda_{D,lrw}} exp\left\{\frac{z}{\lambda_{D,hrw}}\right\} \;\; for \;\; z \le 0\,,$$

$$\varphi_{lrw}(z) = \Delta\varphi_w\left(1-\frac{\varepsilon_{hrw}\lambda_{D,lrw}}{\varepsilon_{lrw}\lambda_{D,hrw}+\varepsilon_{hrw}\lambda_{D,lrw}} exp\left\{-\frac{z}{\lambda_{D,lrw}}\right\}\right) \;\; for \;\; z > 0\,. \qquad \textbf{A.8}$$

## A.2. General properties of simulation models

**Table A - 1** Overview of default device and simulation parameter, the reference temperature of physical quantities is T = 300 K.

| Physical quantity | $B_{rad,a}$ [$cm^3 \cdot s^{-1}$] | $B_{rad,b}$, $B_{rad,w}$ [$cm^3 \cdot s^{-1}$] | $v_{th,p}$, $v_{th,n}$ [$cm \cdot s^{-1}$] | $R_S$ [$\Omega \cdot cm^2$] | $R_{Sh}$ [$\Omega \cdot cm^2$] |
|---|---|---|---|---|---|
| Value | $5 \cdot 10^{-11}$ | -- | $10^7$ | $1.5 \cdot 10^{-2}$ | $4 \cdot 10^3$ |
| Numerical quantity | N discretisation levels | j confidence interval | | | |
| Value | 100 | 7 (tail)<br>6 (gaussian) | | | |

**Table A - 2** Temperature dependency of physical variables for solar cells simulated under varying temperatures.

| General quantity | $v_{th,p}$, $v_{th,n}$ | $N_{C,V}$ | $R_S$ | $R_{Sh}$ | |
|---|---|---|---|---|---|
| Proportionality | $T^{1/2}$ | $T^{3/2}$ | const. | const. | |
| Absorber | $B_{rad,a}$ | $\mu_p$ | $\mu_n$ | Defects | |
| | | | | $\sigma_p$ | $\sigma_n$ |
| Proportionality | const. | $T^{3/2}$ | const. | $T^1$ | $T^1$ |
| Buffer, window | $\mu_p$, $\mu_n$ | Defects | | | |
| | | $\sigma_p$, $\sigma_n$ | | | |
| Proportionality | const. | const. | | | |

**Table A - 3** Optical properties of the particular layers of simulated solar cells.

| Layer | Back contact Mo | Absorber CIGSe | Buffer CdS | Window | | Front contact Ni/Al |
|---|---|---|---|---|---|---|
| | | | | i-ZnO | ZnO:Al | |
| Absorption | 0 | Calculated from Table B.1 in Ref. [74] with x = 0.23 | Calculated from Table B.2 in Ref. [74] | | | 0 |
| Reflectivity, Interference | 0 | 0 | 0 | 0 | 0 | 0 |

## A.3. Physical quantities: Default simulation model

**Table A - 4** Numerical values of the physical layer properties of the default simulation model used in section **2** and **3**. Energy level of interface states are referred to the band edges of the CIGSe absorber. (A) indicates default properties for acceptor like states and (D) for donor like states.

| Layer / Properties | Back contact | Absorber | Interface | Buffer | Window | | Front contact |
|---|---|---|---|---|---|---|---|
| | Mo | CIGSe | CIGSe/CdS | CdS | i-ZnO | ZnO:Al | Ni/Al |
| d [µm] | -- | 2.8 | -- | 0.05 | 0.05 | 0.3 | -- |
| $\Phi_m$, $\chi_e$ [eV] | Flat band[a)] | 4.5 | -- | 4.4 | 4.5 | 4.5 | Flat band[a)] |
| $E_g$ [eV] | -- | 1.15 | -- | 2.4 | 3.3 | 3.4 | -- |
| $\varepsilon_r$ | -- | 13.6 | -- | 10 | 9 | 9 | -- |
| $N_C$ [$cm^{-3}$] | -- | $7 \cdot 10^{17}$ | -- | $4 \cdot 10^{18}$ | $4 \cdot 10^{18}$ | $4 \cdot 10^{18}$ | -- |
| $N_V$ [$cm^{-3}$] | -- | $1.5 \cdot 10^{19}$ | -- | $9 \cdot 10^{18}$ | $9 \cdot 10^{18}$ | $9 \cdot 10^{18}$ | -- |
| $\mu_n$ [$cm^2 \cdot V^{-1} \cdot s^{-1}$] | -- | 10 | -- | 20 | 20 | 20 | -- |
| $\mu_p$ [$cm^2 \cdot V^{-1} \cdot s^{-1}$] | -- | 10 | -- | 20 | 20 | 20 | -- |
| $N_{A,D}$ [$cm^{-3}$] | -- | $7 \cdot 10^{15}$ (A) | -- | $4 \cdot 10^{15}$ (D) | $1.71 \cdot 10^{18}$ (D) | $2 \cdot 10^{18}$ (D) | -- |
| Defect properties | | | | | | | |
| $N_d$ [$cm^{-3}$], $N_{d,IF}$ [$cm^{-2}$] | -- | $10^{13}$ (D) | $10^{11}$ (A, D) | $3 \cdot 10^{15}$ (A) | $10^{18}$ (A) | $10^{16}$ (A) | -- |
| $E_d - E_V$ [eV] | -- | Midgap | Midgap | Midgap | Midgap | Midgap | -- |
| $E_{char}$ [eV] | -- | Discrete | Discrete | Discrete | Discrete | Discrete | -- |
| $\sigma_n$ [$cm^2$] | -- | $10^{-12}$ | $10^{-15}$ (A), $10^{-12}$ (D) | $10^{-15}$ | $10^{-15}$ | $10^{-15}$ | -- |
| $\sigma_p$ [$cm^2$] | -- | $5 \cdot 10^{-15}$ | $10^{-12}$ (A), $10^{-15}$ (D) | $10^{-12}$ | $10^{-12}$ | $10^{-12}$ | -- |
| $\tau_{n0}$ [ns] | -- | 10 | -- | 33 | 0.1 | 10 | -- |
| $\tau_{p0}$ [ns] | -- | 2000 | -- | $3.3 \cdot 10^{-2}$ | $10^{-4}$ | $10^{-2}$ | -- |
| Recombination velocities | | | | | | | |
| $S_{n0}$ [$cm \cdot s^{-1}$] | $10^4$ | $5.1 \cdot 10^3$ | $10^3$ (A), $10^6$ (D) | $4 \cdot 10^3$ | $7.2 \cdot 10^4$ | $7.2 \cdot 10^3$ | $10^7$ |
| $S_{p0}$ [$cm \cdot s^{-1}$] | $10^7$ | $3.6 \cdot 10^2$ | $10^6$ (A), $10^3$ (D) | $1.3 \cdot 10^5$ | $2.3 \cdot 10^6$ | $2.3 \cdot 10^5$ | $10^7$ |

[a)] Flat band denotes a variable metal work function $\Phi_m$ adjusted to the majority carrier Fermi level with the result that no band bending occurs at the metal contacts.

## A.4. Physical quantities: Simulation model of Paper 4

**Table A - 5** Numerical values of the physical layer properties of the extended simulation model used in paper 4 (section 4.4). Energy level of interface states are referred to the band edges of the CIGSe absorber. (G) means Gaussian distributed, and (T) means tail like distributed.

| Layer / Properties | Back contact | Interfacial layer | Absorber | | | | | Interface | |
|---|---|---|---|---|---|---|---|---|---|
| | Mo | $MoSe_x$ | CIGSe | | | | | CIGSe/CdS | |
| d [μm] | -- | 0.03 | 2.77 | | | | | -- | |
| $\Phi_m$, $\chi_e$ [eV] | 5.5 | 4.5 | 4.5 | | | | | -- | |
| $E_g$ [eV] | -- | 1.15 | 1.15 | | | | | -- | |
| $\varepsilon_r$ | -- | 13.6 | 13.6 | | | | | -- | |
| $N_C$ [$cm^{-3}$] | -- | $7{\cdot}10^{17}$ | $7{\cdot}10^{17}$ | | | | | -- | |
| $N_V$ [$cm^{-3}$] | -- | $5{\cdot}10^{15}$ | $1.5{\cdot}10^{19}$ | | | | | -- | |
| $\mu_n$ [$cm^2{\cdot}V^{-1}{\cdot}s^{-1}$] | -- | 10 | 10 | | | | | -- | |
| $\mu_p$ [$cm^2{\cdot}V^{-1}{\cdot}s^{-1}$] | -- | 10 | 10 | | | | | -- | |
| $N_{A,D}$ [$cm^{-3}$] | -- | $10^{15}$ (D) | $7{\cdot}10^{15}$ (A) | | | | | -- | |
| Defects | -- | Acceptor | A1 | A2 | D1 | D2 | | $A_{IF}$ | $D_{IF}$ |
| $N_d$ [$cm^{-3}$], $N_{d,IF}$ [$cm^{-2}$] | -- | $10^{13}$ | $3{\cdot}10^{16}$ | $4{\cdot}10^{16}$ | $10^{13}$ | $1.5{\cdot}10^{16}$ | | $3.5{\cdot}10^{11}$ | $2.86{\cdot}10^{11}$ |
| $E_d - E_V$ [eV] | -- | Midgap | 0 | 0.45 | Midgap | 0.965 | 0.54 | 0.3 | 0.965 |
| $E_{char}$ [eV] | -- | Discrete | 0.08 (T) | 0.3 (G) | Discrete | 0.035 (G) | | 0.15 (G) | 0.035 (G) |
| $\sigma_n$ [$cm^2$] | -- | $10^{-15}$ | $10^{-17}$ | $10^{-17}$ | $10^{-12}$ | $2{\cdot}10^{-13}$ | $10^{-11}$ | $10^{-17}$ | $2{\cdot}10^{-13}$ |
| $\sigma_p$ [$cm^2$] | -- | $5{\cdot}10^{-12}$ | $10^{-14}$ | $10^{-14}$ | $5{\cdot}10^{-15}$ | $10^{-17}$ | $10^{-19}$ | $3{\cdot}10^{-11}$ | $10^{-17}$ |
| $\tau_{n0}$ [ns] | -- | $10^4$ | $3.3{\cdot}10^2$ | $2.5{\cdot}10^2$ | 10 | $3.3{\cdot}10^{-2}$ | $6.7{\cdot}10^{-4}$ | -- | -- |
| $\tau_{p0}$ [ns] | -- | 2 | 0.33 | 0.25 | $2{\cdot}10^3$ | $6.7{\cdot}10^2$ | $6.7{\cdot}10^4$ | -- | -- |
| $S_{n0}$ [$cm{\cdot}s^{-1}$] | $10^4$ | -- | -- | -- | -- | -- | -- | 35 | $2.7{\cdot}10^5$ |
| $S_{p0}$ [$cm{\cdot}s^{-1}$] | $10^7$ | -- | -- | -- | -- | -- | -- | $10^8$ | 29 |
| Transition | -- | 0/– | 0/– | 0/– | 0/+ | 0/+ | +/++ | 0/– | 0/+ |

The physical properties of the device for simulating voltage dependent admittance spectra and J-V curves in Paper 4 (section 4.4) are given in Table A - 5. Parameters of the window layers (CdS, i-ZnO, AZO) are identical to the default model in Table A - 4 and for this reason not listed in Table A - 5.

## A.5. Overview samples used for ALE experiments

**Table A - 6** List of samples used for the verification and evaluation of the ALE impact on CIGSe absorbers, up to complete solar cells.

| Designation | Methods | Comments, Observations |
|---|---|---|
| CIGSe2016-01-08-1 | TRPL | ALE under low light intensity with TRPL laser and high light intensity with sun simulator |
| CIGSe2016-01-09-1 | TRPL, GDOES | Accumulation of Na at the very surface after ALE of bare CIGSe absorber |
| CIGSe2016-01-10-1 | TRPL | Trial recovery of ALE effect by DA of absorber in atmosphere |
| CIGSe2016-01-11-1 | TRPL, GDOES | Repetition Na accumulation at the very surface after ALE of bare CIGSe absorber |
| CIGSe2016-01-12-1 | TRPL | ALE after DA of bare absorber |
| CIGSe2016-01-13-1 | TRPL | ALE as a function of low light intensities with TRPL laser |
| CIGSe2016-01-14-1 | TRPL, GDOES | ALE effect after illumination in vacuum |
| CIGSe2016-07-27-1 | TRPL | Trial recovery of ALE effect by CBD-CdS |
| CIGSe2016-08-05-1 | TRPL | ALE on CIGSe layers without Na |
| CIGSe2016-10-18-1 | TRPL, XPS, J-V | Accumulation of Na and O at the CIGSe suface and detoriation of J-V-parameter of complete solar cells due to ALE (Paper1) |
| CIGSe2016-11-21-1 | TRPL, XPS, J-V, GDOES | Repetition Na and O accumulation at the CIGSe surface after ALE (Paper1) |
| CIGSe2017-03-14-1 | TRPL, J-V, GDOES, $V_{OC}(T)$, $V_{OC}(t)$ | Smaller activation energy of $J_0$ than the CIGSe band gap energy and decreasing $V_{OC}$ transient for devices with ALE-absorber (Paper1) |
| CIGSe2017-04-04-1 | TRPL, J-V, GDOES, $V_{OC}(T)$, $V_{OC}(t)$, VAS | Impact of ALE and CdS on TRPL-transients<br>Recovery of solar cells with ALE absorbers by HLS (Paper3)<br>Detection of interface states due to ALE with voltage dependent admittance spectroscopy (Paper3)<br>Partial recovery of ALE induced TRPL lifetime reduction after rinsing the bare CIGSe absorber with $(NH_4)_2S$ |
| CIGSe2017-06-22-1 | TRPL, GDOES | HLS on CdS covered CIGSe absorbers with and without ALE treatment<br>Na accumulation at the CIGSe/CdS interface after HLS<br>ALE on CIGSe without Na<br>ALE with photon energies below $E_{g,a}$ |

| Designation | Methods | Comments, Observations |
|---|---|---|
| CIGSe2017-07-25-1 | TRPL, J-V | TRPL lifetime reduction as a function of ALE light dose and intensity (Paper2)<br>Metastable states after HLS and DA of complete solar cells (Paper2)<br>Persistent reduction of TRPL lifetime after CdS deposition (Paper2)<br>ALE with photon energies below $E_{g,a}$ |
| CIGSe2017-09-13-1 | TRPL, J-V, GDOES, $V_{OC}(T)$, $V_{OC}(t)$, VAS | Reproduction of detected interface states for solar cells with ALE absorbers in VAS<br>Simulation of device characteristics (Paper4) |
| CIGSe2017-11-08-1 | TRPL, XPS | Investigation of the impact of humidity during ALE (only with XPS)<br>ALE as a function of photon energy |
| CIGSe2017-11-10-1 | TRPL, XPS, J-V, GDOES, $V_{OC}(T)$, $V_{OC}(t)$, C-V, VAS | Investigation of the impact of humidity during ALE (only with XPS)<br>Investigation as fabricated and HLS state on complete solar cells |
| CIGSe2018-01-30-1 | TRPL, J-V | Investigation of metastable character, applying HLS, forward and reverse bias (J-V)<br>ALE of absorbers with NaF-PDT |
| CIGSe2018-04-10-1<br>CIGSe2018-04-11-1<br>CIGSe2018-04-12-1<br>CIGSe2018-04-13-1 | TRPL | ALE on CIGSe with PDT: KF<br>RbF<br>CsF<br>without |
| CIGSe2018-06-27-1 | TRPL, J-V | Investigation of metastable character, applying HLS, forward and reverse bias (TRPL on complete solar cells)<br>Impact of ALE on CIGSe absorbers without Na |
| CIGSe2018-06-27-1 | TRPL, J-V, GDOES, $V_{OC}(T)$, $V_{OC}(t)$ | Repetition TRPL lifetime reduction as a function of ALE light dose and intensity<br>Investigation of metastable character, applying HLS, forward and reverse bias ($V_{OC}(T)$, $V_{OC}(t)$) |

Methods, abbreviations:

| | |
|---|---|
| C-V | Capacitance as a function of voltage at fixed temperature and frequency |
| DA | Annealing in darkness |
| GDOES | Glow-discharge optical emission spectroscopy |
| HLS | Heat light soaking |
| J-V | Measurement of J-V-characteristics |
| PDT | Post-deposition treatment |
| TRPL | Time-resolved pholuminescence |
| VAS | Voltage dependent admittance spectroscopy (Capacitance as a function of voltage, frequency, and temperature) |
| $V_{OC}(T)$ | Measurement of $V_{OC}$ as a function of temperature |
| $V_{OC}(t)$ | Measurement of $V_{OC}$ as a function of time under red light illumination |
| XPS | X-Ray photoelectron emission spectroscopy |

## Danksagung (Acknowledgement)

An dieser Stelle möchte ich mich in besonderem Maße bei Prof. Dr. Roland Scheer bedanken. Zum einen, dass er sich meiner als Betreuer angenommen und mir somit die Erstellung dieser Arbeit ermöglicht hat. Vielmehr jedoch bedanke ich mich für die großzügige Kollaboration hinsichtlich der getätigten Veröffentlichungen und die vorausgehenden Dialoge zum Bewältigen der experimentellen und theoretischen Herausforderungen meiner Untersuchungen.

Für die Beurteilung dieser Dissertation gilt mein Dank sowohl den Referenten als auch der gesamten Prüfungskommission.

Hinsichtlich der Interpretation des ALE Effektes konnten durch die XPS Messungen innerhalb der Fachgruppe Oberflächen- und Grenzflächenphysik von Prof. Dr. Wolf Widdra fundamentale Erkenntnisse erzielt werden. Dabei möchte ich mich besonders herzlich bei Dr. Stefan Förster bedanken, nicht nur für die Durchführung der XPS Messungen, sondern vielmehr für die aktive Beteiligung an der Planung und Auswertung der Experimente sowie die Evaluierung der Ergebnisse. Ich habe unsere Zusammenarbeit wirklich genossen.

Ein großes Dankeschön geht an Dr. Matthias Maiberg, dessen breites Wissen im Bereich der Halbleiterphysik und Photovoltaik aber insbesondere auf dem Gebiet der zeitaufgelösten Photoluminezenz zu Lösungen und neuen Denkansätzen vieler Fragestellungen beigetragen hat.

Prof. Dr. Thomas Walter (Hochschule Ulm) möchte ich für die ausführliche Diskusion über die Interpretation der gemessenen Admittanzspektren danken.

Dr. Wolfgang Fränzel und Dr. Heiko Kempa bin ich sehr verbunden für die Organisation des Laborbetriebes insbesondere bei der Beschaffung von Gebrauchsgegenständen bis hinzu Ersatzteilen oder die realisierung von technischen Lösungen und Reparaturen an experimentellen Einrichtungen. Dadurch erfolgte im Bereich der Administration eine hohe Entlastung, was mehr Freiheit im Bereich der Forschungsaktivitäten bot.

Thomas Schneider danke ich für seine Opferbereitschaft zur Herstellung von CIGSe Schichten für meine Untersuchungen sowie für die zahlreichen fachlichen Diskusionen und unterhaltsamen Momente im Büro. In diesem Zusammenhang möchte ich mich bei meinen Bürokollegen Ulrich Fahnert und Thomas Richter bedanken. Nicht nur für die humorvollen Beiträge im Büroalltag, sondern auch für die Fertigstellung meiner CIGSe Schichten zu

kompletten Solarzellen sowie die Unterstützung bei technischen Problemstellungen im Labor- und Anlagenbetrieb.

Ebenfalls danke ich Dr. Setareh Zahedi-Azad für das Bereitstellen von CIGSe Schichten und das Bonden meiner Proben für Tieftemperaturmessungen.

Der gesamten Fachgruppe Photovoltaik gilt mein Dank für ein reibungsloses Miteinander. Sehr angenehm empfand ich hierbei den regen Austausch mit Leonard Wägele und Chris Bluhm über fachspezifische aber auch allgemeine Themen.

Sehr geschätzt habe ich die Zusammenabeit mit den Mitarbeitern der Forschungswerkstätten für Feinmechanik und Elektronik, ohne deren Hilfe wohl viele meiner Experimente nicht hätten realisiert werden können.

Zu guter Letzt gilt mein größter Dank meiner Familie und Freunden, die für die nötige Entlastung und Ablenkung vom Arbeitsalltag gesorgt haben.

## Eidesstattliche Erklärung (Declaration on oath)

Hiermit erkläre ich, dass ich die vorliegende Arbeit selbstständig und ausschließlich mit den von mir angegebenen Quellen und Hilfsmitteln verfasst habe. Ferner versichere ich, dass ich alle wörtlichen und sinngemäßen Zitate als solche kenntlich gemacht habe.

Halle, 25.08.2021 Unterschrift: